FINITE ELEMENT ANALYSIS AND EXPERIMENTAL STUDY OF DOVETAIL ATTACHMENTS

A THESIS SUBMITTED TO
THE GRADUATE SCHOOL OF NATURAL AND APPLIED SCIENCES
OF
MIDDLE EAST TECHNICAL UNIVERSITY

BY

AHMET ARDA AKAY

IN PARTIAL FULFILLMENT OF THE REQUIREMENTS
FOR
THE DEGREE OF MASTER OF SCIENCE
IN
AEROSPACE ENGINEERING

SEPTEMBER 2016

Approval of the thesis:

FINITE ELEMENT ANALYSIS AND EXPERIMENTAL STUDY OF DOVETAIL ATTACHMENTS

submitted by **AHMET ARDA AKAY** in partial fulfillment of the requirements for the degree of **Master of Science in Aerospace Engineering Department, Middle East Technical University** by,

Prof. Dr. Gülbin Dural Ünver
Dean, Graduate School of **Natural and Applied Sciences** _____

Prof. Dr. Ozan Tekinalp
Head of Department, **Aerospace Engineering** _____

Assist. Prof. Dr. Ercan Gürses
Supervisor, **Aerospace Engineering Department, METU** _____

Examining Committee Members:

Prof. Dr. Altan Kayran
Aerospace Engineering Department, METU _____

Assist. Prof. Dr. Ercan Gürses
Aerospace Engineering Department, METU _____

Assoc. Prof. Dr. Demirkan Çöker
Aerospace Engineering Department, METU _____

Assoc. Prof. Dr. Afşin Sarıtaş
Civil Engineering Department, METU _____

Prof. Dr. Mehmet Ali Güler
Mechanical Engineering Department, TOBB ETÜ _____

Date: _____

I hereby declare that all information in this document has been obtained and presented in accordance with academic rules and ethical conduct. I also declare that, as required by these rules and conduct, I have fully cited and referenced all material and results that are not original to this work.

Name, Last Name: AHMET ARDA AKAY

Signature :

ABSTRACT

FINITE ELEMENT ANALYSIS AND EXPERIMENTAL STUDY OF DOVETAIL ATTACHMENTS

Akay, Ahmet Arda
M.S., Department of Aerospace Engineering
Supervisor : Assist. Prof. Dr. Ercan Gürses

September 2016, 138 pages

Dovetail-rim attachment is a critical component of an aeroengine compressor disc. Fretting fatigue is commonly seen in these attachments, which results to premature failures such as cracking or wear. Main cause of the fretting fatigue is high stress gradients occuring near the edges of contact. Since the problem involves contact, the effect of the certain contact parameters on the stress gradients is investigated. These contact stresses are non-singular and can converge to a value with successive mesh refinement. For this purpose, a submodelling procedure is introduced which can provide an accurate solution without the requirement of high computational resource. Submodelling is implemented on two different models and convergence of the peak stresses is observed within about five percent. Hence, three experimental studies are carried out on dovetail-rim attachments. For this purpose, an experimental setup is designed. Comparison of the finite element analysis and the experiment is performed. In the first two experiments, it is seen that the misalignment of the specimens causes asymmetric contact condition in the contact pairs between the disc and the blade parts of dovetail. Therefore, inconsistencies between finite element and experiment are observed. Certain changes are made in the experimental setup for the third experiment. Due to the alterations made, the third experiment gives results more consistent to the finite element. It is concluded that the measurements during the experiment are highly sensitive to the tolerances and imperfections in the experiment of the dovetail

specimen.

Keywords: Finite Element, Dovetail Joint, Contact Modelling, Submodelling, Experimental Study, Tension Test

ÖZ

KIRLANGIÇ KUYRUĞU BAĞLANTI ELEMANININ SONLU ELEMANLAR ANALİZLERİ VE BUNLARIN DENEY SONUÇLARIYLA KIYASLANMASI

Akay, Ahmet Arda
Yüksek Lisans, Havacılık ve Uzay Mühendisliği Bölümü
Tez Yöneticisi : Yrd. Doç. Dr. Ercan Gürses

Eylül 2016 , 138 sayfa

Kırlangıç kuyuruğu tipi bağlantı elemanı, uçak motorlarının kompressor disk bölümünün kritik elemanlarından biridir. Bu tip bağlantı elemanlarında görülen en temel sorunlardan biri aşındırma yorulmasıdır. Aşındırma yorulması malzeme üzerinde oluşacak çatlakların ve aşınmanın en önemli nedenlerindendir. Kontakt yüzeyinin köşelerinde oluşan yüksek gerinimler, aşındırma yorulmasına yol açmaktadır. İncelenen bağlantı elemanı kontakt modellemesi içerdiği için, belli kontakt parametrelerinin bu yüksek gerinimlere olan etkisi incelenmiştir. Bu gerinimlerin yakınsaması, sonlu elemanlar yöntemi kullanarak eleman boyutunun küçültülmesiyle sağlanabilmektedir. Bu nedenle, çok yüksek bir bilgisayar çözüm gücü gerektirmeden bu gerinimlerin yakınsamasını sağlayan submodelling metotu kullanılmıştır. Bu metot iki farklı modele uygulanmış ve gerinimlerin yüzde 5 mertebelerinde yakınsadığı gözlemlenmiştir. Buna ek olarak kırlangıç kuyruğu bağlantı elemanın deneysel çalışması ile ilgili üç adet deney yapılmıştır. Bu çalışmaların gerçekleştirilebilmesi için bir deney düzeneği tasarlanmıştır. Sonlu elemenlar analizleriyle deney sonuçlarının kıyaslaması yapılmıştır. İlk iki deneyde, parçalar arasındaki kontakt durumlarında bir asimetri gözlenmiştir. Parçaların tam olarak hizalanmadığı da gözlemlenmiştir. Bu nedenle bu deneylerin sonuçları ve sonlu eleman analizleri sonuçları arasında tutarsızlık bulunmaktadır. Üçüncü deneyi gerçekleştirmeden önce, deney prosedüründe belli başlı değişiklikler yapılmıştır. Yapılan bu değişikliklere bağlı olarak üçüncü deneyde elde

edilen sonuçların sonlu elemanlar analizleri sonuçlarıyla daha tutarlı olduğu gözlemlenmiştir. Bu çalışmalar sonucunda deneyde elde edilen ölçümlerin, deney sisteminde veya parçalarda bulunan ufak kusurlara ve toleranslara oldukça duyarlı olduğu gözlemlenmiştir.

Anahtar Kelimeler: Sonlu Elemenalar, Kırlangıç Kuyruğu, Kontakt Modellemesi, Submodelling, Deneysel Çalışma, Çekme Deneyi

to my family and friends

ACKNOWLEDGMENTS

Firstly, I would like to express my sincere thanks to my supervisor Asst. Prof. Dr. Ercan Gürses for his advices, recommendations, guidance, motivation and hours he spent throughout my thesis study.

I would like to express my sincere gratitude to Prof. Dr. Altan Kayran and Assoc. Dr. Demirkan Çöker for their advices and contributions to this study.

I would like to thank a lot to my friends Samet Emre Yılmaz and Hasan Emre Oktay for their support and help. The discussions I have made with them throughout this study enhanced my knowledge on certain topics.

I would like to thank Oğuz Atalay for the hours he has spent with me and the help he provided during experiments. I would also thank to Özgün Şener and Burcu Taşdemir for their contributions during the experiments.

I would like to my co-workers in the Aerospace Engineering Department for the friendship and the support they have provided.

I would like to thank all my friends for their motivation, support and friendship.

Lastly, I would like to give my deepest gratitude to my family. I would never have made it here without them. I am much obliged.

TABLE OF CONTENTS

ABSTRACT v

ÖZ vii

ACKNOWLEDGMENTS x

TABLE OF CONTENTS xi

LIST OF TABLES xvi

LIST OF FIGURES xviii

LIST OF ABBREVIATIONS xxiv

CHAPTERS

1 INTRODUCTION 1

1.1 Motivation of the Thesis 1

1.2 Objective of the Thesis 3

1.3 Literature Review 3

1.3.1 Literature Review on Submodelling 3

1.3.2 Literature Review on Fretting Fatigue and Dovetail Experiments 5

1.4 Organization of the Thesis 7

2 EFFECTS OF CONTACT PARAMETERS ON FINITE ELEMENT RESULTS 9

2.1 Problem Definition 10

2.1.1 Geometry 10

2.1.2 Material Properties 10

2.1.3 Finite Element Model 11

2.1.4 Loading and Boundary Condition 12

2.2 Parametric Study 13

2.2.1 Preliminary Results 14

2.2.2 Effect of Normal Stiffness Factor 15

2.2.3 Effect of Penetration Tolerance Factor 19

2.2.4 Effect of Elastic Slip Tolerance Factor 21

2.2.5 Effect of Friction Coefficient 22

2.2.6 Effect of Constraint Enforcement Methods 23

2.2.6.1 Normal Lagrange Method 24

2.2.6.2 Pure Penalty Method 26

2.2.6.3 Augmented Lagrange Method 27

2.2.6.4 Comparison of Contact Enforcement Methods 28

3 SUBMODELLING 31

3.1 Singular and Nonsingular Edge of Contact Stresses on Contact Problems 31

3.2 Procedure 34

3.3 Submodelling On A Simple Two Block Geometry 38
3.3.1 Geometry and Material Properties 38
3.3.2 Finite Element Model 39
3.3.2.1 Contact Properties 39
3.3.2.2 Meshing 39
3.3.3 Loading and Boundary Conditions 41
3.3.4 Submodels 42
3.3.5 Results 43
3.4 Submodelling On Dovetail Geometry 53
3.4.1 Geometry 53
3.4.2 Material Properties 54
3.4.3 Finite Element Model 54
3.4.3.1 Contact Properties 55
3.4.3.2 Meshing 56
3.4.4 Loading and Boundary Conditions 59
3.4.5 Submodels 60
3.4.6 Results 62
4 EXPERIMENTAL STUDY OF THE DOVETAIL SPECIMEN UNDER TENSILE LOADING AND VALIDATION WITH THE FINITE ELEMENT ANALYSIS 77
4.1 Experimental Study 77
4.1.1 Preliminary Finite Element Analysis Model of the Experimental Setup 79

4.1.2 Specimen 81

4.1.3 Holders 82

4.1.4 Pins 83

4.1.5 Experimental Setup 84

4.2 Finite Element Model of the Experimental Setup 89

4.2.1 Full Finite Element Model of the Experimental Setup 89

4.2.2 Simplified Finite Element Model of the Experimental Setup 91

4.3 Results 95

4.3.1 Experimental and Finite Element Analysis Results 95

4.3.1.1 Global Load Displacement Results . . 95

4.3.1.2 DIC Results 96

4.3.1.3 Strain Gauge Results 105

4.3.2 Assessment of Difference in Results 109

4.3.2.1 Eccentric Loading Case 110

4.3.2.2 Different Friction Coefficients Between Two Contact Surfaces 111

4.4 Third Experiment on the Dovetail Specimen 114

4.4.1 Alterations of the Third Experiment and the Finite Element Model 114

4.4.2 Comparison of the Finite Element and Experimental Results 117

4.5 Conclusion of the Experimental Studies 123

5 CONCLUSION 125

REFERENCES 129

APPENDICES

A TECHNICAL DRAWINGS OF THE COMPONENTS OF THE EXPERIMENTAL SETUP 133

A.1 Technical Drawing of the Blade Specimen 133

A.2 Technical Drawing of the Disc Specimen 134

A.3 Technical Drawing of the Holders 135

A.4 Comparison of the Second and the Third Experiments 136

LIST OF TABLES

TABLES

Table 2.1 Material properties [8] 11

Table 2.2 ANSYS 2D finite element model properties with contact region properties between the blocks 12

Table 2.3 Relationship between the normal contact stiffness factor and the normal contact stiffness 16

Table 2.4 2D finite element model properties for the parametric study of the normal stiffness factor 17

Table 2.5 Finite element model solution time for the normal stiffness factor study 19

Table 2.6 The relationship between the penetration tolerance factor and the resulting penetration tolerance for h=0.25 mm 20

Table 2.7 Solution times of the constraint enforcement methods: the Normal Lagrange method, the Pure Penalty method and the Augmented Lagrange method 29

Table 2.8 Pros and cons of contact enforcement methods 29

Table 3.1 Material properties of Homalite® [8] 38

Table 3.2 Mesh parameters used for coarse, medium and fine global models . . 41

Table 3.3 Maximum equivalent stress for coarse, medium, fine global models and their convergence checks 42

Table 3.4 Mesh parameters used for coarse, medium and fine submodels . . . 43

Table 3.5 Maximum normal and shear stresses at the edge of contact on bottom body for both global and submodels with their errors 43

Table 3.6 Maximum normal and shear stresses at the edge of contact on top body for both global and submodels with their errors 44

Table 3.7 Mesh parameters used for superfine (S) and extra-superfine (ES) global models 51

Table 3.8 Solution times of the global models and the submodels 51

Table 3.9 Material properties of aero-engine [1] 54

Table 3.10 Mesh parameters used outside of the boundary layer for coarse, medium and fine global models 58

Table 3.11 Mesh parameters used inside of the boundary layer for coarse, medium and fine global models 59

Table 3.12 Maximum equivalent stress for coarse, medium, fine global models and their convergence checks 61

Table 3.13 Mesh parameters used for coarse, medium and fine submodels . . . 62

Table 3.14 Maximum normal and shear stresses at the edge of contact on the disc for both global and submodels with their errors 66

Table 3.15 Maximum normal and shear stresses at the edge of contact on the blade for both global and submodels with their errors 66

Table 3.16 Mesh parameters used outside of the boundary layer for superfine (S) and extra-superfine (ES) global models 73

Table 3.17 Mesh parameters used inside of the boundary layer for superfine (S) and extra-superfine (ES) global models 73

Table 3.18 Solution times of the global models and the submodels 74

Table 4.1 Boundary conditions of the finite element model of the experimental setup 80

Table 4.2 Material properties of Inconel Alloy 718 - AMS 5663 81

Table 4.3 Material properties of 12.9 grade structural steel 83

Table 4.4 Strain gauge readings of S3 and S5 before and after tapping at the pre-loading stage of the third experiment 115

Table 4.5 Load steps of the third experiment 116

LIST OF FIGURES

FIGURES

Figure 1.1 A typical aeroengine compressor disc [22] 1

Figure 1.2 Bladed-disc rotor section of a typical aeroengine compressor disc [1] 2

Figure 1.3 three different dovetail geometries having angles of 35°, 45° and 55° [11] 6

Figure 2.1 Problem Geometry 10

Figure 2.2 2D finite element model with local 0.25 mm mesh size at the contact region 11

Figure 2.3 Loadings and boundary conditions for the finite element model . . 12

Figure 2.4 Normal stress distribution in y-direction of 2D finite element model 14

Figure 2.5 The path defined for the stress output (shown in pink) 15

Figure 2.6 Contact stress for 5 different normal stiffness factors for mesh size of 0.25 mm 17

Figure 2.7 The maximum contact stress for 5 different normal stiffness factors for three mesh sizes 18

Figure 2.8 The contact stress on the selected path for 4 different penetration tolerance factors for mesh size of 0.25 mm 21

Figure 2.9 The contact stress on the selected path for 4 different elastic slip tolerance factors for mesh size of 0.25 mm 22

Figure 2.10 The contact stress on the selected path for 4 different friction coefficients for mesh size of 0.25 mm 23

Figure 2.11 Contact stress for 3 different contact enforcement methods for mesh size of 0.25 mm 28

Figure 3.1 Classical elasticity examples of contact problems [26] 33

Figure 3.2 Boundary layer for the dovetail model 35

Figure 3.3 Example of submodel grids [9] 37

Figure 3.4 Contact surface between bodies 39

Figure 3.5 Boundary layer of two block model 40

Figure 3.6 Edges that are defined with a sizing value to have systematic mesh . 41

Figure 3.7 Coarse submodel 42

Figure 3.8 The paths defined for the stress output (shown in red) 44

Figure 3.9 Normal stress in x-direction σ_x on lower part for three global and three submodels on the defined path 45

Figure 3.10 Normal stress in x-direction σ_x on upper part for three global and three submodels on the defined path 46

Figure 3.11 Normal stress in y-direction σ_y on lower part for three global and three submodels on the defined path 47

Figure 3.12 Normal stress in y-direction σ_y on upper part for three global and three submodels on the defined path 48

Figure 3.13 Shear stress in xy-direction τ_{xy} on lower part for three global and three submodels on the defined path 49

Figure 3.14 Shear stress in xy-direction τ_{xy} on upper part for three global and three submodels on the defined path 50

Figure 3.15 Normal stress in x-direction σ_x on lower part for extra-superfine global model and fine submodel on the defined path 52

Figure 3.16 Geometric details of dovetail joint [22] 53

Figure 3.17 2D finite element model of the dovetail joint 54

Figure 3.18 Equivalent stress on the peak stress location for 2D and 3D finite element analyses of dovetail 55

Figure 3.19 Contact surface between bodies 56

Figure 3.20 Boundary layer of dovetail model 57

Figure 3.21 Edges that are defined with a sizing value to have a systematic mesh 58

Figure 3.22 Loadings and boundary conditions for the finite element model . . 60

Figure 3.23 Equivalent stress distribution of 2D dovetail model with coarse mesh 61

Figure 3.24 Submodel 62

Figure 3.25 Condition of the contact at the stage of 0.1 times of the maximum loading 63

Figure 3.26 Condition of the contact at the stage of 0.5 times of the maximum loading 63

Figure 3.27 Condition of the contact at the maximum loading 64

Figure 3.28 The paths defined for the stress output (shown in red) 64

Figure 3.29 Coordinate system defined for stress outputs 65

Figure 3.30 Normal stress in x-direction σ_x on the disc for three global and three submodels on the defined path 67

Figure 3.31 Normal stress in x-direction σ_x on the blade for three global and three submodels on the defined path 68

Figure 3.32 Normal stress in y-direction σ_y on the disc for three global and three submodels on the defined path 69

Figure 3.33 Normal stress in y-direction σ_y on the blade for three global and three submodels on the defined path 70

Figure 3.34 Shear stress in xy-direction τ_{xy} on the disc for three global and three submodels on the defined path 71

Figure 3.35 Shear stress in xy-direction τ_{xy} on the blade for three global and three submodels on the defined path 72

Figure 3.36 Normal stress in y-direction σ_x on disc for extra-superfine global model and fine submodel on the defined path 75

Figure 3.37 Contact stress distribution between the disc and the blade [1] 76

Figure 4.1 Experimental set-up's used in the literature 78

Figure 4.2 Components of the experimental setup 79

Figure 4.3 Finite element model of the experimental setup with loadings and boundary conditions 80

Figure 4.4 Finite element mesh grid of the experimental setup 81

Figure 4.5 Equivalent stress on the specimen under 20 kN tensile loading . . . 82

Figure 4.6 Equivalent stress on the adapters under 20 kN tensile loading . . . 83
Figure 4.7 Equivalent stress on the pins under 20 kN tensile loading 84
Figure 4.8 Strain gauge location on the disc specimen 85
Figure 4.9 Strain gauge locations on the blade specimen 85
Figure 4.10 Strain gage connections to the data acquisition system 86
Figure 4.11 DIC paintings 86
Figure 4.12 Experimental setup and DIC camera 87
Figure 4.13 Experimental setup 88
Figure 4.14 Loading rate 88
Figure 4.15 Finite element mesh of the full model of the experimental setup . . 90
Figure 4.16 Refined mesh at the location of the strain gauge on the disc 90
Figure 4.17 Contact regions of the full model of the experimental setup 91
Figure 4.18 Boundary conditions of the simplified model 92
Figure 4.19 Finite element mesh of the simplified model of the experimental setup 93
Figure 4.20 Refined mesh at the location of the strain gauge on the blade (S3) . 93
Figure 4.21 Contact regions of the simplified model of the experimental setup . 94
Figure 4.22 Load displacement curve of the system obtained from the tensile testing machine 96
Figure 4.23 Stage points defined on the specimens 97
Figure 4.24 Displacements in x direction of the stage points defined on the specimens 97
Figure 4.25 Displacements in y direction of the stage points defined on the specimens 98
Figure 4.26 Displacements in x direction at the stage of 20 kN maximum load . 99
Figure 4.27 Displacements in y direction at the stage of 20 kN maximum load . 100
Figure 4.28 Von Misses strain at the stage of 20 kN maximum load 101
Figure 4.29 Path defined for the displacement output 102

Figure 4.30 Displacements in x direction of the nodes that are located at the vertical path defined on the DIC results 102

Figure 4.31 Paths defined on the specimens 103

Figure 4.32 Load displacement curve of the system obtained from the relative displacements between paths 1 and 2 104

Figure 4.33 Load displacement curve of the system obtained from the relative displacements between paths 1 and 3 104

Figure 4.34 Load displacement curve of the system obtained from the relative displacements between paths 1 and 4 105

Figure 4.35 Strain gauge readings of the experiment 106

Figure 4.36 Comparison of strain readings S1 of the experiment, simplified finite element model and full finite element model 107

Figure 4.37 Comparison of average strain readings of S2 and S4 of the experiment, simplified finite element model and full finite element model 108

Figure 4.38 Comparison of average strain readings of S3 and S5 of the experiment, simplified finite element model and full finite element model 108

Figure 4.39 Close-up DIC image of the contact region between the disc and the blade at the beginning of the experiment 110

Figure 4.40 Load displacement curves of the system obtained from averaging displacements of paths 1 and 2. Finite element results are presented for perfectly symmetric and two eccentric loading cases. 111

Figure 4.41 Load displacement curves of the experiment and the finite element model obtained from averaging displacements of paths 1 and 2. Finite element results are presented for perfectly symmetric and two uneven friction coefficient cases. 112

Figure 4.42 Von Misses strain at the stage of 20 kN maximum load 113

Figure 4.43 Modified experimental setup 115

Figure 4.44 Nodes that additional constraints are defined on for the simplified finite element model of the third experiment 117

Figure 4.45 Load displacement curve of the global system 118

Figure 4.46 Load displacement curve of the system obtained from averaging displacements of path 1 and 2 119

Figure 4.47 Load displacement curve of the system obtained from averaging displacements of path 1 and 3 119

Figure 4.48 Strain gauge readings of the thirdexperiment 120

Figure 4.49 Strain readings S1 of the experiment, simplified finite element model and full finite element model 121

Figure 4.50 Average strain readings of S2 and S4 of the experiment, simplified finite element model and full finite element model 121

Figure 4.51 Average strain readings of S3 and S5 of the experiment, simplified finite element model and full finite element model 122

Figure A.1 Technical drawing of the blade specimen 133

Figure A.2 Technical drawing of the disc specimen 134

Figure A.3 Technical drawing of the upper holder 135

Figure A.4 Technical drawing of the lower holder 135

Figure A.5 Load displacement curve of the system obtained from averaging displacements of path 1 and 2 136

Figure A.6 Load displacement curve of the system obtained from averaging displacements of path 1 and 3 136

Figure A.7 Strain readings of S1 of the experiment, simplified finite element model and full finite element model 137

Figure A.8 Average strain readings of S2 and S4 of the experiment, simplified finite element model and full finite element model 137

Figure A.9 Average strain readings of S3 and S5 of the experiment, simplified finite element model and full finite element model 138

LIST OF ABBREVIATIONS

fkn	Normal Stiffness Factor
slto	Elastic Slip Tolerance Factor
ftoln	Penetration Tolerance Factor
h	Mesh Size
E	Young's Modulus
μ	Coefficient Of Friction
$\prod$	Potential Energy Functional
W	Elastic Energy
λ_N	Lagrange Multiplier in Normal Direction
ϵ_N	Penalty Parameter
R	Local Radius of Curvature
σ	Normal Stress
τ	Shear Stress

CHAPTER 1

INTRODUCTION

1.1 Motivation of the Thesis

Aeroengine compressor discs consist of three critical components. These are the hub region, the dovetail-rim region and the areas that contain assembly holes or welds [18]. Critical areas are highlighted in Figure 1.1. Components of the aeroengine compressor discs are subjected to high thermo-mechanical loads during the flight of the air vehicle. These loads are the centrifugal forces of the blades, loads generated by spacers and assembly bolts and thermal stresses. Due to these loads, highly stressed areas occur in the component [22]. In order not to have a catastrophic failure of the compressor disc, it is vital to have a sustainable engine design regarding to these loads on the components.

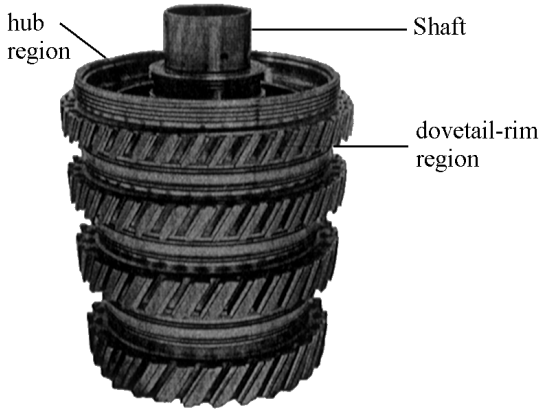


Figure 1.1: A typical aeroengine compressor disc [22]

In this thesis work, dovetail-rim region of an aeroengine compressor disc under the action of the centrifugal forces of the blades is investigated. A detailed dovetail-rim

region of an aeroengine for a single blade section is given in Figure 1.2. During the operation of the engine, the blades are rotating at a high speed which causes a radially outward movement of the blades. Because of the radial motion of the blade, the dovetail root-blade and the dovetail slot-disc get into contact. The dovetail root-blade is in the dovetail slot-disc which prevents the radial motion of the blade assembly. Accordingly, highly stressed areas occur at the interface of the disc and the blade. Peak values of these contact stresses are located at the edges of the contact surface.

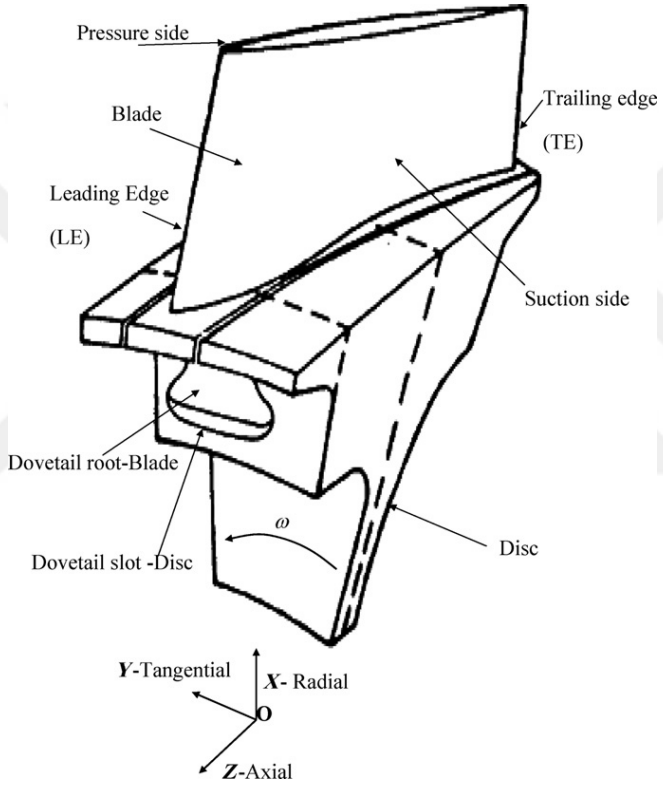


Figure 1.2: Bladed-disc rotor section of a typical aeroengine compressor disc [1]

Premature failures such as cracking or wear are commonly observed on dovetail attachments. In order to have a reliable dovetail-rim assembly, the mechanics of the interface should be studied with caution. Having the knowledge on the subject will allow designers to satisfy the requirements of high trust to weight ratio engines without compromising the safety conditions [25].

1.2 Objective of the Thesis

Finite element method is a useful tool which is used in a wide variety of fields in engineering. However, it may lead to misleading results if it is used by an inexperienced analyst. Because of the reason that the analysis of the dovetail attachment is a contact problem, contact mechanics should be studied and understood in detail. Presence of contact introduces non-linearities to the finite element analysis. Effects of the certain contact parameters such as the normal stiffness factor, the penetration tolerance factor, the elastic slip tolerance factor, the friction coefficient and the constraint enforcement methods on the finite element analysis should be examined. Some of these parameters have strong effects on the results of the finite element problems. For this reason, it is essential to have a wise choice on these parameters while creating the finite element model.

Contact stresses, which cause the fretting fatigue, occurring at the edges of the contact zone are investigated in this thesis work. In [26], these stresses are proved to be nonsingular and converges to a value with successive mesh refinement on the edges of contact. To obtain reliable elastic stresses by using modest computing resources, submodelling approach introduced in [9] is implemented to the finite element analyses. Submodelling can be briefly explained as cutting out a region of interest and modelling it separately. Boundary conditions of the extracted submodel are taken from a previously solved global model. The submodelling technique allows the analyst to have a solution with high resolution in a region of interest without the requirement of high computational resource. In order to validate the finite element results obtained with submodelling, a tension test is conducted on the dovetail geometry. Then, the results of the experiment is compared with the finite element results.

1.3 Literature Review

1.3.1 Literature Review on Submodelling

There are several methods introduced in the literature to increase the accuracy of the finite element analysis. One of these methods is the multigrid technique. In this

method, a previously solved coarse model is used as an initial guess for an iterative solution to reduce the size of the stiffness matrix of the finite element solution [5]. Implementation of the multigrid technique on solid mechanics examples are given in [23, 24]. Adaptive refinement may be combined with the multigrid technique. In the adaptive refinement, a transition from a coarser mesh to a finer mesh occurs as one proceed from the far field to the region of interest. Example of the adaptive refinement is given in [29]. Another method used to increase the accuracy of the finite element solution is the substructuring method. This method combines a group of finite elements into a single element, which is called the superelement. The group of finite elements is represented with a single-matrix in the finite element solution, which reduces the size of the global solution matrix and decreases the solution time [2]. Examples of the substructuring method are given in [14, 21]. A more contemporary approach to have an accurate solution in a region of interest is the submodelling technique. In this method, a local region where the accuracy of the mesh determines the results of the solution is broken out from the global model and it is modelled separately. The cut out model is meshed with a finer mesh compared to the mesh of the global model. The boundary conditions of the submodel are taken from the previously solved coarser model. Since the number of nodes on the boundary of the submodel will be greater than the number of nodes on the boundary of the global model, an interpolation method is used to determine the boundary conditions to be assigned to the intervening nodes. The submodelling is also called as zooming, global-local analysis, rezoning and windowing.

The first application of the submodelling method to the finite element analysis of the dovetail specimen is presented by Cormier et al. [9]. Some of the early applications of the submodelling approach on different geometries are cited therein. The difference of this work from the other submodelling applications is that it has a ratio of global model area to submodel area around 200 to 1, whereas the maximum value of the ratio is 50 to 1 in previous papers. In the paper, the submodelling technique is firstly used on an engineering problem which has an exact analytic solution. After verifying the analytical solution with the submodel results, it is implemented on a 2D dovetail geometry and the convergence of the peak contact stress is visualized. Cormier et al. uses displacement shape functions as boundary condition on the boundaries

of the submodel. Sinclair et al. state that the use of displacement shape functions may yield to logarithmic stress singularities on the the submodel boundary. Instead, cubic splines may be fit to the boundaries of the submodel and they can be used as the boundary condition [27]. Stress values at the edges of contact for dovetail geometry are proved to be converging to a value with successive mesh refinement of the submodel. These stresses appears to be non-singular since they have a convergence behaviour. Accordingly, numerical verification of non-singular stress state for dovetail attachment is presented in [26]. The first application of the submodelling approach on 3D dovetail finite element model is done by Beisheim and Sinclair [3]. The convergence of the peak stress on 3D model is observed; however, the contact between the disc and the blade is assumed to be frictionless in this study. The most extensive dovetail analyses are conducted by Anandavel et al. [1]. 3D finite element analyses are done for 15 different loading conditions including angular velocity and aero-dynamical loads. Hence, effects of the skew angle of the dovetail on the results are presented. It is deducted that for 3D straight dovetail model, the variation of peak stress in the thickness direction is negligible.

1.3.2 Literature Review on Fretting Fatigue and Dovetail Experiments

Fretting fatigue is usually observed in dovetail assemblies due to high contact stresses and relatively small displacements develop between the disc and the blade components of the dovetail. Fretting fatigue can be described as a damage mechanism which lowers the fatigue strength of the component due the corrosion between contacting bodies [12]. Moreover, it is stated that the damage related to the fretting is one of the most costly damage types of in-service [20].

To observe the parameters effecting the fretting fatigue life of a dovetail attachment, Golden et al. present three different dovetail geometries having angles of 35^o, 45^o and 55^o [11]. Corresponding dovetail geometries are given in Figure 1.3. Local contact forces are determined by using a series of strain gages located on the specimen. Test results show that there is no correlation between the dovetail angle and fretting fatigue life of the dovetail, whereas the contact forces are dependent on the dovetail angle. Hence, for a single geometry, it is deduced that the contact loads has no

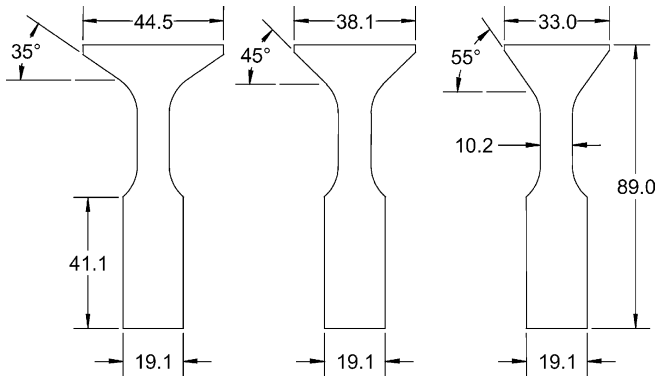


Figure 1.3: three different dovetail geometries having angles of 35^o, 45^o and 55^o [11]

effect on the fretting fatigue life of the dovetail, only the externally applied load affects the fatigue life. Rather than experimentally calculating contact loads, Golden et al. proposed a hybrid method to calculate contact loads and stresses [10]. The method uses a coarse 2D finite element method analysis to estimate contact loads and an analysis software CAPRI to calculate contact stresses. Moreover, the stresses at the edges of contact are computed by implementation of a stress intensity factor to contact stress results. Peak stress results are obtained similar to those obtained by using finite element method with a finer mesh size. Hence, another outcome of this study is that the fracture mechanics approaches accurately estimates the crack growth in dovetail specimen. To increase the fretting fatigue strength of the dovetail geometry, Beisheim and Sinclair introduced a crowning surface to the blade on the contacting flat surface between the disc and the blade [4]. The contact surface of the blade is no longer a flat surface but have an elliptic paraboloid profile. It is seen that the crowning reduces the maximum contact stress by more than one-third for the dovetail attachment. Therefore, the fretting fatigue strength of the attachment considered to be increasing by using crowning on the contacting surface of the blade. Wei and Wang use a fretting specimen to predict the fretting life and crack growth path of a dovetail attachment based on the similarities between the specimen and the dovetail attachment [31]. It is stated in the paper that the peak stresses at the edges of the contact zone of the blade and the disk are the main cause of the fretting fatigue. Hence, for the estimation of the fretting fatigue life and crack propagation path on the dovetail specimen, fracture mechanics parameters of the crack, such as initial angle, initial location, growth angle, may be used. The approach introduced in the paper starts with the determination of the contact stress and location of the peak

stress; secondly, by using the correlation between the initial angle of the crack and the stress intensity factor, calculation of the initial possible angle of the crack is done; thirdly, to evaluate the fretting fatigue life and the crack propagation path, simulation of the crack propagation is conducted by using boundary element method. The first experimental study on the fretting fatigue strength of the dovetail attachments on the actual geometry is done by Murugesan and Mutoh [19]. In the previous studies, a generalized tangential stress range-compressive stress range (TSR-CSR) diagram has been used to predict fretting fatigue strength regardless of the boundary conditions, material properties, contact geometry, etc. Experimental results show a good agreement between the fretting fatigue strength of the dovetail attachment calculated by using generalized TSR-CSR diagram and obtained experimentally. An approach on the calculation of the fretting fatigue life of the dovetail attachments by using the critical-plane based Smith-Watson-Topper (SWT) model is presented by Shi et al. [25]. The model takes the stress gradients on the contact surface into the calculation with the use of a weight function. Three different levels of loading is carried out. The study shows that the fatigue life of the dovetail specimen decreases with the increase in the remotely applied load. Hence, it is seen that almost 90% of the fatigue life is consumed at the crack initiation.

1.4 Organization of the Thesis

In Chapter 2, parameters that define contact is presented. Effect of these parameters on the local and global stress results are presented. A simple 2D geometry is chosen for the parametric study.

In Chapter 3, submodelling technique is explained in detail. Firstly, implementation of the submodelling is done on the simple geometry used in Chapter 2. Convergence of the peak values of the stresses is visualized. Secondly, submodelling technique is used on a real aeroengine compressor disc component called dovetail. Location and value of the converged peak stresses at the edge of contact is presented in this chapter.

In Chapter 4, experimental set-up used to demonstrate the dovetail attachment under the presence of centrifugal loading is shown. A tension test is carried out on the

model. Experimental and finite element analysis results are presented in this chapter.

In Chapter 5, conclusions and discussions of the thesis work is presented.

CHAPTER 2

EFFECTS OF CONTACT PARAMETERS ON FINITE ELEMENT RESULTS

Contact mechanics can be considered as the mechanics of solid bodies which are in contact with each other at a point, a line or a plane depending on the problem. Contact mechanics has two driving mechanism which can be summarized as the behaviour in normal direction and the behaviour in tangential direction. In normal direction, compressive and adhesive forces develop and in tangential direction, friction forces develop. Frictional contact mechanics can be defined as the study of the mechanics of bodies in the presence of frictional effects.

In this chapter, effects of the parameters that define contact on the overall and local stress results are presented. For the analysis, a simple 2D model is selected which consists of two rectangular blocks. The simple model is chosen to gain basic knowledge about contact before investigating more complex models. A parametric study is conducted with commercial finite element software package ANSYS v15.0.7.

In Section 2.1 problem geometry, material properties, finite element model and boundary conditions are discussed. In Section 2.2 results of the parametric study are presented. Effects of normal stiffness factor, penetration tolerance factor, elastic slip tolerance, friction coefficient and contact enforcement methods are presented.

2.1 Problem Definition

ANSYS contact and friction parameters are investigated with 2D finite element model of a simple geometry which consists of two plates on top of each other. Details of the geometry, material, finite element model parameters and the loading/boundary conditions are provided in the following sub-chapters.

2.1.1 Geometry

Investigated geometry is shown in Figure 2.1. The lower plate has 60x20x10 mm dimensions and upper plate has 40x20x10 mm dimensions. Bottom corners of the upper block are filleted with a radius of 4 mm.

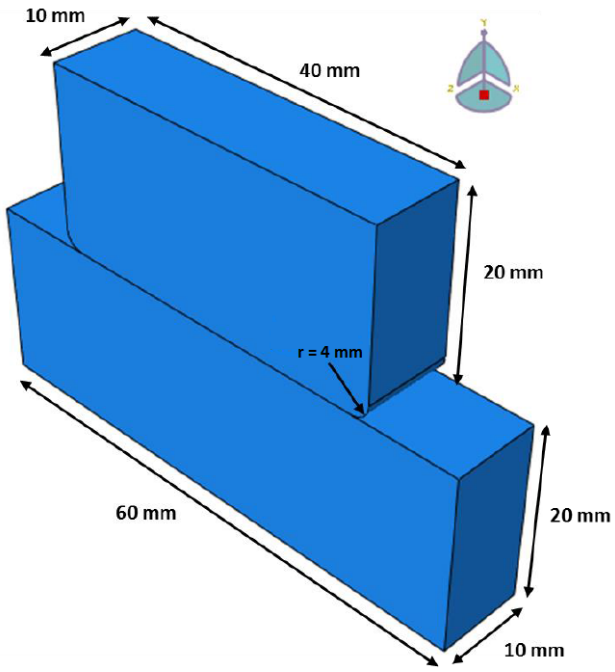


Figure 2.1: Problem Geometry

2.1.2 Material Properties

Material properties of the plates are provided in Table 2.1, are used in the numerical simulations. Material is assumed to have isotropic and linear elastic behaviour.

Table 2.1: Material properties [8]

Elastic Modulus [GPa]	Poisson's Ratio [-]	Density [kg/m^3]
5.2	0.34	1230

2.1.3 Finite Element Model

Figure 2.2 shows the finite element model with 0.25 mm element size on contact region. Finite sliding, surface to surface contact is defined between the part interfaces. CONTA172 type of elements are used for contact elements which represents contact and sliding between 2-D "target" surfaces (TARGE169) and a deformable surface, defined by this element. This type of contact element is located on the surfaces of 2-D solid elements with midside nodes[2]. 4-noded quadrilateral plane stress elements (PLANE182) with reduced integration are used for the bulk material behavior. Plane stress assumption is used. Implicit runs are carried out. Table 3.1 shows the 2D finite element parameters.

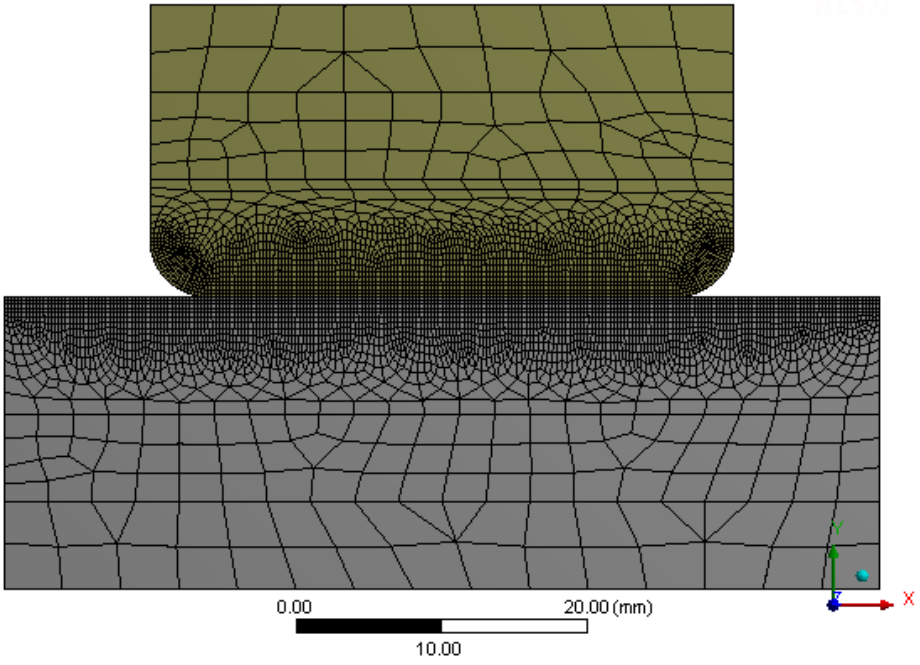


Figure 2.2: 2D finite element model with local 0.25 mm mesh size at the contact region

Table 2.2: ANSYS 2D finite element model properties with contact region properties between the blocks

element size on contact region [mm]	0.25
number of elements	5378
number of nodes	5613
element type	PLANE182

2.1.4 Loading and Boundary Condition

Loading and boundary conditions for the finite element model are shown in Figure 2.3. In Figure 2.3, nodes highlighted with blue and purple colors (letters A and D, respectively) are roller supports. In other words, displacements of A and D are constrained in x and y directions, respectively. Analyses are carried out in two steps with 5 substeps in the first load step and 30 substeps in the second load step. At the first step, a prescribed displacement with a value of 0.16 mm is applied on the nodes highlighted with gray color (letter B) in -y direction and this displacement is kept constant at the second step. In addition to 0.16 mm displacement, a displacement value of 0.25 mm is applied in +x direction on the nodes highlighted with yellow color (letter C) at the second step of the analysis.

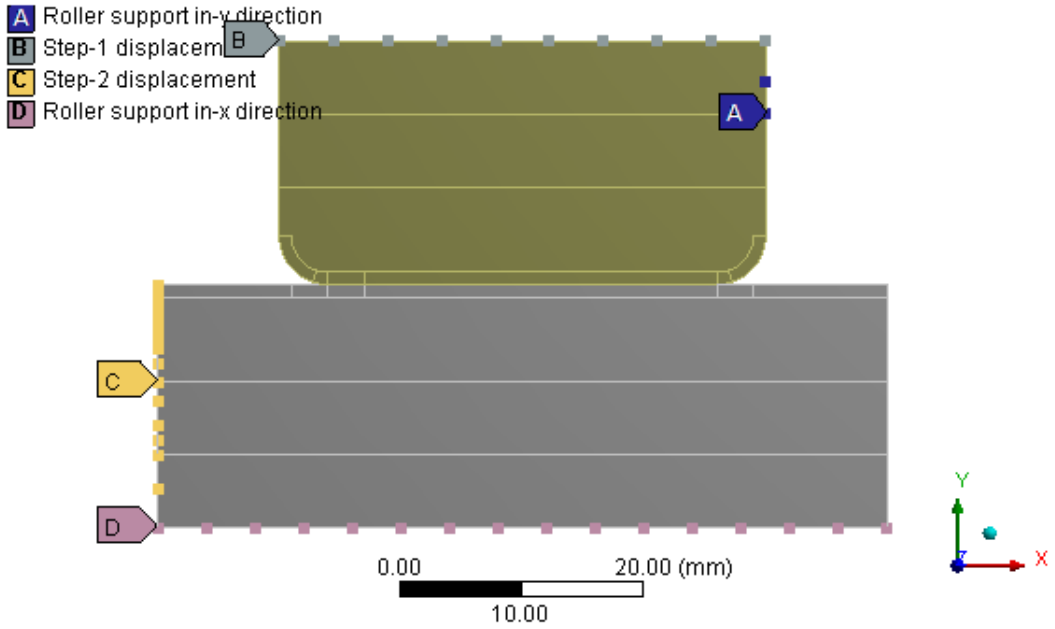


Figure 2.3: Loadings and boundary conditions for the finite element model

2.2 Parametric Study

Contact and friction parameters are usually specified separately in normal and tangential directions in finite element programs. User should specify the desired ones among several possible choices. In ANSYS, there are three possible algorithms to define normal contact properties: Augmented Lagrange Formulation, Pure Penalty Formulation and Normal Lagrange Formulation. There are up to three parameters as inputs depending on the solution formulation to be used. These parameters are given below:

- Augmented Lagrange: The penetration tolerance, the elastic slip tolerance and the normal stiffness factor,
- Pure Penalty: The elastic slip tolerance and the normal stiffness factor,
- Normal Lagrange: The elastic slip tolerance.

In the following subsections, a parametric study is carried out to investigate the effects of some contact and friction parameters on the results. In Subsection 2.2.1, preliminary results of the 2D finite element model discussed in Section 2.1 are presented. The parameters chosen for the parametric study are outlined in this section. Then, the parametric study is conducted to investigate the effects of contact and friction parameters. The investigated parameters are:

- the normal stiffness factor,
- the penetration tolerance factor,
- the elastic slip tolerance factor,
- the friction coefficient,
- the constraint enforcement methods.

2.2.1 Preliminary Results

Due to the loading and the boundary conditions of the problem, high local contact stresses occur at the contact region of both lower and upper blocks. In Figure 2.4, these local contact stress areas are highlighted together with the peak stress location. In Chapter 3, convergence of peak local stresses is discussed in detail. In the context of the parametric study, to determine the effect of contact and friction parameters on the local stresses, a path is defined on the lower block as shown with pink color in Figure 2.5. Origin is located at the bottom left corner of the bottom block. Path starts from x=11 mm and ends at x=17 mm in global coordinates. Contact stress (σ_y) is selected as the output parameter to be used for the parametric study. Stress values on these nodes are compared at end of the second loading step.

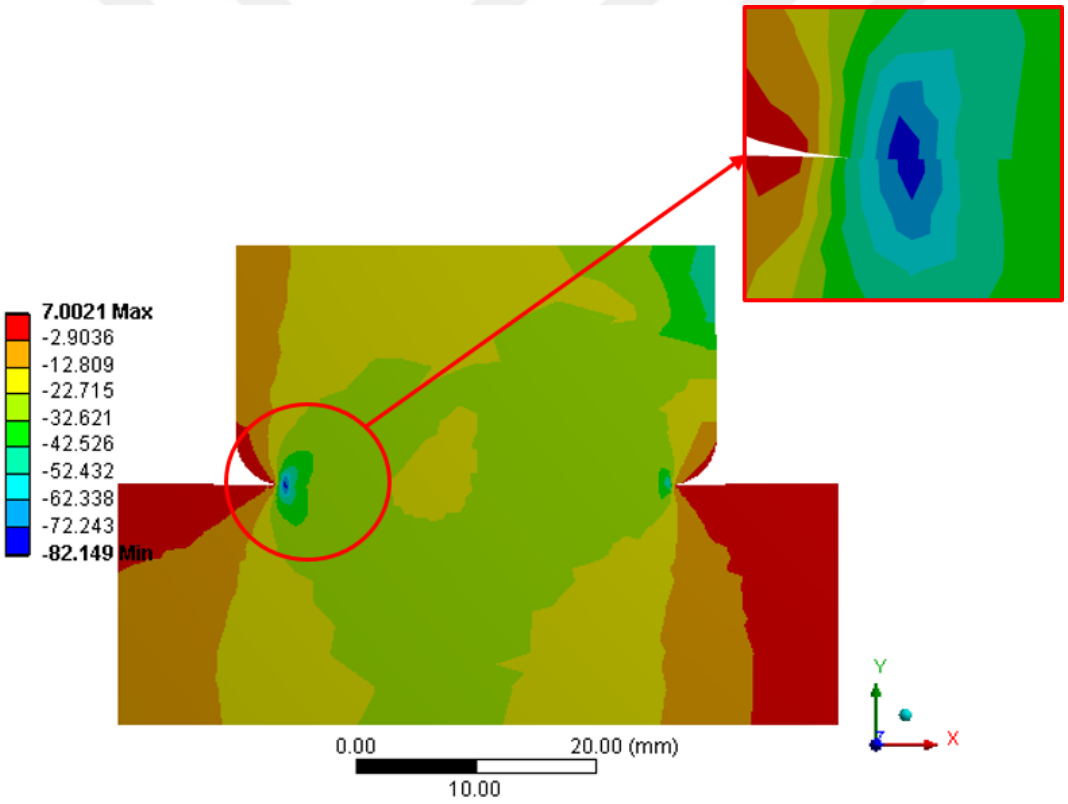


Figure 2.4: Normal stress distribution in y-direction of 2D finite element model

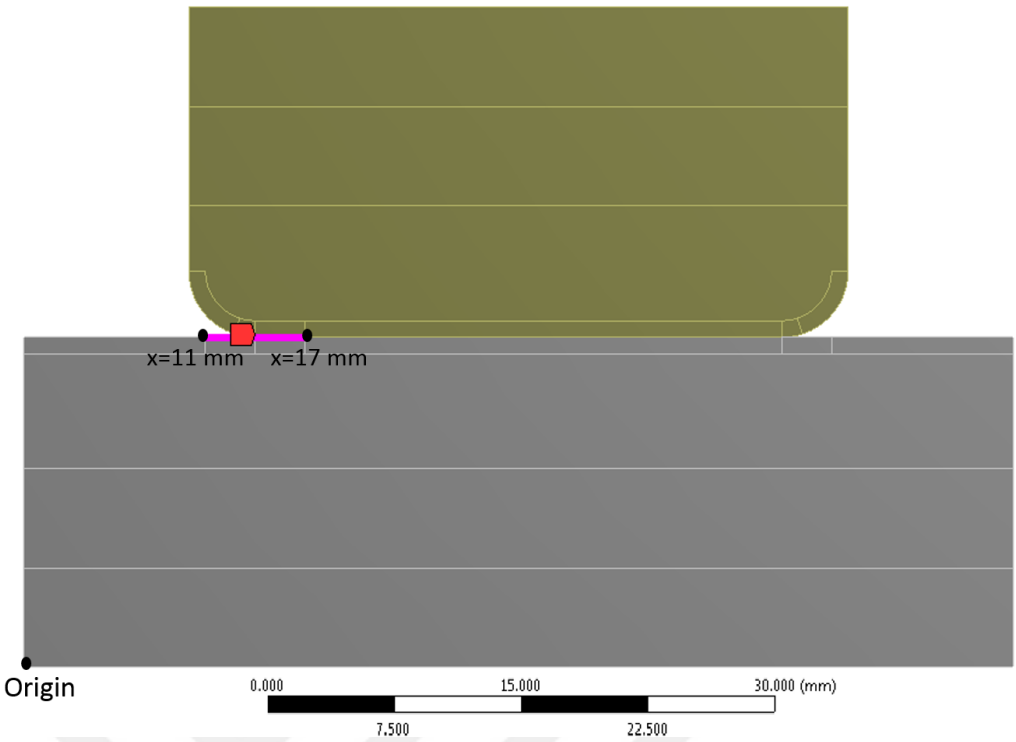


Figure 2.5: The path defined for the stress output (shown in pink)

2.2.2 Effect of Normal Stiffness Factor

For the Augmented Lagrange and the Penalty methods, the normal and the tangential contact stiffness values need to be specified. The amount of penetration between contacting surfaces depends on the normal stiffness. The amount of sticking between contact bodies depends on the tangential stiffness. Higher stiffness values decrease the amount of penetration/elastic slip, but can lead to ill-conditioned global stiffness matrices and to convergence difficulties. Lower stiffness values can lead to a certain amount of penetration/elastic slip and may produce inaccurate results. It should be preferred a high enough stiffness that the penetration/elastic slip is acceptably small and low enough stiffness that the problem will well-behave in terms of convergence [2].

The normal stiffness can either be directly specified or through a factor in ANSYS. Effects of the normal stiffness factor are investigated for five values of the factor, i.e., 0.1, 0.5, 1, 1.5, and 2 for three different mesh sizes. The contact stiffness values corresponding to the stiffness factors and contact elements mesh sizes are given in Table

2.3. From Table 2.3, it can be seen that the normal stiffness is calculated by scaling the underlying element stiffness with the normal stiffness factor (fkn). Hence, it is seen that the contact stiffness is inversely proportional to mesh size of the contact elements. The relationship between the normal stiffness factor and the normal stiffness is given in Equation 2.1. Combining Equation 2.1 with Table 2.3, the scaling factor (C) used by ANSYS for the model problem is found as 20. An example of calculation of normal stiffness for 5200 MPa Young's modulus, 0.1 normal stiffness factor and mesh sizes of 0.25 mm is given in Equation 2.2.

$$normal\ stiffness = fkn \times \frac{C}{h} \times E \tag{2.1}$$

$$normal\ stiffness = (0.1) \times \frac{20}{0.25} \times (5200\text{MPa}) = 416000\text{MPa} \tag{2.2}$$

A total of 15 finite element models are created in ANSYS for the normal stiffness factor values of 0.1, 0.5, 1, 1.5 and 2 for three different mesh sizes of 0.5, 0.25 and 0.125 mm (Table 2.4) while keeping all the other parameters constant at 0.3 friction coefficient, the Augmented Lagrange formulation, 0.1 penetration tolerance factor and 0.01 elastic slip tolerance factor.

Table 2.3: Relationship between the normal contact stiffness factor and the normal contact stiffness

Normal Stiffness Factor (fkn)	**Mesh Size on Contact [mm]**	**Normal Contact Stiffness [MPa]**
0.1	0.25	41600
	0.5	20800
0.5	0.25	208000
	0.5	104000
1	0.25	416000
	0.5	208000
1.5	0.25	312000
	0.5	624000
2	0.25	832000
	0.5	416000

Local contact stresses and their peak location are exported for each normal stiffness factor. In Figure 2.6, change in the peak of the contact stress ($\sigma_{y,max}$) for 5 different normal stiffness factors for the mesh size of 0.25 mm is given. It can be deduced

Table 2.4: 2D finite element model properties for the parametric study of the normal stiffness factor

Mesh Size [mm]	Number of Elements	Number of Nodes
0.5	1856	1987
0.25	5293	5528
0.125	15214	15676

that for lower values of the normal stiffness factor, $\sigma_{y,max}$ varies with the change in normal stiffness factor, whereas after a value of 1 (the default value of ANSYS) the peak stress no longer depends on the change. It is known that higher values of normal stiffness factor makes convergence harder. Therefore, the normal stiffness factor cannot be chosen arbitrarily large. It can be concluded that an optimum value of normal stiffness factor can be chosen around 1.

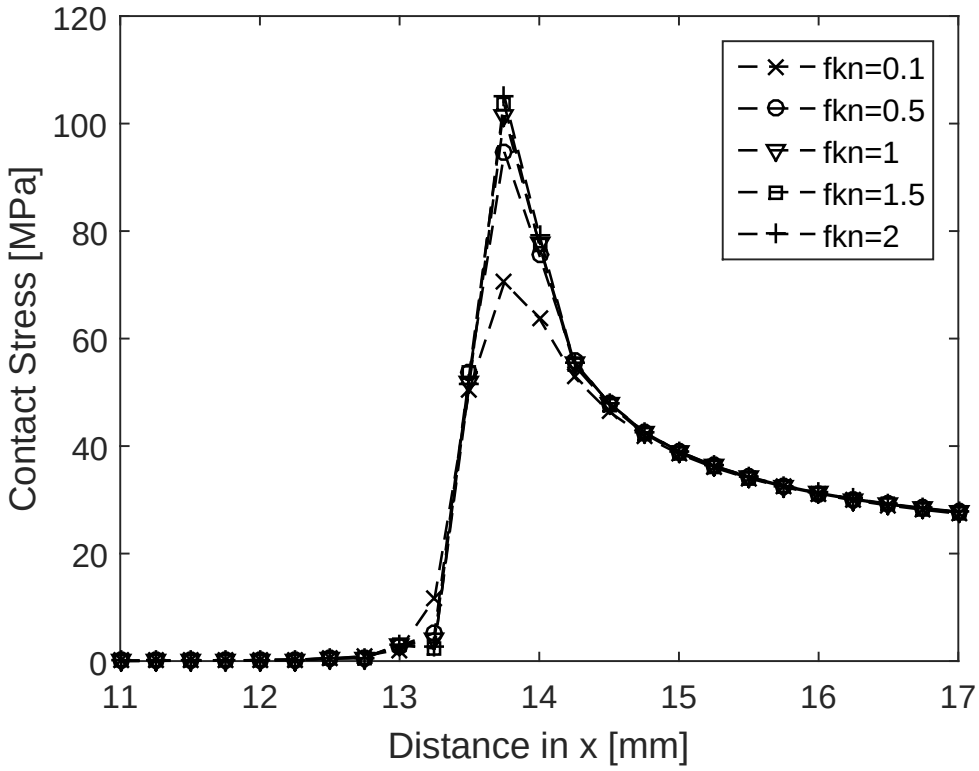


Figure 2.6: Contact stress for 5 different normal stiffness factors for mesh size of 0.25 mm

From Figure 2.7, it is seen that choosing a finer mesh also makes the solution more precise. The maximum stress values for mesh sizes 0.25 mm and 0.125 mm are close

to each other, whereas stress values for mesh size of 0.5 mm varies from the values of the other two meshes. The convergence problem of the maximum stress will be discussed in details in Chapter 3. In the same figure, it is seen that two design points for the mesh size of 0.125 mm are missing at the normal stiffness factor values of 1.5 and 2. The reason is that in these analyses convergence could not be obtained. This result justifies that high contact stiffness factors may yield convergence difficulties.

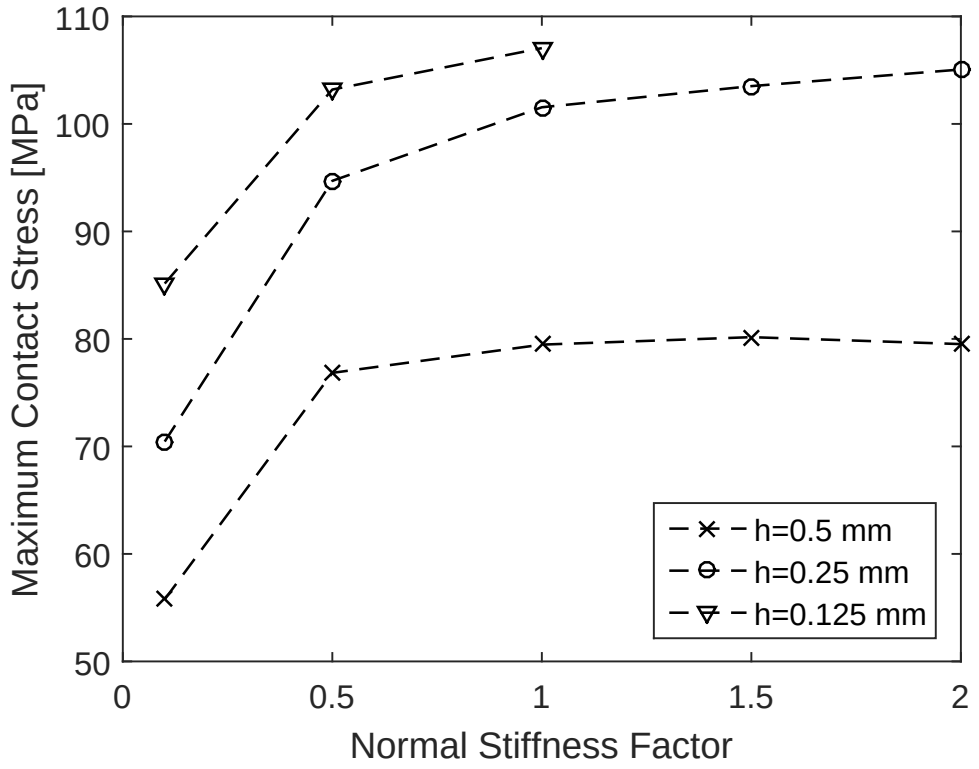


Figure 2.7: The maximum contact stress for 5 different normal stiffness factors for three mesh sizes

Table 2.5 shows CPU time for contact stiffness parametric study. It can be observed that the solution time increases considerably with the decrease in mesh size. It is also seen that as the mesh size gets smaller, the normal stiffness factor has an impact on the solution time. For smaller mesh sizes, increase in the normal stiffness factor also increases the solution time.

Table 2.5: Finite element model solution time for the normal stiffness factor study

Mesh Size on Contact [mm]	Normal Stiffness Factor (fkn)	Time Spent Computing Solution [s]
0.125	0.1	89.2
	0.5	103.3
	1	169.7
	1.5	No convergence
	2	No convergence
0.25	0.1	30.5
	0.5	29.3
	1	35.9
	1.5	43.6
	2	72.1
0.5	0.1	11.7
	0.5	12.8
	1	12
	1.5	11.8
	2	12

2.2.3 Effect of Penetration Tolerance Factor

When two bodies get into contact, physically there is no penetration between bodies [17]. However, to solve contact problem numerically, finite element programs allow some penetration between target and contact surfaces. It may be explained as placing stiff springs on contact surfaces which has a stiffness value proportional to the normal contact stiffness and have maximum allowable deflection which is defined by the penetration tolerance factor (ftoln). Directly a penetration tolerance value or a factor can be set in ANSYS for Augmented Lagrange and Pure Penalty algorithms. The penetration tolerance can be increased from the default value to ease the convergence. Table 2.6 shows the resulting penetration tolerance for the given factors for contact elements with a size of 0.25 mm. It can be seen that the penetration tolerance factor and the resulting penetration tolerance is linearly proportional with a factor of contact element mesh size (h). The relationship between them is given in Eqution 2.3.

$$resulting\ penetration\ tolerance = ftoln \times h \tag{2.3}$$

Table 2.6: The relationship between the penetration tolerance factor and the resulting penetration tolerance for h=0.25 mm

Penetration Tolerance Factor (ftoln)	**Resulting Penetration tolerance [mm]**
0.05	0.0125
0.1	0.0249
0.5	0.1247
0.9	0.2245

Effect of the penetration tolerance factor is investigated for only 0.25 mm element size. Other than the penetration tolerance factor, other parameters are kept costant at, 0.3 friction coefficient, Augmented Lagrange formulation, 1 normal stiffness factor and 0.01 elastic slip tolerance factor. A total of 4 runs were conducted for the penetration tolerance factors of 0.05, 0.1, 0.5 and 0.9. Figure 2.8 shows the contact stress values (σ_y) the selected part of the contact for the corresponding penetration tolerance factors. It can be seen that, results are almost same for different factors expect at the neighbourhood of $\sigma_{y,max}$ location. However, as the penetration tolerance factor increases, $\sigma_{y,max}$ decreases, which gives unreliable results. Decrease in $\sigma_{y,max}$ is bigger as the penetration tolerance factor exceeds the program default value of 0.1. It can be concluded that an optimum value of penetration tolerance factor can be chosen around 0.1.

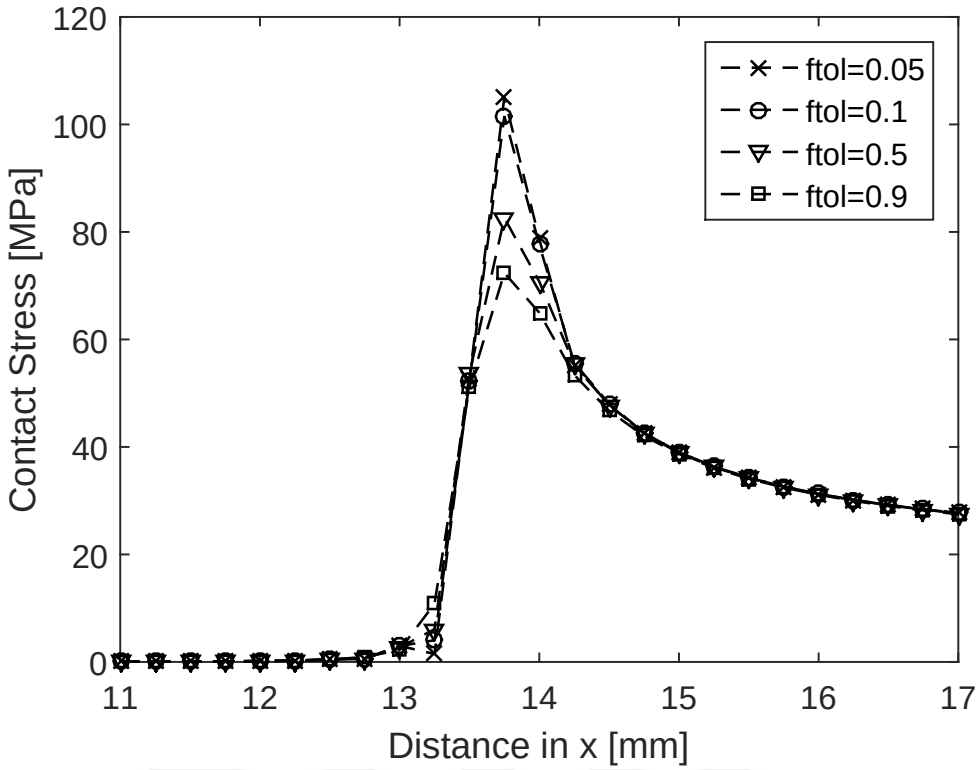


Figure 2.8: The contact stress on the selected path for 4 different penetration tolerance factors for mesh size of 0.25 mm

2.2.4 Effect of Elastic Slip Tolerance Factor

For the contact cases with friction, an analogous situation to normal behaviour occurs for the tangential behaviour. Until the frictional shear stress exceeds a limiting value defined by the friction coefficient, the contact nodes are in sticking condition. It is desired to have zero slip in penalty based methods; however, similar to the normal behaviour, to have a convergent numerical solution there exists a slip which is related to the tangential contact stiffness. This tangential contact stiffness is calculated automatically in ANSYS [17]. However, the elastic slip can be set in ANSYS as a factor or a value. An elastic slip tolerance can be used to ease the convergence. It sets a small elastic relative movement between the contacting surfaces before the irreversible slip of the surfaces. By default, the elastic slip tolerance is set to zero that is no relative movement of contacting surfaces are allowed before the critical frictional force [6]. In this part of the study, the elastic slip tolerance is varied while keeping the other

parameters constant at 0.3 friction coefficient, the Augmented Lagrange formulation, 1 normal stiffness factor factor and 0.1 penetration tolerance factor. A total of 4 runs have been conducted for the elastic slip tolerance values of 0.005, 0.01, 0.05 and 0.1. Figure 2.9 shows the contact stress values (σ_y) on the selected part of the contact surface for the corresponding elastic slip tolerance factors. It can be observed that the change in elastic slip tolerance has no effect on either the peak contact stress ($\sigma_{y,max}$) or the contact stress(σ_y) on any location.

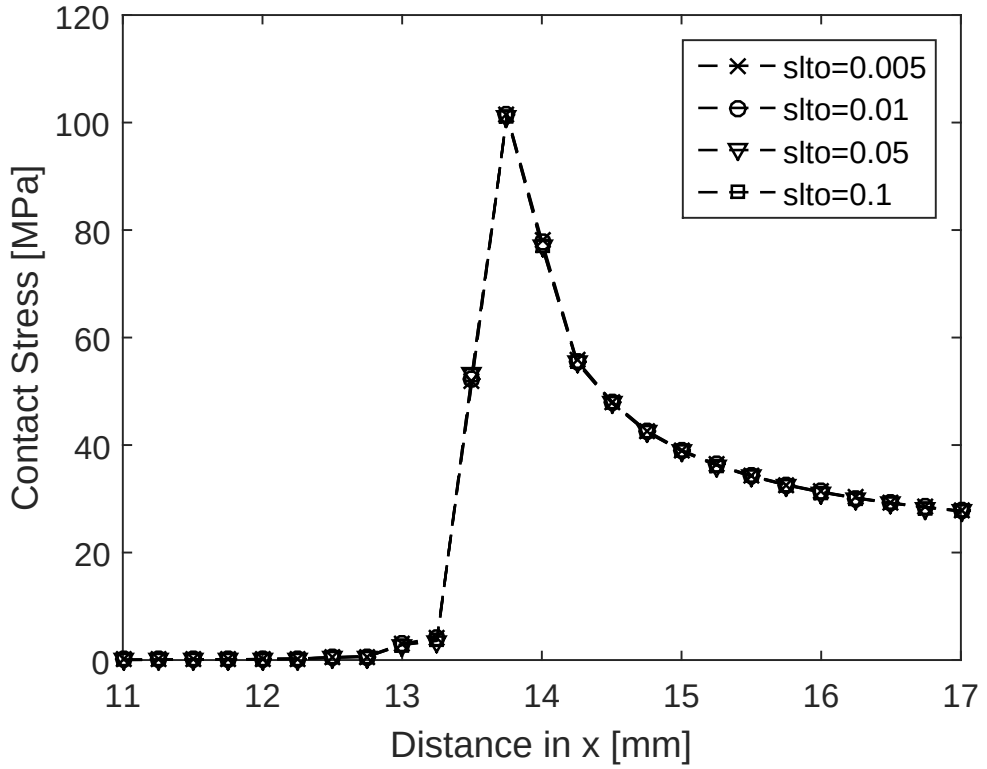


Figure 2.9: The contact stress on the selected path for 4 different elastic slip tolerance factors for mesh size of 0.25 mm

2.2.5 Effect of Friction Coefficient

Amanton's law of friction is used as the friction formulation by ANSYS [2]. Under slipping condition, formulation used is given in Equation 2.4.

$$\tau_{xy} = \mu \times \sigma_y \tag{2.4}$$

Four different friction coefficients are investigated in this part which are 0.2, 0.3, 0.5 and 0.7. Figure 2.10 shows the contact stress values (σ_y) on the selected part of the contact surface for the corresponding friction coefficients. It can be deducted that the friction coefficient has an impact on the peak contact stress ($\sigma_{y,max}$) whereas its effect on other points of contact is more negligible. Hence, it should be noted that for friction coefficient of 0.5 and 0.7, no partial slip occurs between bodies and contact is in "sticking" condition. Because of that reason the peak contact stresses for the two parameters are the same. On the other hand, for the friction coefficients of 0.2 and 0.3, the contact is in "sliding" condition and the peak contact stress seems to be dependent on friction coefficient.

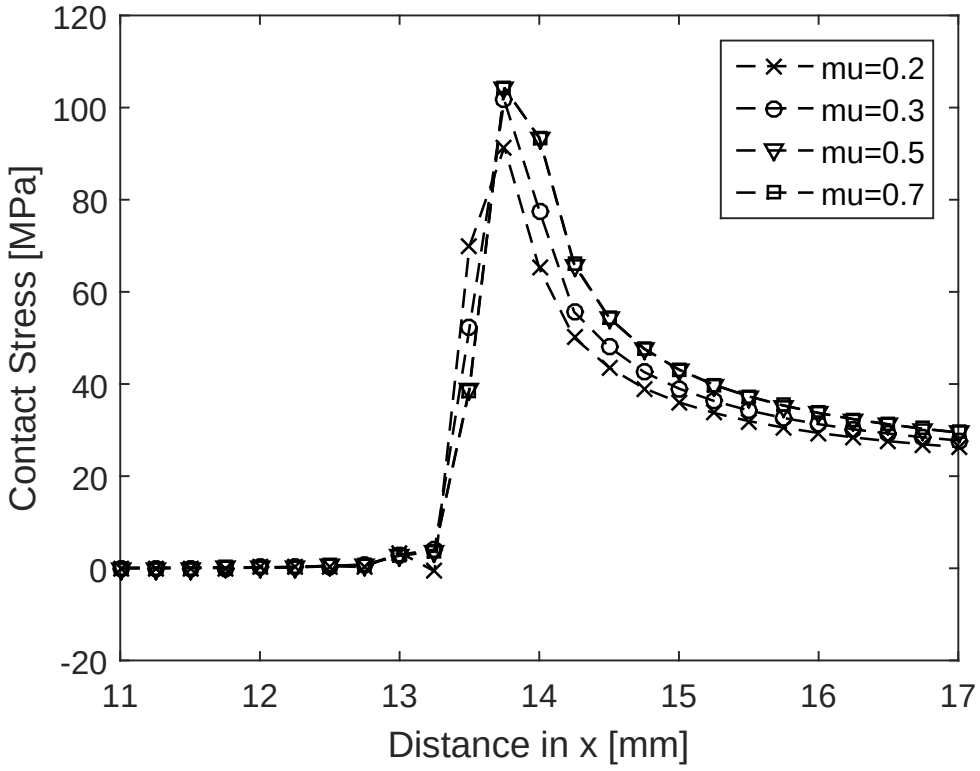


Figure 2.10: The contact stress on the selected path for 4 different friction coefficients for mesh size of 0.25 mm

2.2.6 Effect of Constraint Enforcement Methods

For classical stress analysis problems under small deformations hypothesis, the potential energy functional $\prod(\mathbf{u})$ of a deformable body is defined as shown in Equation

2.5 [16].

$$\prod^{(i)}(\mathbf{u}^{(i)}) := \int_{\Omega^{(i)}} W^{(i)} d\Omega - \int_{\Omega^{(i)}} \mathbf{f}^{(i)} \cdot \mathbf{u}^{(i)} d\Omega - \int_{\Gamma_\sigma^{(i)}} \bar{\mathbf{t}}^{(i)} \cdot \mathbf{u}^{(i)} d\Gamma \tag{2.5}$$

In Equation 2.5, $W^{(i)}$ is defined as the stored elastic energy per volume in body $\Omega^{(i)}$. Minimization of the potential functional given in above equation is constructed for problems without contact. It leads to an optimization problem without any constraints. However, contact is a constraint itself and for problems including contact, an extra energy term $\prod^{(c)}$ is added to above equation as given in Equation 2.6.

$$\prod(\mathbf{u}, \lambda_N) := \sum_{i=1}^{2} \prod^{(i)}(\mathbf{u}^{(i)}) + \prod^{(c)}(\mathbf{u}) d\Gamma \tag{2.6}$$

To solve this optimization problem, ANSYS uses three constraint enforcement methods: Normal Lagrange, Pure Penalty and Augmented Lagrange methods. $\prod^{(c)}$ term and its parameters vary for each method chosen for the enforcement of contact constraints. Details of the $\prod^{(c)}$ for each method will be presented in following subsections.

2.2.6.1 Normal Lagrange Method

For a frictionless contact, the contribution of the potential energy functional to the global functional due to contact is given in Equation 2.7 [16].

$$\prod^{(c)}(\mathbf{u}, \lambda_N) = \int_{\Gamma_c} \lambda_N g d\Gamma \tag{2.7}$$

The global functional becomes

$$\prod^{(lagrange)}(\mathbf{u}, \lambda_N) = \prod(\mathbf{u}) + \int_{\Gamma_c} \lambda_N g d\Gamma, \tag{2.8}$$

where λ_N is the Lagrange multiplier in the normal direction and g is the penetration along the normal and tangential direction. Combining Equation 2.5 with Equation

2.8, the directional derivative of the functional at solution point ($\mathbf{u}$, λ_N) can be given as:

$$\begin{aligned} 0 = D_u \prod^{(lagrange)} \cdot \boldsymbol{\omega} &= \frac{d}{d\alpha}\Big|_{\alpha=0} \prod^{(lagrange)} (\mathbf{u} + \boldsymbol{\omega}, \lambda_N) \\ &= \sum_{i=1}^{2} \left\{ \int_{\Omega} \omega_{jk}^{(i)} \sigma_{jk}^{(i)} d\Omega^{(i)} - \int_{\Omega^{(i)}} \omega_j^{(i)} f_j d\Omega^{(i)} \right. \\ &\left. - \int_{\Gamma_\sigma^{(i)}} \omega^{(i)} \bar{t}_j^{(i)} d\Gamma^{(i)} + \int_{\Gamma_c}^{(1)} \lambda_N \delta g d\Gamma \right. \end{aligned} \tag{2.9}$$

for all posible variations of ω that satisfy necessary continuity and smoothness properties

$$\int_{\Gamma_c} (\lambda_N - q_N) g d\Gamma \geq 0 \tag{2.10}$$

and for admissible variations of $q_N \geq 0$ of λ_N. With the implementation of the classical Kuhn-Tucker optimality conditions, the inequality given in Equation 2.10 can be replaced as:

$$\lambda_N \geq 0 \tag{2.11a}$$

$$g(x) \leq 0 \tag{2.11b}$$

$$\lambda_N g = 0 \tag{2.11c}$$

Equation 2.11a gives the condition that non-zero contact force/pressure will develop. Equation 2.11b ensures the condition of no penetration for this algorithm. For the case given in Equation 2.11c, either $\lambda_N = 0$ which is no contact condition or $g_N = 0$, non-zero compressive contact forces will develop. Adhesion condition is not taken into the consideration for this solution. It should be noted that for frictional contact two extra terms which includes λ_t and g_t will be added to Equation 2.7, which formulates the behaviour in tangential direction.

2.2.6.2 Pure Penalty Method

The advantage of the Penalty method to the Lagrange method is that it explicitly removes the constraints due to the variational formulation. The Penalty method transforms a constraint problem to an unconstrained optimization problem. For the frictionless contact, the extra potential energy functional added to system due to the penalty formulation is given in Equation 2.12 [16].

$$\prod^{(c)}(\mathbf{u}) = \int_{\Gamma_c^{(1)}} \epsilon_N \langle g \rangle^2 d\Gamma \tag{2.12}$$

ϵ_N is defined as a positive penalty parameter. Definition of the Macauley bracket in above equation is given in Equation 2.13.

$$\langle \mathbf{g} \rangle = \begin{Bmatrix} g \; if \; g \geq 0 \\ 0 \; if \; g < 0 \end{Bmatrix}, \tag{2.13}$$

Substituting Equation 2.12 into the global functional, one can get the modified global potential energy functional of pure penalty method as shown below.

$$\prod^{(penalty)}(\mathbf{u}) = \prod(\mathbf{u}) + \int_{\Gamma_c^{(1)}} \epsilon_N \langle g \rangle^2 d\Gamma \tag{2.14}$$

Then the solution is obtained by minimizing the potential energy functional given in Equation 2.14 by rendering it as stationary to variations in $\mathbf{u}$ in arbitrary directions parameterized by $\boldsymbol{\omega}$.

$$\begin{aligned} 0 = D_u \prod^{(penalty)} \cdot \boldsymbol{\omega} &= \frac{d}{d\alpha}\Big|_{\alpha=0} \prod^{(lagrange)}(\mathbf{u} + \boldsymbol{\omega}, \lambda_N) \\ &= \sum_{i=1}^{2} \left\{ \int_{\Omega} \omega_{jk}^{(i)} \sigma_{jk}^{(i)} d\Omega^{(i)} - \int_{\Omega^{(i)}} \omega_j^{(i)} f_j d\Omega^{(i)} \right. \\ &\left. - \int_{\Gamma_\sigma^{(i)}} \omega^{(i)} \bar{t}_j^{(i)} d\Gamma^{(i)} + \int_{\Gamma_c^{(1)}} \epsilon_N \langle g \rangle^2 d\Gamma \right. \end{aligned} \tag{2.15}$$

2.2.6.3 Augmented Lagrange Method

The Augmented Lagrange method can be explained as the combination of the Normal Lagrange and Penalty methods. It represents the exact contact constraints from the Lagrange method and uses penalty terms to ease the solution procedure. For a frictionless contact, the extra potential energy functional added to the system due to the Augmented Lagrange formulation is given in Equation 2.16 [16].

$$\prod^{(c)}(\mathbf{u}, \lambda_N) = \int_{\Gamma_c^{(1)}} \left[\frac{1}{2\epsilon_N} \langle \lambda_N + \epsilon_N g \rangle^2 - \frac{1}{2\epsilon_N} \lambda_N^2 \right] d\Gamma \tag{2.16}$$

In above equation, it is seen that the potential energy functional due to contact has terms of both the Lagrange method (λ_N) and the Penalty method (ϵ_N). Substituting Equation 2.16 into the global functional, one can get the modified global energy functional of the Augmented Lagrange method as shown below.

$$\prod^{(augmented)}(\mathbf{u}, \lambda_N) = \prod(\mathbf{u}) + \int_{\Gamma_c^{(1)}} \left[\frac{1}{2\epsilon_N} \langle \lambda_N + \epsilon_N g \rangle^2 - \frac{1}{2\epsilon_N} \lambda_N^2 \right] d\Gamma \tag{2.17}$$

Similar to the penalty method $\epsilon_N > 0$ and it is a user-defined parameter. The case when $\lambda_N = 0$, the penalty functional is obtained in Equation 2.16. By rendering Equation 2.17 stationary with respect to both $\mathbf{u}$ and λ_N, one can obtain the solution of the Augmented Lagrange method as given below.

$$\begin{aligned} 0 = D_u \prod^{(augmented)} \cdot \boldsymbol{\omega} &= \frac{d}{d\alpha}\Big|_{\alpha=0} \prod^{(augmented)} (\mathbf{u} + \boldsymbol{\omega}, \lambda_N) \\ &= \sum_{i=1}^{2} \left\{ \int_{\Omega} \omega_{jk}^{(i)} \sigma_{jk}^{(i)} d\Omega^{(i)} - \int_{\Omega^{(i)}} \omega_j^{(i)} f_j d\Omega^{(i)} \right. \\ &\quad \left. - \int_{\Gamma_\sigma^{(i)}} \omega^{(i)} \bar{t}_j^{(i)} d\Gamma^{(i)} + \int_{\Gamma_c^{(1)}} \langle \lambda_N + \epsilon_N g \rangle \delta g d\Gamma \right. \end{aligned} \tag{2.18}$$

and

$$\frac{1}{\epsilon_N} \int_{\Gamma_c^{(1)}} \left[\langle \lambda_N + \epsilon_N g \rangle^2 - \lambda_N \right] q_N d\Gamma = 0 \tag{2.19}$$

2.2.6.4 Comparison of Contact Enforcement Methods

In Table 2.8, a general comparison between contact enforcement methods are presented. Each method has its advantageous at certain points and weaknesses as well. For the model problem, in this part of the study, three contact enforcement methods are compared while keeping the other parameters constant at 0.3 friction coefficient, 1 normal stiffness factor factor, 0.1 penetration tolerance factor and 0.01 elastic slip tolerance factor. A total of 3 runs have been conducted for 3 methods. Figure 2.11 shows the contact stress values (σ_y) on the selected part of the contact surface for the corresponding enforcement methods. It can be observed that the change in enforcement method has no effect on either the peak contact stress ($\sigma_{y,max}$) or contact stress (σ_y) at any location. Solution times for the three methods are given on Table 2.7. It is seen that there is no difference between the solution times for the three methods.

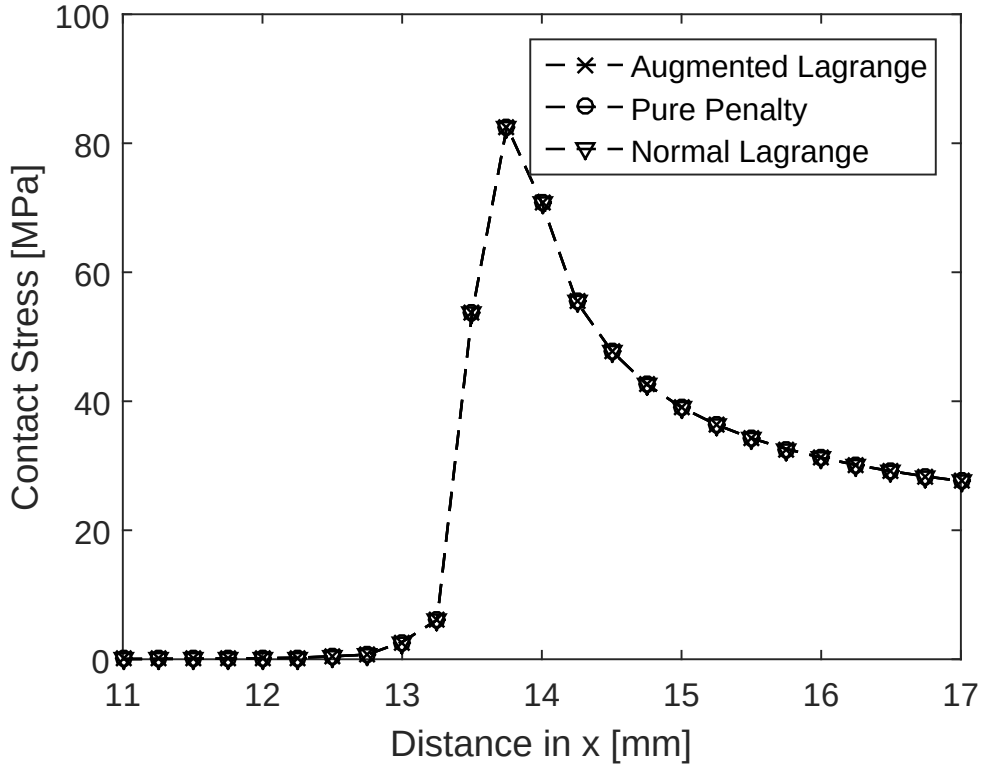


Figure 2.11: Contact stress for 3 different contact enforcement methods for mesh size of 0.25 mm

Table 2.7: Solution times of the constraint enforcement methods: the Normal Lagrange method, the Pure Penalty method and the Augmented Lagrange method

	Pure Penalty	**Augmented Lagrange**	**Normal Lagrange**
Solution Time [s]	67.6	67.7	67.6

Table 2.8: Pros and cons of contact enforcement methods

Pure Penalty	**Augmented Lagrange**	**Normal Lagrange**
Good convergence behaviour (few equilibrium iterations)	For the cases of large penetrations, additional equilibrium iterations may needed	For the case of chattering additional equilibrium iterations may needed
Results are very sensitive to the normal contact stiffness selection	Results are less sensitive to the normal contact stiffness selection than pure penalty method	Normal stiffness factor is not an input
Contact penetration occurs and can not be controlled	Contact penetration occurs, but can be becontrolled to some degree	No penetration occurs between bodies
Both direct or iterative solvers can be used	Both direct or iterative solvers can be used	Only direct solver can be used
Symmetric or asymmetric contact options are available	Symmetric or asymmetric contact options are available	Asymmetric contact option is available
Contact detection at integration points	Contact detection at integration points	Contact detection at nodes

CHAPTER 3

SUBMODELLING

In aerospace field, safety of the air vehicle is the main concern of the engineers. The engine designers tries to design their engines by meeting the requirements of longer operation life, high thrust to weight ratio [18]. In engineering problems, failure due to the stress concentrations in local areas are most commonly encountered. Accurate prediction of these stress concentrations are a challenge in the finite element analysis. One of the methods to overcome this challenge is the submodelling approach [22].

In Section 3.1, the singular and nonsingular stress state on the contact edges are discussed. In the following Section 3.2, implementation of the submodelling technique on models with peak edge of contact stresses is explained. In Sections 3.3 and 3.4, the submodelling technique is used on the model discussed in Section 2.1 and on a real aeroengine component "dovetail joint".

3.1 Singular and Nonsingular Edge of Contact Stresses on Contact Problems

Submodelling procedure can briefly be described as cutting out a critical section of a global model and modelling it separately by taking its boundary conditions from previously solved coarser global model. Extracted boundary conditions are applied to the boundaries of the substracted submodel. The reason for such an operation is quite obvious. To have a converged sought-after stress, one needs to have a mesh fine enough in the critical region so that the stress will no longer be dependent on the mesh size. However, following such a procedure on a global model will not be computationally efficient. Hence, because of the complexity of the superfine global model,

it may not usually possible to have a converged solution with a normal computation system. Nevertheless, following the submodelling procedure explained in this thesis work, one can have a reliable model without requirement of a high computational resource.

To begin with, it is vital to show that stresses occurring near the edge of contact are not singularities and can be converged to a finite value with successive mesh refinement. For this reason, Sinclair et. al. [26] presented the solutions of three types of edge contact problems from classical elasticity. In Figure 3.1a, contact bodies having profiles of a cylindrical roller, a polynomial profile and a flat punch with sharp corners are shown. These contact profiles share same contact area of 2a with bottom elastic half-space. Corresponding stress values of each profile are given in Hertz [13], Steuermann [28] and Sadowsky [15], respectively. These stresses are plotted in Figure 3.1b, where σ_c is the absolute value of contact stress and it is normalized by using average contact stress $\bar{\sigma}_c$ throughout the contact region. Local radius of curvature on the contact area for the three profiles can be defined as R. Hence, for these profiles, R/a ratio is defined as $R/a > 1$ for roller, $R/a \approx 1$ for the polynomial profile and $R/a = 0$ for flat punch. From Figure 3.1b, it is seen that as R/a decreases edge of contact stress tends to increase and for the flat punch it diverges to infinity. For most dovetail attachments, this ratio is in the range of $1/4 < R/a < 1$. For this reason, contact stress profile of dovetail attachments are expected to be something in between of polynomial profile and flat punch, which justifies the non-singular finite stress state at the edge of contact for dovetail joints.

Sinclair et. al. [26] further proves the case of non-singular stress state by considering the rigid roller example given in Figure 3.1. Conforming frictionless contact is assumed between bodies. Conforming means that contact and target bodies share a common tangent from zero load to final load step. In the Figure 3.1, this tangent is the line $|CC'|$. For the rigid roller, local boundary condition at point C take the form

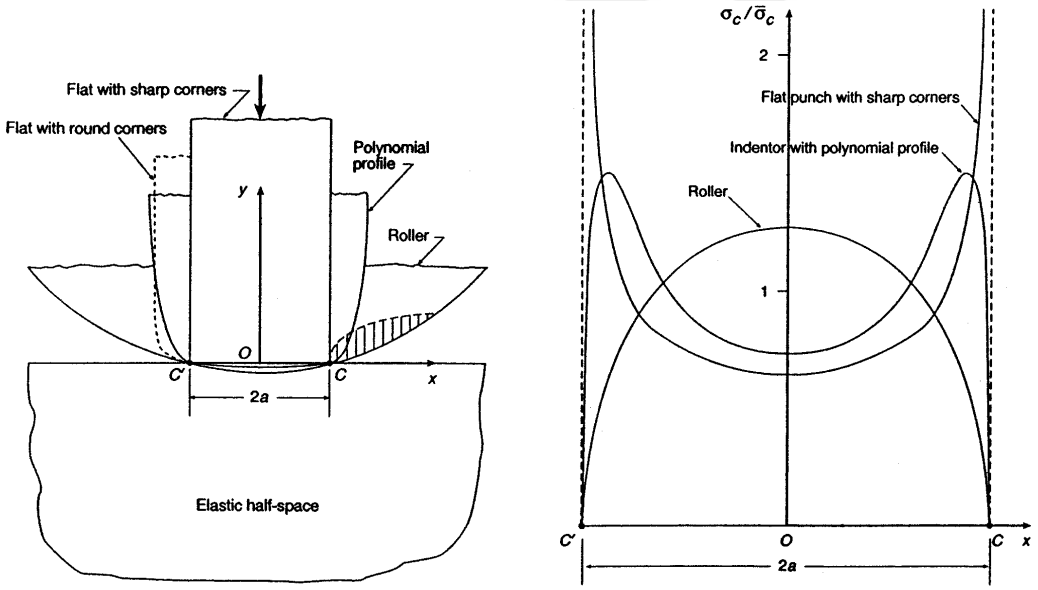
$$\begin{aligned} \sigma_y = \tau_{xy} = 0 \quad &\text{on} \quad y = 0,\ |x| > a, \\ \nu = -\nu_0, \tau_{xy} = 0 \quad &\text{on} \quad y = 0,\ |x| < a, \end{aligned} \tag{3.1}$$

where σ_y, τ_{xy} are stress components in cartesian coordinate system given in Figure 3.1

and ν is the displacement in y-direction. First part of Equation 3.1 is the stress state at the external contact region. Second part governs the stress condition at the contact which has non-zero σ_y and ν_0 amount of penetration between bodies. τ_{xy} equals to zero due to the nature of frictionless contact. Moreover, two more physically sensible constraints may be added to system as given in Equation 3.2.

$$\begin{aligned} \sigma_y &\leq 0 \quad \text{on} \quad y = 0,\ |x| < a, \\ \nu &< \sqrt{R^2 - a^2} - \sqrt{R^2 - x^2} \quad \text{on} \quad y = 0,\ |x| > a, \end{aligned} \tag{3.2}$$

First part of the constraint equation yields the condition of non-zero compressive stress between contacting bodies in the contact region and the second part constraints no penetration condition at the external contact region. It should be noted that at the second part of the equation for x values greater than R, constraint equation yield complex results. However, it is not realistic, since those x values yield the condition on the free surface that does not have a possibility of getting into contact.



(a) Contact bodies profiles

(b) Contact stresses

Figure 3.1: Classical elasticity examples of contact problems [26]

For this contact problem, there are two cases for singular stresses to occur. First case is that, the singular stresses will have a positive stress intensity factor. To have singular non-zero stress state, one should approach to the point C within contact region

($x < a$) as stated in the second part of Equation 3.1. However, having positive non-singular stress will violates the first constraint of Equation 3.2. Second case is that, the singular stresses will have a negative stress intensity factor. Under this condition, the penetrated body (roller) will have vertically upwards displaced shape just outside of point C (highlighted as hatched area in Figure 3.1a. As a result of this condition, penetration will occur at $x > a$ which violates the second part of 3.2.

Having justified that the sharp corners at the contact result singularities, for the models introduced in this thesis work R/a ratio's are within desired limits and it is possible to have converged results with successive mesh refinement.

3.2 Procedure

Following the procedure given below, the submodelling technique can be implemented to any case involving non-singular edge of contact stress. Procedure mostly follows the submodelling method introduced in [9].

1. A coarse global model may be solved to see the peak edge of contact stress that is desired to be converged with the implementation of submodelling technique.

2. Having determined the critical area to be investigated by the submodelling, a boundary layer which includes this region is defined. This boundary layer will have the shape similar to the contact area shape and will have a thickness value of roughly one-fourth of the nearest radius of curvature. An example of the boundary layer is given in Figure 3.2. Area highlighted with green is the boundary layer.

3. The reason for such a boundary layer implementation is that it is not usually possible and necessary to have a uniform mesh throughout the all sections of global model. However, in the boundary layer it is achievable.

4. Depending upon the size of the boundary layer and the available computational facility, a coarse mesh grid is implemented to the boundary layer of the global model.

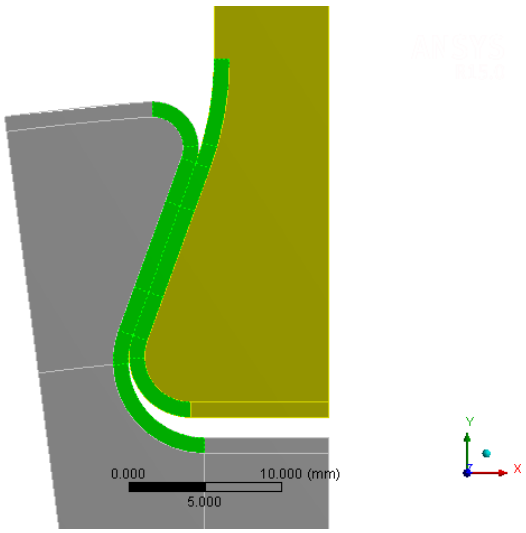


Figure 3.2: Boundary layer for the dovetail model

5. Outside of the boundary layer, number of divisions are defined to some edges. Rest of the mesh is automatically generated by ANSYS.

6. From the coarse (C) global model, by systematically halving the element edge sizes inside of the boundary layer, medium (M) and fine (F) global grids are created.

7. To see the convergence behaviour of the maximum stress value, convergence check given in Equation 3.3 may be used. Superscripts C, M and F used in below equation denotes the maximum stress value corresponding to the coarse, the medium and the fine grids, respectively. If no convergence is seen, a superfine global grid may be created and convergence check may be done between the medium, the fine and the superfine grids. However, such an operation will not be logical in terms of computational effort.

$$|\sigma^{M}_{max} - \sigma^{C}_{max}| > |\sigma^{M}_{max} - \sigma^{F}_{max}| \tag{3.3}$$

8. To check whether or not the peak stress has converged, a second convergence check given in Equation 3.4 may be used. $\epsilon_s = 0.01$ is considered as excellent accuracy, $\epsilon_s = 0.05$ as good, $\epsilon_s = 0.1$ as satisfactory and $\epsilon_s > 0.1$ as unsatisfactory [3]. If the ϵ_s value is in desired limits for the global models, there will be no need for a submodel and convergence is achieved. Otherwise, submodelling

is necessary to have convergence.

$$|\frac{\sigma^F_{max} - \sigma^M_{max}}{\sigma^F_{max}}| < \epsilon_s \tag{3.4}$$

9. First step of the submodelling technique is to determine the thickness of the submodel boundary. It is already proven that the maximum sought-after stress is not converged; however, points away from the location of that, it may converge. On a path starting from the location of maximum stress and perpendicular to the contact line, common nodes on coarse, medium and fine global models are selected. Stress convergence according to Equations 3.3 and 3.4 on these nodes are checked and the closest point to the maximum stress location satisfying both conditions are selected as the boundary of submodel. If no convergence is observed within the boundary layer, it is advised to increase the thickness of boundary layer for not to have any misleading stress values due to non-uniformity of mesh outside of the boundary layer.

10. Having determined the size of the submodel, three submodels are created as coarse submodel (CS), medium submodel (MS) and fine submodel (FS). Element size of the coarse submodel is the half size of the fine global model. Moreover, the medium and the fine submodels have the element size of half and one-fourth of the coarse submodel, respectively.

11. Boundary conditions that will be given to the submodels should be determined. From the finest global model, displacement values on the boundaries of the submodel is extracted. There are several reasons for the selection of displacements rather than stress. First reason is the errors of displacement decays faster compared to stress. For linear elements with element size of h, mean square of the error decreases at a rate of h for stress, whereas it is h^2 for displacements [30]. Secondly, it is a well known fact that the displacements are taken from nodes which is more accurate [3].

12. Post-processing codes are used to extract desired outputs from global model.

13. Interpolation on the nodal displacements extracted from the finest global model should be performed. In Figure 3.3, a hypothetical case of the use of submodelling technique is presented. Three grids of global model (C-M-F) and two

grids of submodel (CS-MS) are shown. It is assumed that there exist a peak stress on the upper left corner of the geometry. To converge that stress value, two submodels are created and the size of the submodel selected equals to a single element in fine global model. For this sample problem, only from three interior nodes of finest global model displacement values are extracted. Apart from the the shared 3 nodes with fine global model, there exist 2 extra nodes on coarse submodel and 6 extra nodes on medium submodel that requires boundary conditions to be given. Linear interpolation is conducted to determine interior nodal results. An interpolation code written in Matlab is used. Firstly, the code reads the output files of fine global model and it further interpolates those values. Then, it writes those nodal values in separate text files.

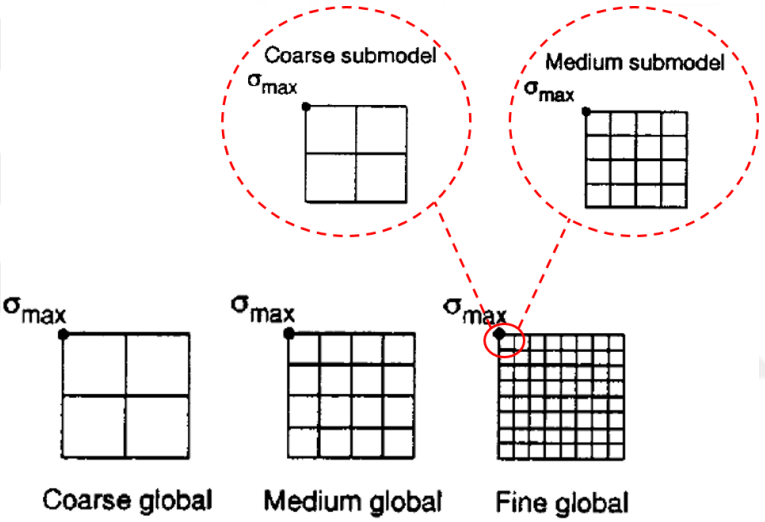


Figure 3.3: Example of submodel grids [9]

14. Having calculated the displacement values at each substep on the intervening nodes for three submodels, an ANSYS script written is used to apply nodal displacements to the boundary nodes of the submodels. Algorithm of this script is briefly explained as follows.

    (a) In the first part of the script, it reads the output files of interpolation code and stores them as arrays in ANSYS.

    (b) By using the arrays which have the coordinate values of the nodes after the interpolation, script determines the node numbers associated with those coordinates. It further stores the node numbers in arrays.

(c) Displacements are applied to the associated nodes for each sub-step and "ls file"s are created. A "ls file" is the file that ANSYS automatically creates for an ordinary analysis. Those files are sent to ANSYS solver. However, for this case, since the loading and boundary conditions are applied by using a script, those files should be created manually.

(d) After the creation of "ls file"s of for each sub-step, the files are sent to solver and the analysis is finished.

15. To determine the convergence of the submodel, discretization error should be calculated. It is defined as follows:

$$\epsilon_d = \left| \frac{\sigma_{max}^{FS} - \sigma_{max}^{MS}}{\sigma_{max}^{FS}} \right|, \tag{3.5}$$

where superscripts σ_{max}^{MS} and σ_{max}^{FS} are evaluated on medium and fine submodels by taking boundary conditions from fine global model.

16. If the error is in desired limits, peak stress evaluated with the fine submodel is considered to be converged. However, if it is not satisfied, then a finer coarse-medium-fine global model should be selected and submodelling procedure should be repeated for the new case.

3.3 Submodelling On A Simple Two Block Geometry

3.3.1 Geometry and Material Properties

Investigated geometry is given in Figure 2.1. 2D finite element analyses are carried out with plane stress assumption. Homalite® plexiglass is defined as the material used for upper and lower blocks. Material properties are provided in Table 3.1. The material is assumed to have isotropic and linear elastic behaviour.

Table 3.1: Material properties of Homalite® [8]

Elastic Modulus [GPa]	**Poisson's Ratio [-]**	**Density [kg/m^3]**
5.2	0.34	1230

3.3.2 Finite Element Model

3.3.2.1 Contact Properties

Frictional contact with a friction coefficient of 0.6 is defined between Homalite® bodies shown in Figure 3.4 [7]. The upper and the lower bodies are defined as contact and target bodies, respectively. For the contact enforcement method, the Normal Lagrange method is used. In Section 2.2.4, it is proven that the elastic slip tolerance has no effect on the peak stress value, so the program default value is set for the elastic slip tolerance factor. The reason for the selection of the Normal Lagrange algorithm is due to the convergence difficulties faced with the analyses conducted with the Pure Penalty and the Augmented Lagrange methods. As it is explained in Section 2.2.6, those methods allow some penetration between bodies. For the fine global model, analyses are not converged with the use of the Augmented Lagrange and the Pure Penalty methods as contact enforcement methods.

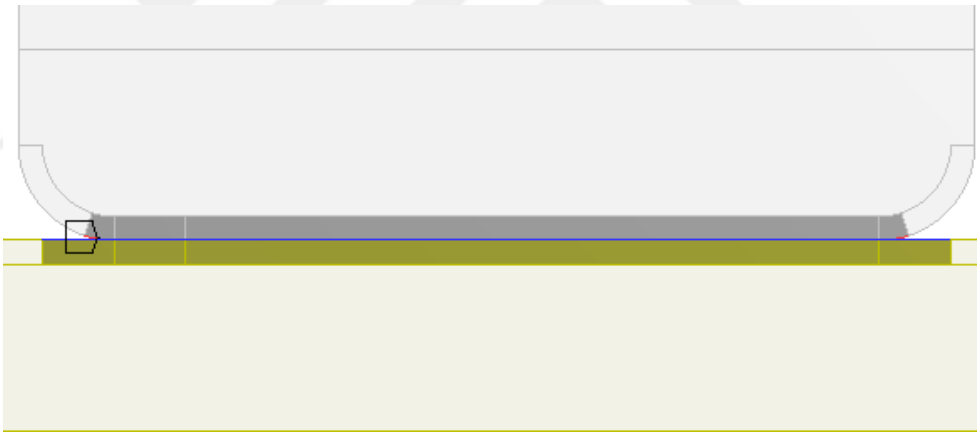


Figure 3.4: Contact surface between bodies

3.3.2.2 Meshing

To adjust the meshing properties, firstly the boundary layer should be defined. The local radius of curvature R for the model is 4 mm, so the boundary layer to be used is selected with a thickness of 1 mm. Boundary layer is highlighted with green color in Figure 3.5.

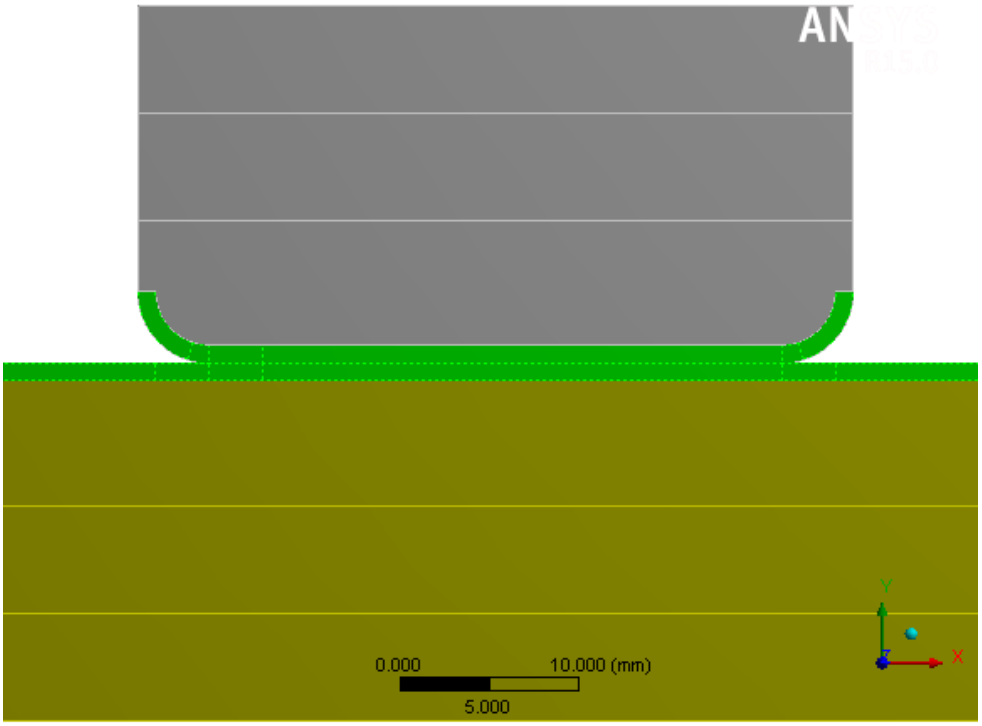


Figure 3.5: Boundary layer of two block model

To have systematic mesh couples (coarse, medium, fine) on the global model, edge sizing is defined to certain edges. These edges are highlighted in Figure 3.6. In Table 3.2, for the coarse, the medium and the fine global models, the edge sizing values are presented. It is seen that the edge sizing parameters regarding to the mesh of the boundary layer (boundary layer, R_1, R_2) are successively halved between the coarse and the medium global models and between the medium and the fine global models. The element sizing is directly given to the straight edges on the boundary layer. For the arc lengths within the boundary layer, line division is set according to the outer length of the arc. Given division is calculated by the ratio between the outer arc length and the element sizing given to the straight edges of the boundary layer. All surfaces regarding to the boundary layer is set to the mapped face meshing to have uniform mesh inside it. Outside of the boundary layer, the change is done in a systematic way. Each mesh parameter share a common ratio at the transition between meshes. There is no need for edges at the outside of the boundary layer to be successively halved, since its effect on the edge of contact stress is negligible. They are regarded as the transition elements.

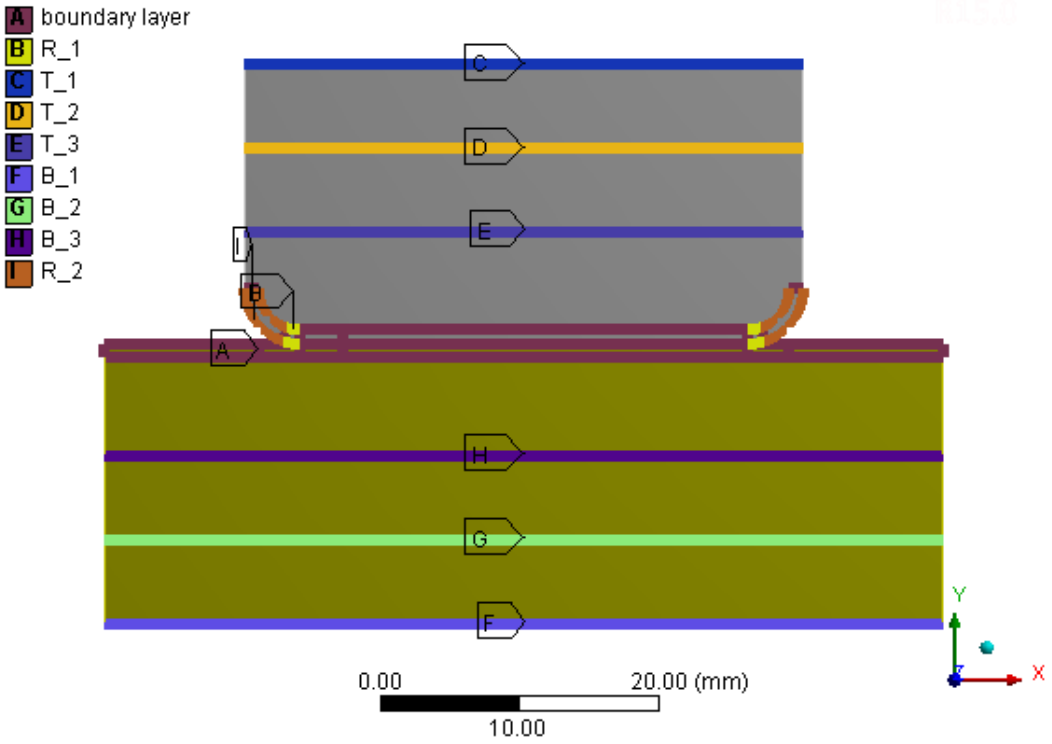


Figure 3.6: Edges that are defined with a sizing value to have systematic mesh

Table 3.2: Mesh parameters used for coarse, medium and fine global models

Edge Name	Coarse Mesh	Medium Mesh	Fine Mesh	Type of Sizing
boundary layer	0.5	0.25	0.125	element size [mm]
R_1	3	5	10	number of division
T_1	6	9	12	number of division
T_2	9	12	15	number of division
T_3	12	15	18	number of division
B_1	10	15	20	number of division
B_2	15	20	25	number of division
B_3	20	25	30	number of division
R_2	10	20	40	number of division

3.3.3 Loading and Boundary Conditions

Loading and boundary conditions of the model are discussed in Section 2.1.4. The only difference is that a displacement value of 0.8 mm is applied in +x direction on the nodes highlighted with yellow color (letter C) in Figure 2.3.

3.3.4 Submodels

In Figure 2.4, it is seen that for the sample problem peak contact stress occurs at the bottom left corner of the upper block, so the submodel will be selected in the neighbourhood of that location. For this purpose, global model results of the peak stress should be analysed. If the convergence is achieved with the global model, there will be no need for the submodelling. In Table 3.12, it is seen that the convergence of the edge of peak stress is not observed on the global models. Error value is way beyond the desired limits. The submodelling is necessary to converge the edge of peak stress.

Table 3.3: Maximum equivalent stress for coarse, medium, fine global models and their convergence checks

Stress Component	**Coarse Mesh [MPa]**	**Medium Mesh [MPa]**	**Fine Mesh [MPa]**
σ_{eqv}	91.86	120.21	135.59
Convergence Check According to Equation 3.3		**Error Value ϵ According to Equation 3.4**	
Satisfied		0.11	

Initially the size of the submodel should be determined. Following the 9th step of the submodelling procedure explained in Section 3.2, at the 0.5mm thickness the convergence of the equivalent stress reaches to the desired limits. Accordingly, the submodel shown in Figure 3.7 is created. Only mesh parameters on the submodel are boundary layer size and R_1. Values set for those are given in Table 3.13.

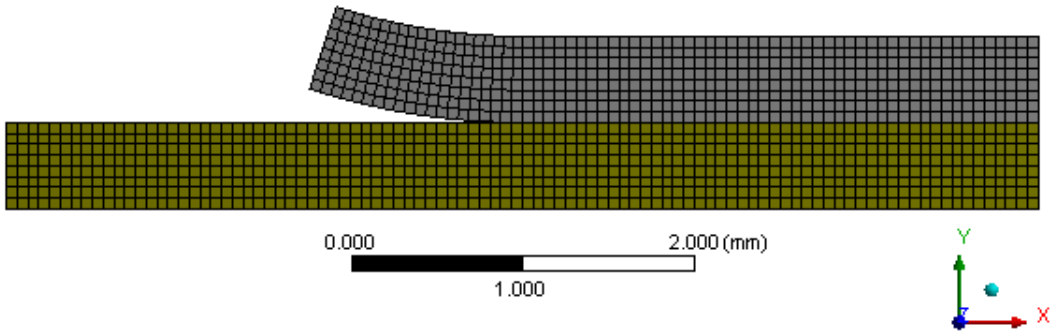


Figure 3.7: Coarse submodel

Table 3.4: Mesh parameters used for coarse, medium and fine submodels

Edge Name	Coarse Submodel	Medium Submodel	Fine Submodel	Type of Sizing
boundary layer	0.0625	0.03125	0.015625	element size [mm]
R_1	20	40	80	number of division

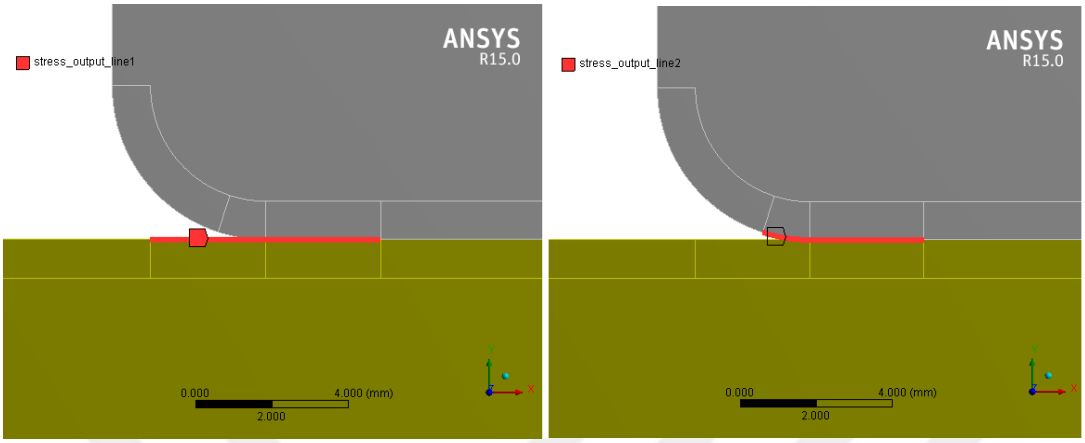
3.3.5 Results

Because of the loading and the boundary conditions applied, high local edge of contact stresses occur at the neighbourhood of bottom left corner of the upper part and its counterpart on the lower block. The contact is in "sliding" condition at the end of the loading step. Figure 2.4 shows the location of the peak contact stress for the medium global model. To visualize the convergence of the peak stresses, two paths are defined on the lower and the upper blocks as shown with red color in Figure 3.8. Identical paths are also defined on submodels to have consistence results.

In Tables 3.5 and 3.6, the maximum peak stress values on bottom and top bodies are presented, respectively. Hence, the error values defined in Equations 3.4 and 3.5 are calculated for each stress component. They are calculated between the medium and the fine meshes of each global and submodel results. By individually comparing each stress component with the global model and the submodel results, it is seen that after the implementation of the submodelling approach, the stress results are converged in desired limits. In Figures 3.9 - 3.14, the peak stress results on the defined path is visualized. Convergence of the peak stresses with submodelling can be observed in the zoomed views on peak locations.

Table 3.5: Maximum normal and shear stresses at the edge of contact on bottom body for both global and submodels with their errors

Models	Peak Stress Components	Coarse [MPa]	Medium [MPa]	Fine [MPa]	Error, ϵ [-]
Global	$\sigma_{x,max}$	151.94	202.13	239.59	0.16
	$\sigma_{y,max}$	109.46	123.55	128.66	0.04
	$\tau_{xy,max}$	40.47	53.79	62.23	0.136
Submodel	$\sigma_{x,max}$	249.85	249.70	249.88	0.0007
	$\sigma_{y,max}$	131.45	132.33	132.25	0.0005
	$\tau_{xy,max}$	69.33	74.07	76.97	0.038



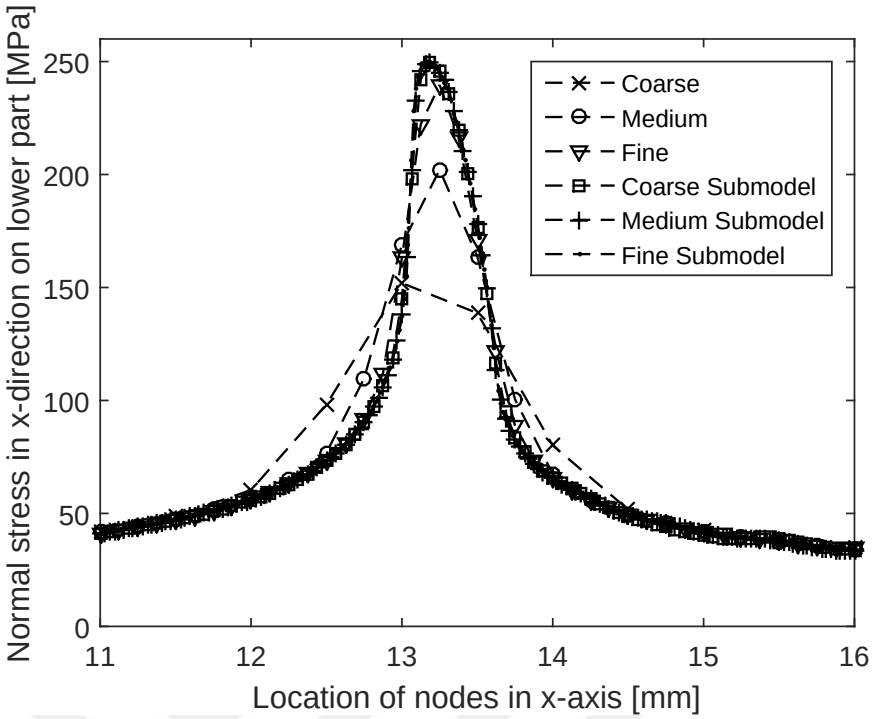
(a) On lower part

(b) On upper part

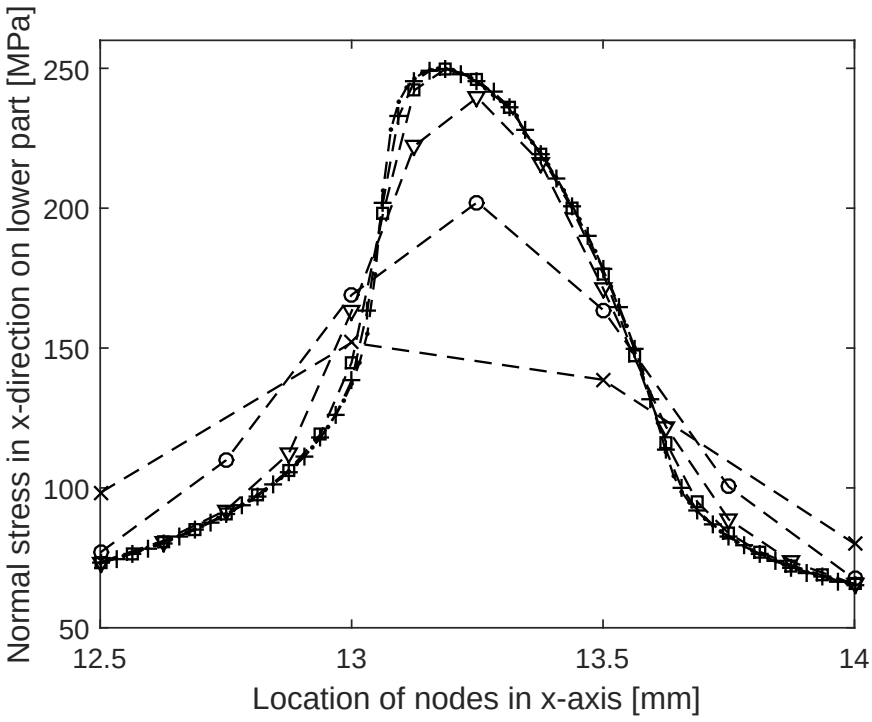
Figure 3.8: The paths defined for the stress output (shown in red)

Table 3.6: Maximum normal and shear stresses at the edge of contact on top body for both global and submodels with their errors

Models	**Peak Stress Components**	**Coarse [MPa]**	**Medium [MPa]**	**Fine [MPa]**	**Error, ϵ [-]**
Global	$\sigma_{x,max}$	93.69	118.30	127.90	0.075
	$\sigma_{y,max}$	106.77	136.40	130.84	0.04
	$\tau_{xy,max}$	43.14	56.99	63.50	0.10
Submodel	$\sigma_{x,max}$	135.70	139.28	141.38	0.015
	$\sigma_{y,max}$	131.84	132.31	131.94	0.0028
	$\tau_{xy,max}$	69.29	72.55	74.85	0.031

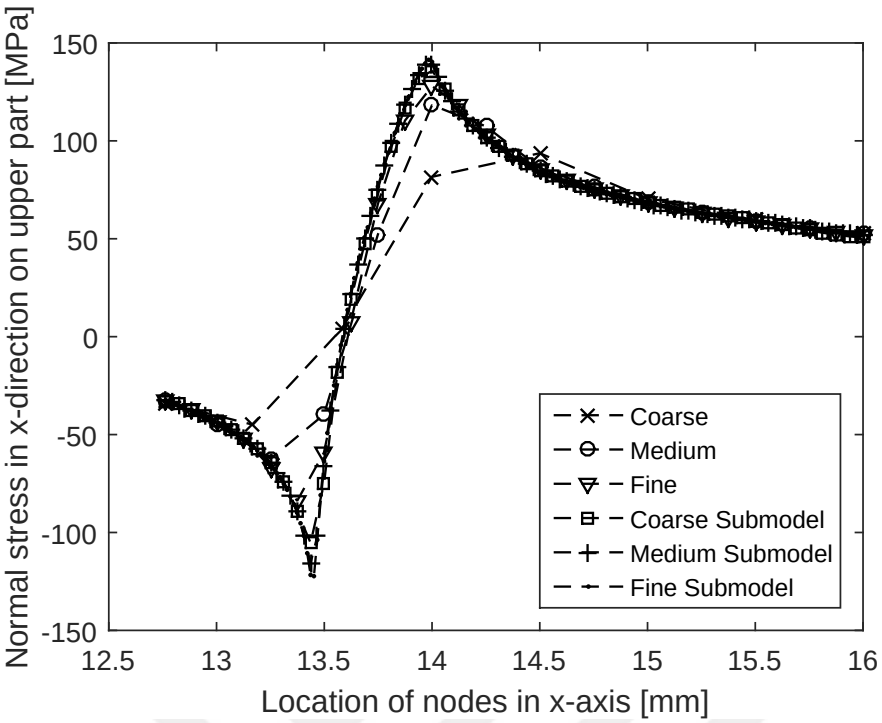


(a) General view

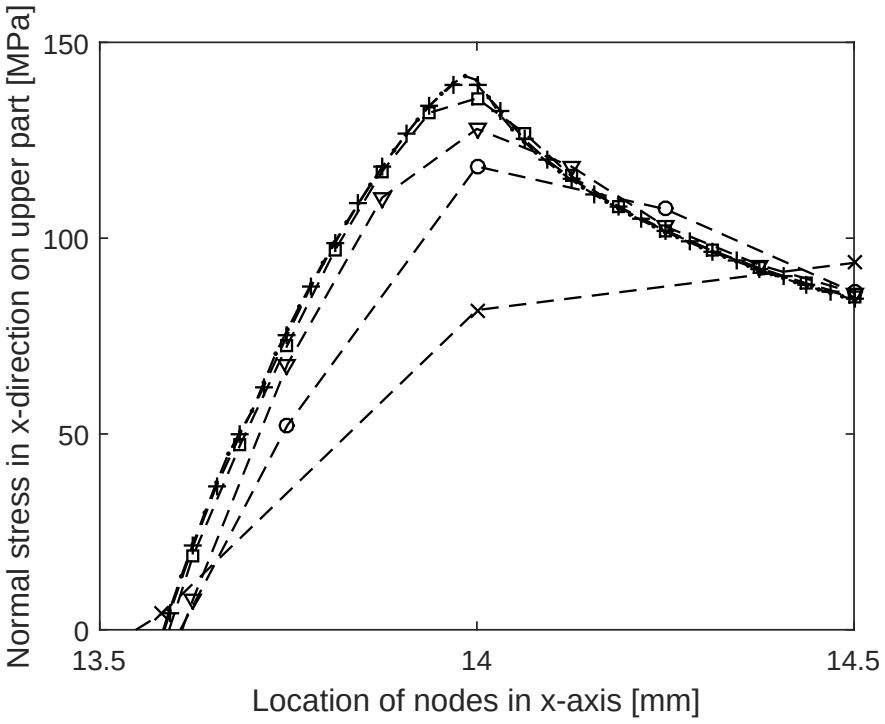


(b) Zoomed view on the peak location

Figure 3.9: Normal stress in x-direction σ_x on lower part for three global and three submodels on the defined path

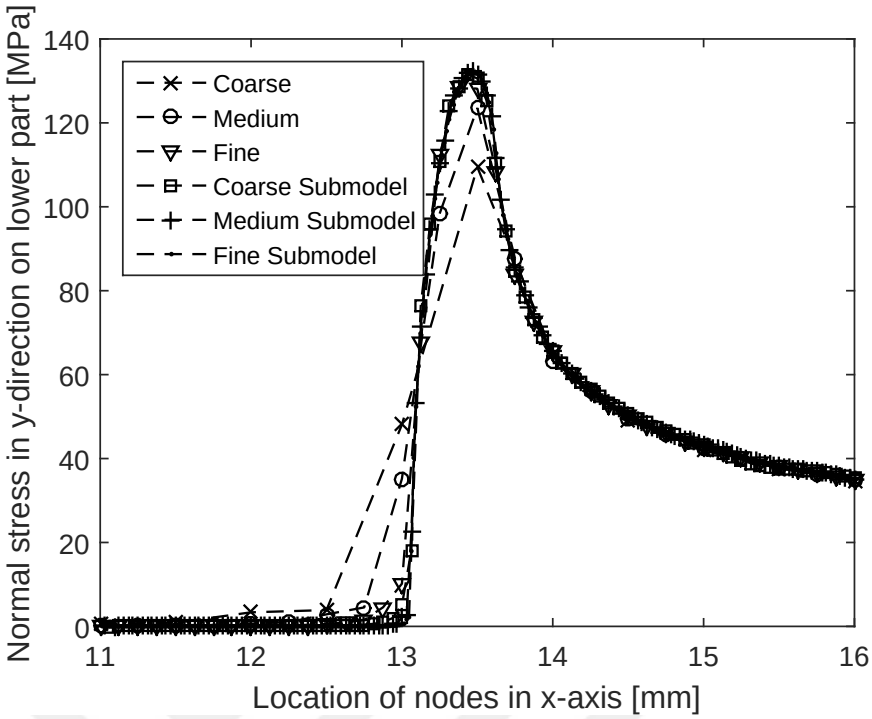


(a) General view

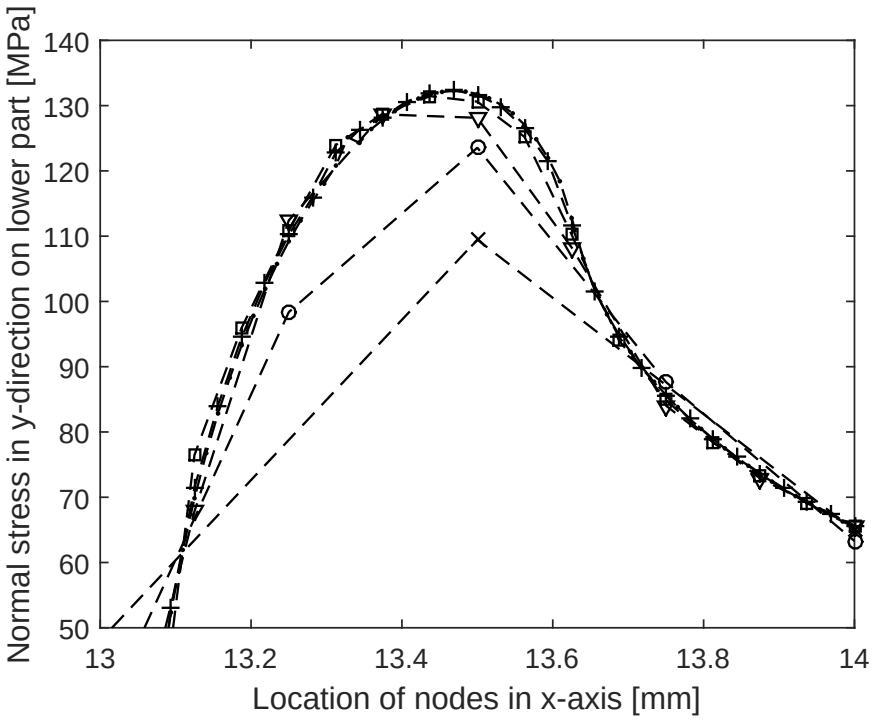


(b) Zoomed view on the peak location

Figure 3.10: Normal stress in x-direction σ_x on upper part for three global and three submodels on the defined path

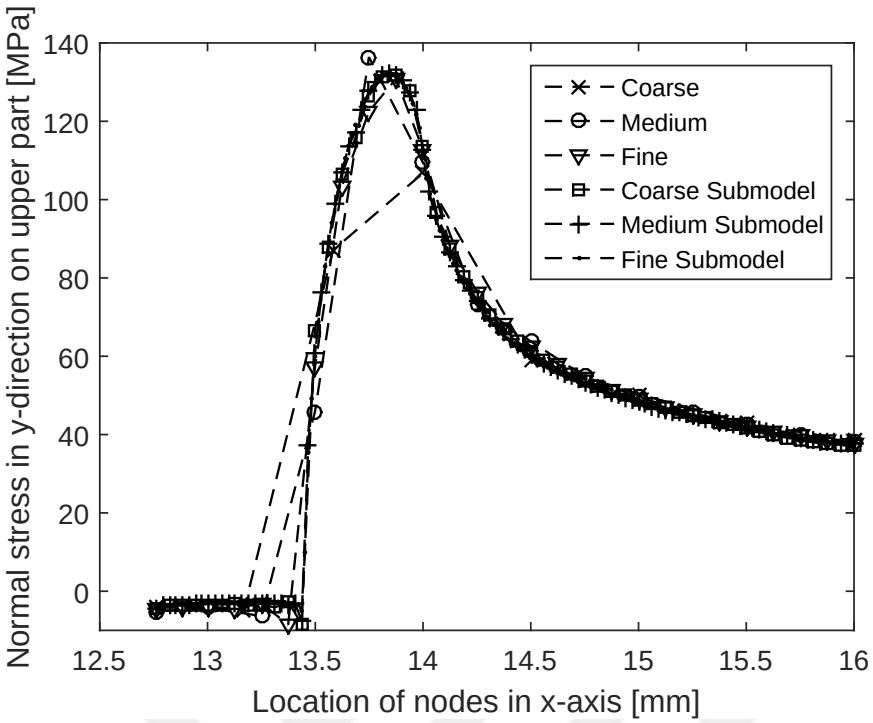


(a) General view

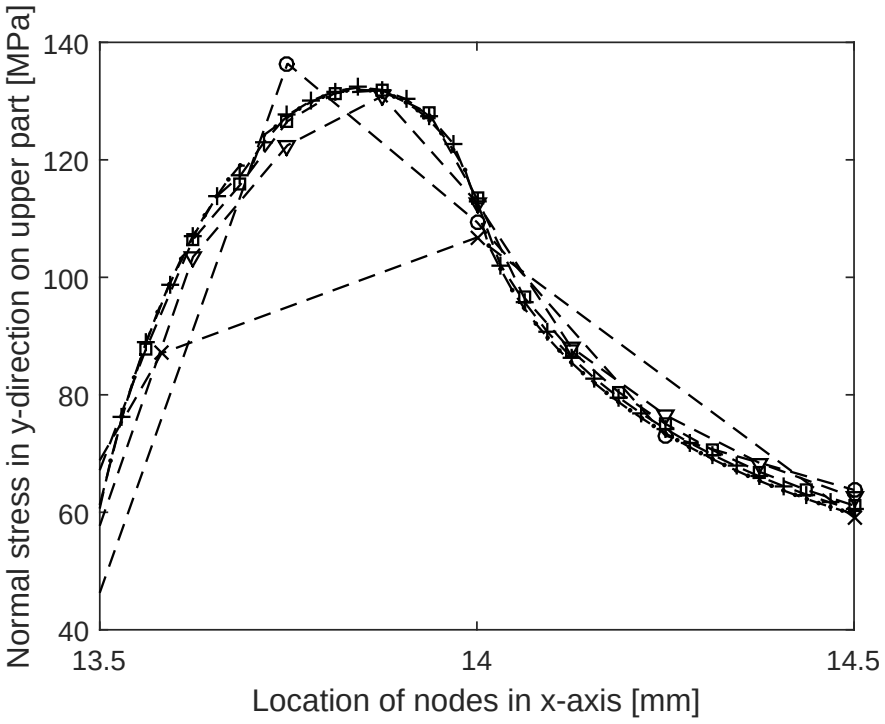


(b) Zoomed view on the peak location

Figure 3.11: Normal stress in y-direction σ_y on lower part for three global and three submodels on the defined path

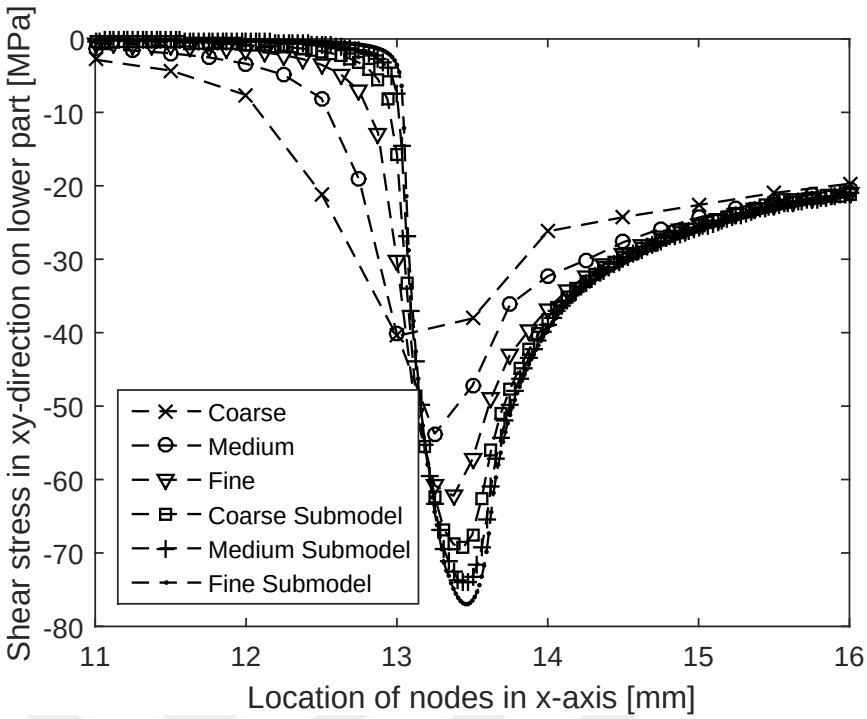


(a) General view

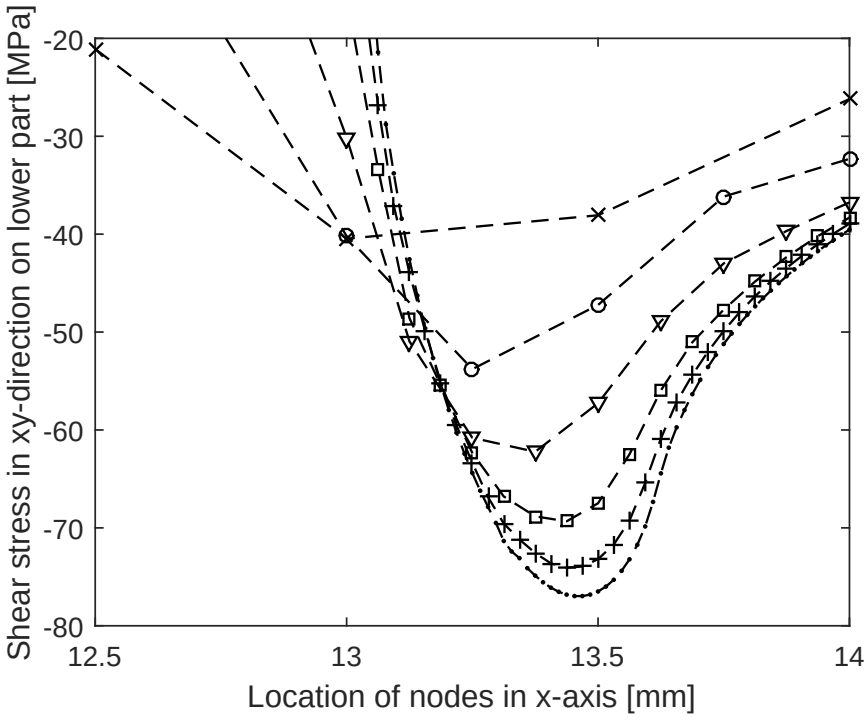


(b) Zoomed view on the peak location

Figure 3.12: Normal stress in y-direction σ_y on upper part for three global and three submodels on the defined path

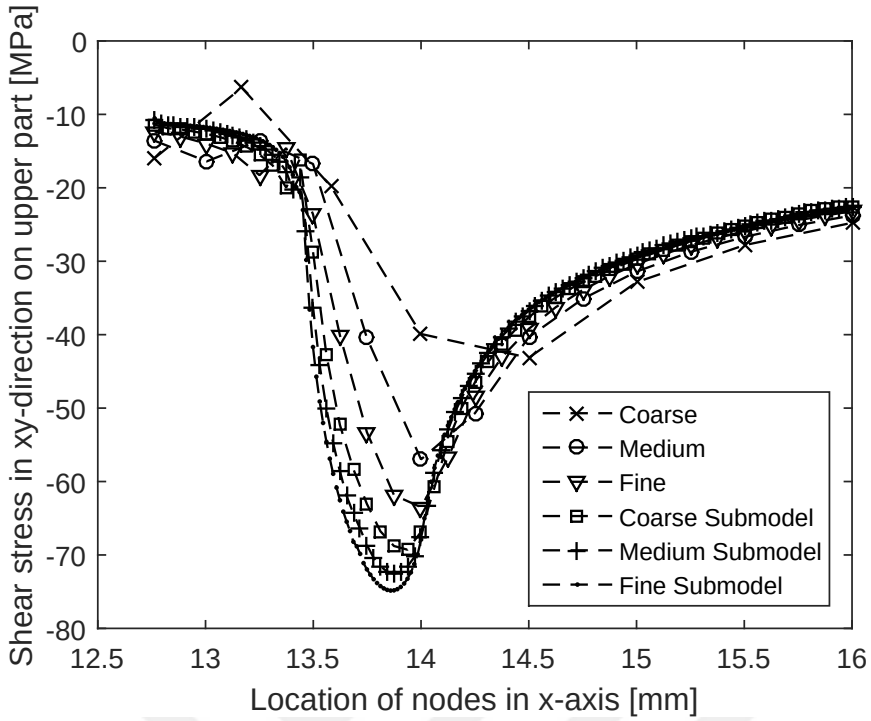


(a) General view

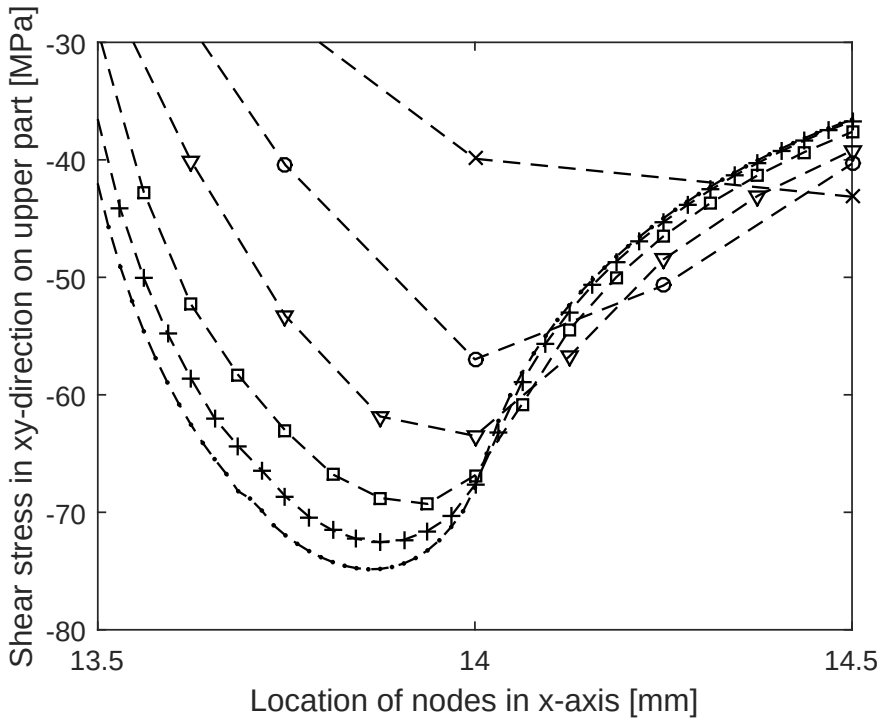


(b) Zoomed view on the peak location

Figure 3.13: Shear stress in xy-direction τ_{xy} on lower part for three global and three submodels on the defined path



(a) General view



(b) Zoomed view on the peak location

Figure 3.14: Shear stress in xy-direction τ_{xy} on upper part for three global and three submodels on the defined path

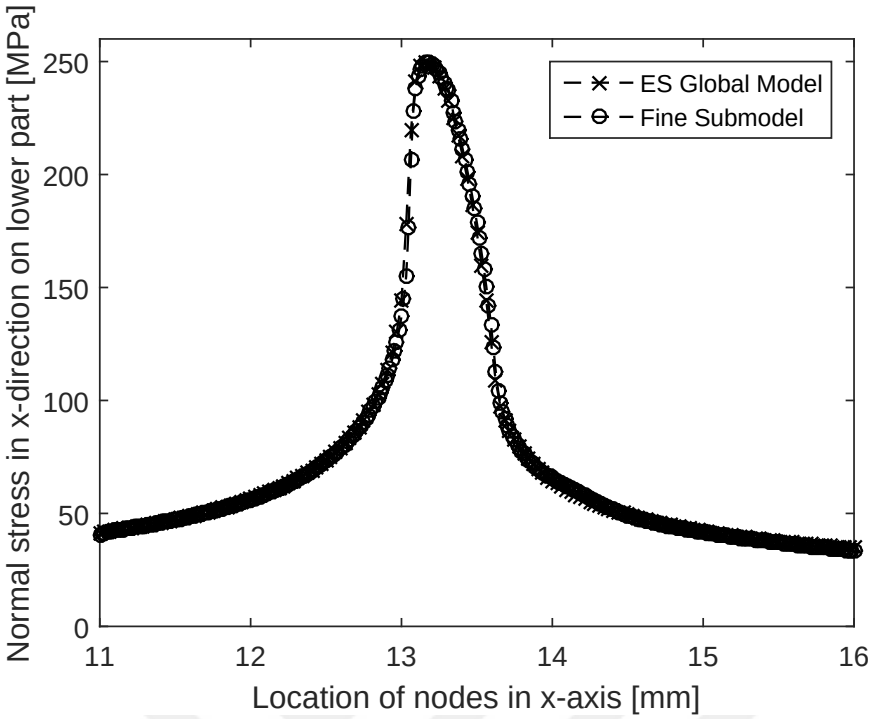
Furthermore, in order to compare the accuracy of the submodel, two more global models are created with smaller mesh sizes compared to fine global model. These models are called as the superfine (S) and the extra-superfine (ES) global models. Meshing parameters used to create these two finer models are given in Table 3.7. In Figure 3.6, edge names given in the Table 3.7 are highlighted. This approach is not logical computational-wise; however, it is possible to ensure the correctness of the submodelling approach and the simple model selected here can be meshed finer without the requirement of high computational resources. The results of these models are presented in Figure 3.15. It is seen that two lines of the different models are almost on top of each other. Solution times of the global models and the submodels are presented in Table 3.8. It is observed that the fine submodel has the accuracy close to the extra-superfine global model with a four-five times quicker solution time.

Table 3.7: Mesh parameters used for superfine (S) and extra-superfine (ES) global models

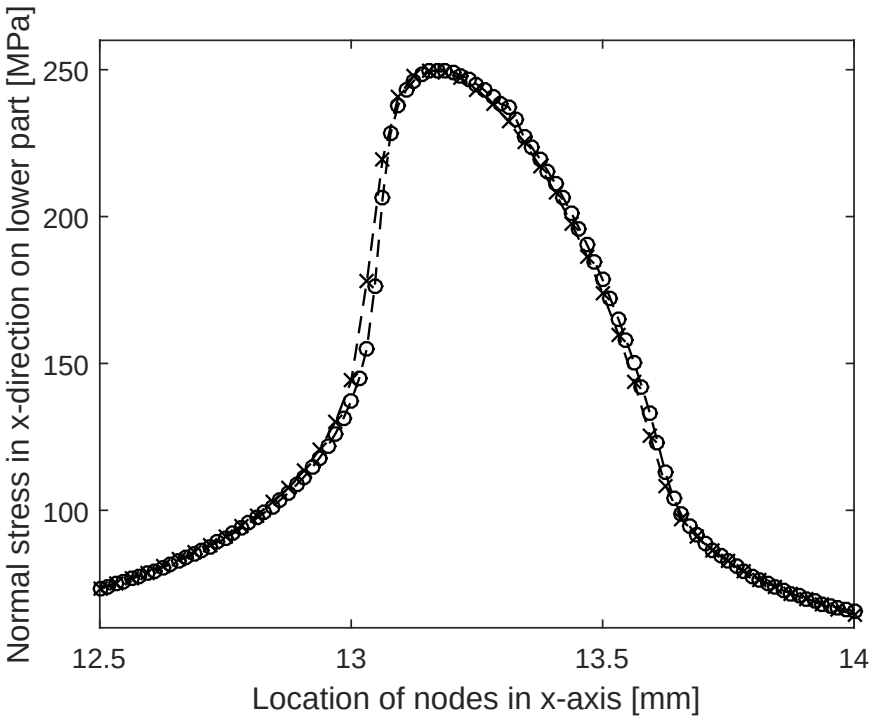
Edge Name	**Superfine Mesh (S)**	**Extra-superfine Mesh (ES)**	**Type of Sizing**
boundary layer	0.0625	0.03125	element size [mm]
R_1	20	40	number of division
T_1	15	18	number of division
T_2	18	21	number of division
T_3	21	24	number of division
B_1	25	30	number of division
B_2	30	35	number of division
B_3	35	40	number of division
R_2	80	160	number of division

Table 3.8: Solution times of the global models and the submodels

	Solution Time [s]				
Models	**Coarse**	**Medium**	**Fine**	**Superfine**	**Extra-superfine**
Global Model	19.9	50.0	145.0	425.4	1431.0
Submodel	23.6	84.2	305.9	N/A	N/A



(a) General view



(b) Zoomed view on the peak location

Figure 3.15: Normal stress in x-direction σ_x on lower part for extra-superfine global model and fine submodel on the defined path

3.4 Submodelling On Dovetail Geometry

3.4.1 Geometry

The geometric model used in [22] is used for the two dimensional submodelling study on the dovetail joint. Geometric details and dimensions of the blade and the disc geometries are given in Figure 3.16. Investigated geometry is a single part of the cyclic sector of rotor. Due to the symmetry condition, investigation of one section is sufficient.

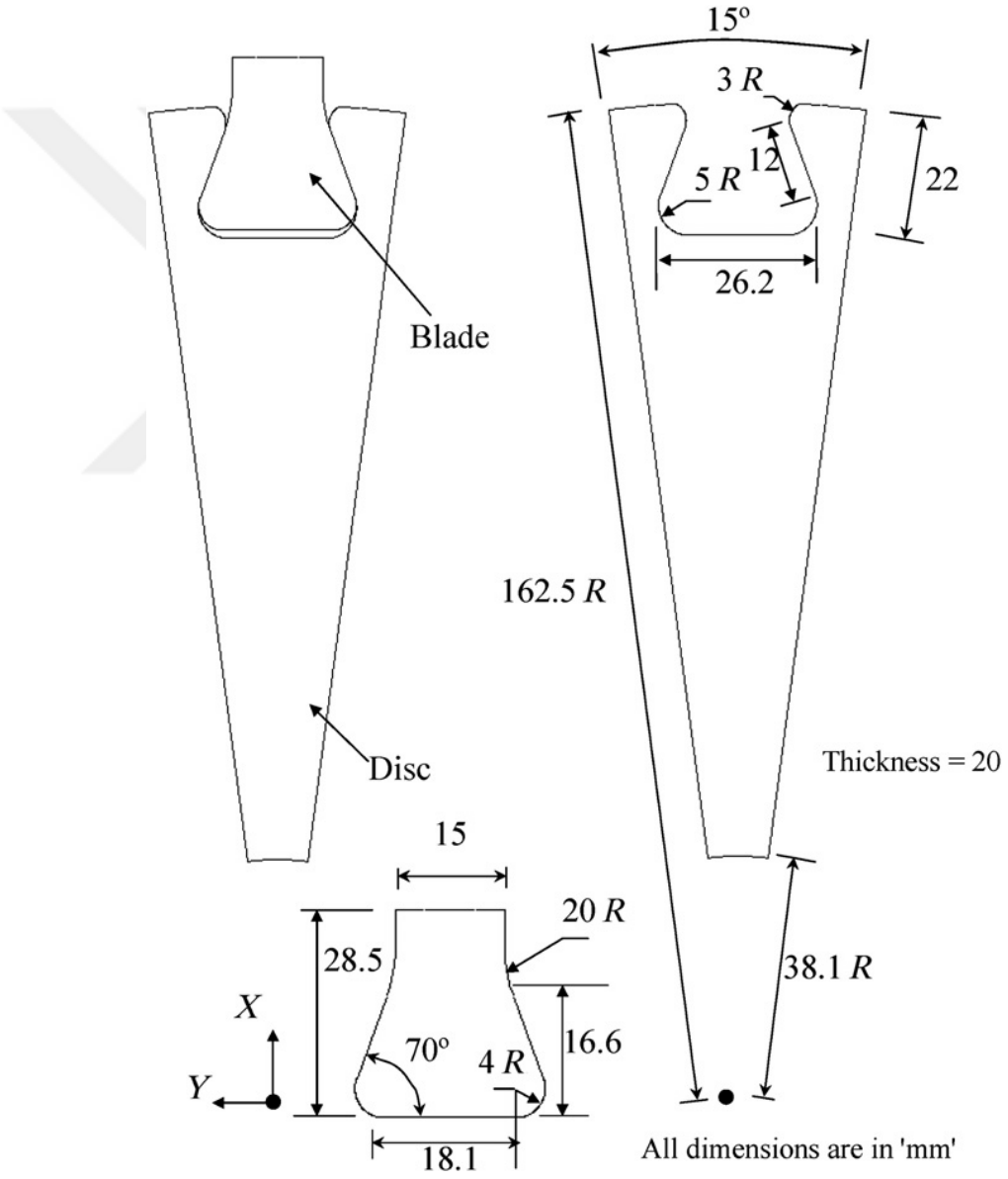


Figure 3.16: Geometric details of dovetail joint [22]

3.4.2 Material Properties

Material properties of the Ti-alloy aero-engine are provided in Table 3.9. Material is assumed to have isotropic and linear elastic behaviour.

Table 3.9: Material properties of aero-engine [1]

Elastic Modulus [GPa]	**Poisson's Ratio [-]**	**Density [kg/m^3]**
110	0.30	4500

3.4.3 Finite Element Model

Due to the symmetry of the geometry given in Figure 3.16 and the loading given in Section 3.4.4, modelling of the half section is done. Model used in the analyses is shown in Figure 3.17.

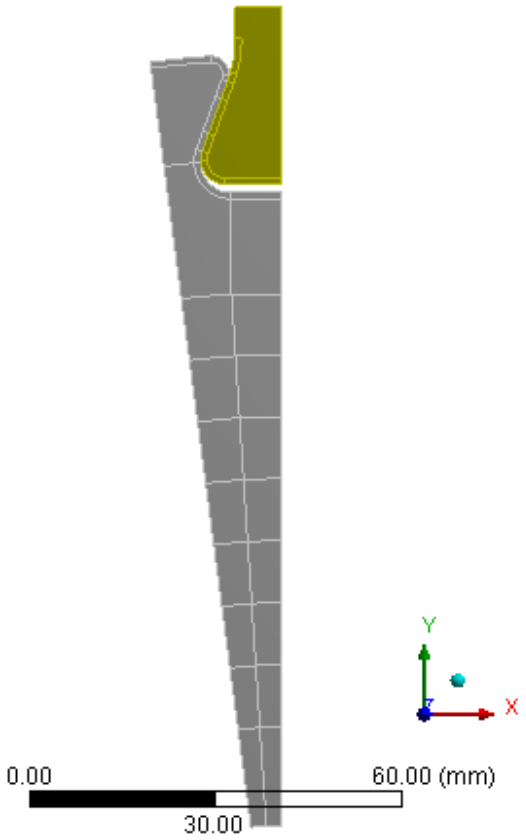


Figure 3.17: 2D finite element model of the dovetail joint

2D finite element analyses are carried out with plane stress assumption (PLANE182 elements in ANSYS) on both the global models and the submodels of the dovetail. In 3.18, equivalent stress at the location of the peak stresses on the path shown in Figure 3.28a for 2D and 3D finite element models are presented. For 3D model, stresses are extracted from three different paths defined in the thickness direction at locations of z=0 mm (mid-section), z=5 mm and z=10 mm (free surface). It is seen that the 2D model slightly over-estimates the stress values compared to 3D model. It is concluded that 2D modelling of the dovetail would be convenient for the problem considered.

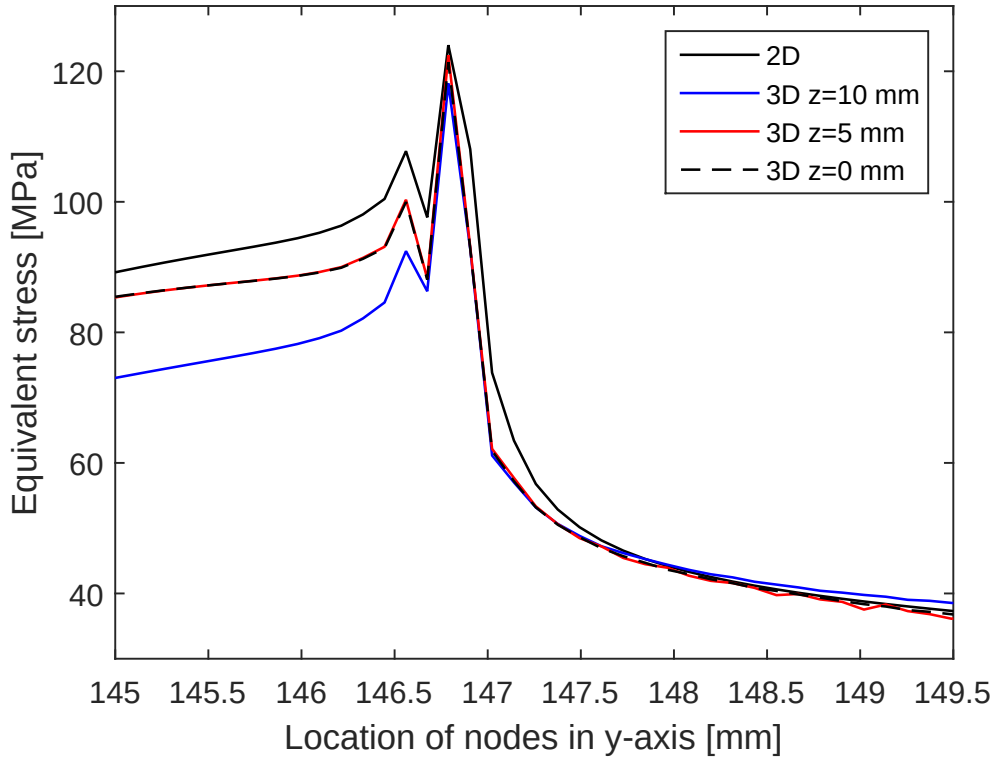


Figure 3.18: Equivalent stress on the peak stress location for 2D and 3D finite element analyses of dovetail

3.4.3.1 Contact Properties

Frictional contact with a friction coefficient of 0.3 is defined between the bodies shown in Figure 3.19 [1]. 3-node line-to-line contact is defined between contacting bodies. The disc and the blade bodies are defined as the target and the contact bodies, respectively. ANSYS TARGE169 and CONTA172 elements are used for the

modelling of the target and the contact surfaces, respectively. For the contact enforcement method, the Normal Lagrange method is used. In Section 2.2.4, it has proven that the elastic slip tolerance has no effect on the peak stress value, so the program default value is set for the elastic slip tolerance factor. The reason for the selection of the Normal Lagrange algorithm is due to the convergence difficulties faced with the analyses conducted with the Pure Penalty and the Augmented Lagrange methods. As it is explained in Section 2.2.6, those methods allow some penetration between bodies. For this model, for the fine global model it is seen that the convergence have not achieved with the use of the Augmented Lagrange and the Pure Penalty methods.

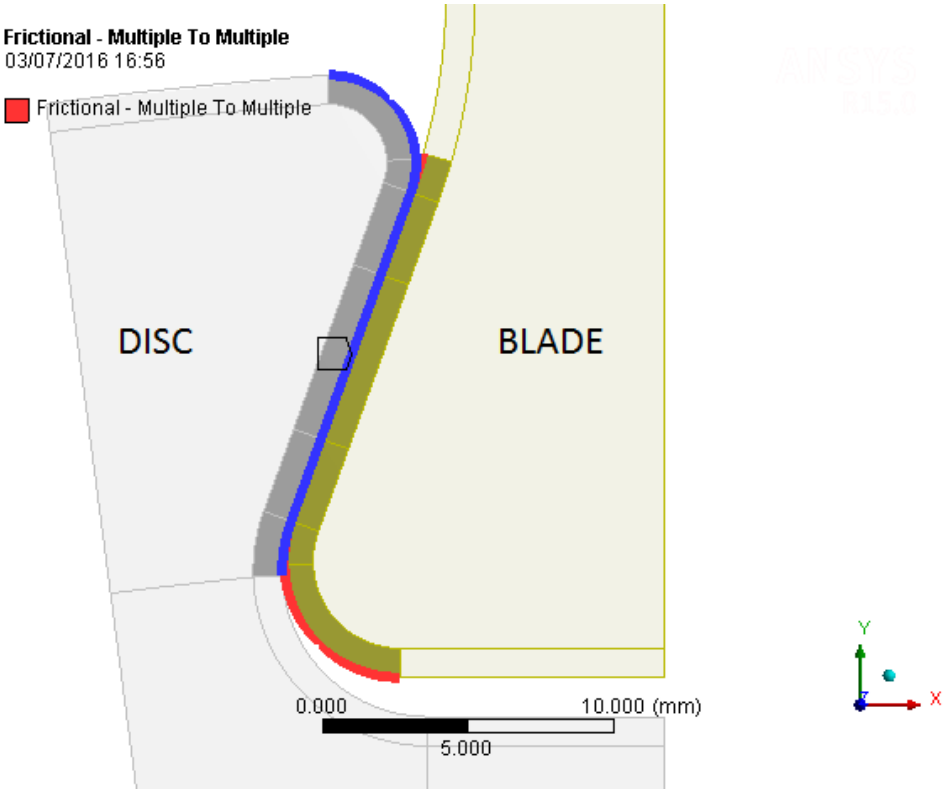


Figure 3.19: Contact surface between bodies

3.4.3.2 Meshing

To adjust the meshing properties, firstly the boundary layer should be defined. The smaller local radius of curvature R for this model is 3 mm, so the thickness of the boundary layer thickness to be used should have a value around 0.75. For meshing purposes, it is selected as 1 mm. Boundary layer is highlighted with green color in

Figure 3.20.

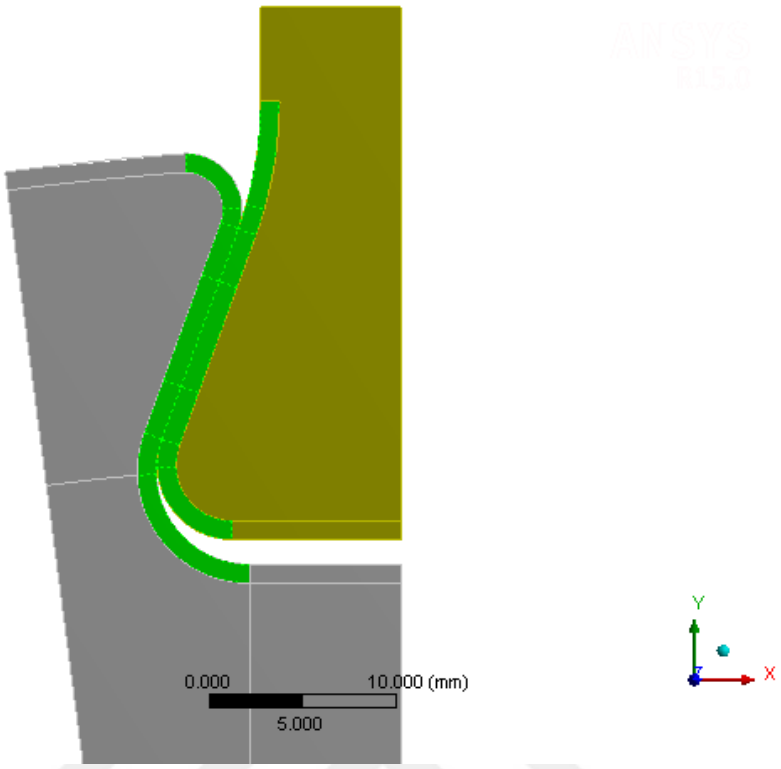
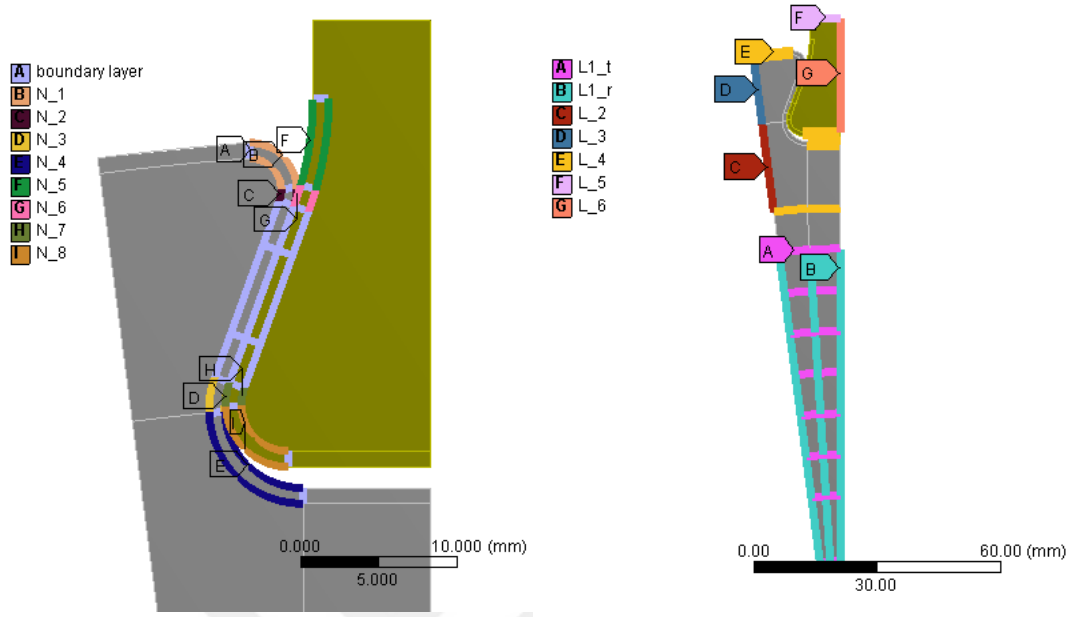


Figure 3.20: Boundary layer of dovetail model

To have systematic mesh couples (coarse, medium, fine) on global model, edge sizing is defined to certain edges. These edges are highlighted in Figure 3.21. In Tables 3.11 and 3.10, for the coarse, the medium and the fine global models, the meshing parameters are presented. It is seen that the edge sizing parameters regarding to the mesh of boundary layer (Table 3.11) are successively halved between the coarse and the medium global models and between the medium and the fine global models. The element sizing is given to the straight edges of the boundary layer. For the arc lengths within the boundary layer, line division is set according to the outer length of the arc. Given division is calculated by the ratio between outer arc length and element sizing given to the straight edges of the boundary layer. All surfaces regarding to the boundary layer is set to mapped face meshing to have uniform mesh inside it. Outside of the boundary layer, to the edges highlighted in Figure 3.21b, edge divisions are given with the values shown in Table 3.10. The change is done in a systematic way. Each mesh parameter share a common ratio at the transition between meshes. There is no need for edges at the outside of the boundary layer to be successively halved,

since its effect on the edge of contact stress is negligible. They are regarded as the transition elements.



(a) Inside of the boundary layer

(b) Outside of the boundary layer

Figure 3.21: Edges that are defined with a sizing value to have a systematic mesh

Table 3.10: Mesh parameters used outside of the boundary layer for coarse, medium and fine global models

Edge Name	**Coarse Mesh**	**Medium Mesh**	**Fine Mesh**	**Type of Sizing**
L1_t	1	2	3	number of division
L1_r	1	2	3	number of division
L_2	2	4	8	number of division
L_3	6	12	24	number of division
L_4	3	6	12	number of division
L_5	3	6	12	number of division
L_6	12	24	36	number of division

Table 3.11: Mesh parameters used inside of the boundary layer for coarse, medium and fine global models

Edge Name	Coarse Mesh	Medium Mesh	Fine Mesh	Type of Sizing
boundary layer	0.125	0.0625	0.03125	element size [mm]
N_1	36	72	144	number of division
N_2	8	16	32	number of division
N_3	16	32	64	number of division
N_4	64	128	256	number of division
N_5	40	80	160	number of division
N_6	10	20	40	number of division
N_7	12	24	48	number of division
N_8	48	96	192	number of division

3.4.4 Loading and Boundary Conditions

A cylindrical coordinate system is defined to the center of the circular disc part of the dovetail joint. Loading and boundary conditions of the finite element model are shown in Figure 3.22. Due to the symmetry condition of the model, displacements of the nodes on the edges highlighted with orange color (letter A) are constraint in θ-direction. Hence, in order to prevent the rigid body motion, displacements of the nodes on the edges highlighted with red color (letter C) are constraint in r-direction. Analyses are carried out in one load step with 10 sub-steps. An angular velocity of 1050 rad/s is applied at the center of circular disc as shown with purple color in Figure 3.22 [1]. The blade is subjected to the angular velocity. Due to the angular velocity, a steady and regular centrifugal force is acting at center of gravity of the blade.

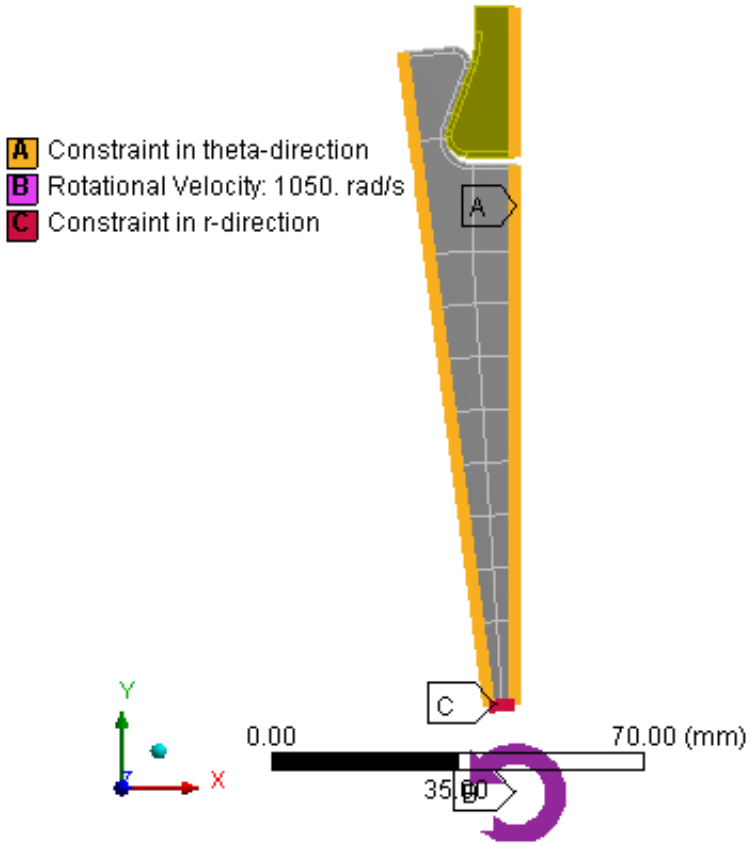


Figure 3.22: Loadings and boundary conditions for the finite element model

3.4.5 Submodels

In Figure 3.23, it is seen that for the dovetail geometry with the applied loading, the maximum equivalent stress occurs at the bottom edge of the contact, so the submodel will be selected in the neighbourhood of that location. For this purpose, the global model results of the peak stress should be analysed. If the convergence is achieved with the global models, there will be no need for the submodelling technique. In Table 3.12, it is seen that the convergence of the edge of peak stress is not observed on the global models. Error value is way beyond the desired limits. Submodelling is necessary to converge the edge of peak stress.

In order to show the convergence behaviour of the peak stress, a superfine model is created. Convergence check according to Equation 3.3 is done between the medium (M), the fine (F) and the superfine (SF) global models in Equation 3.6. The equation verifies the convergence behaviour of the maximum edge of contact stress for this

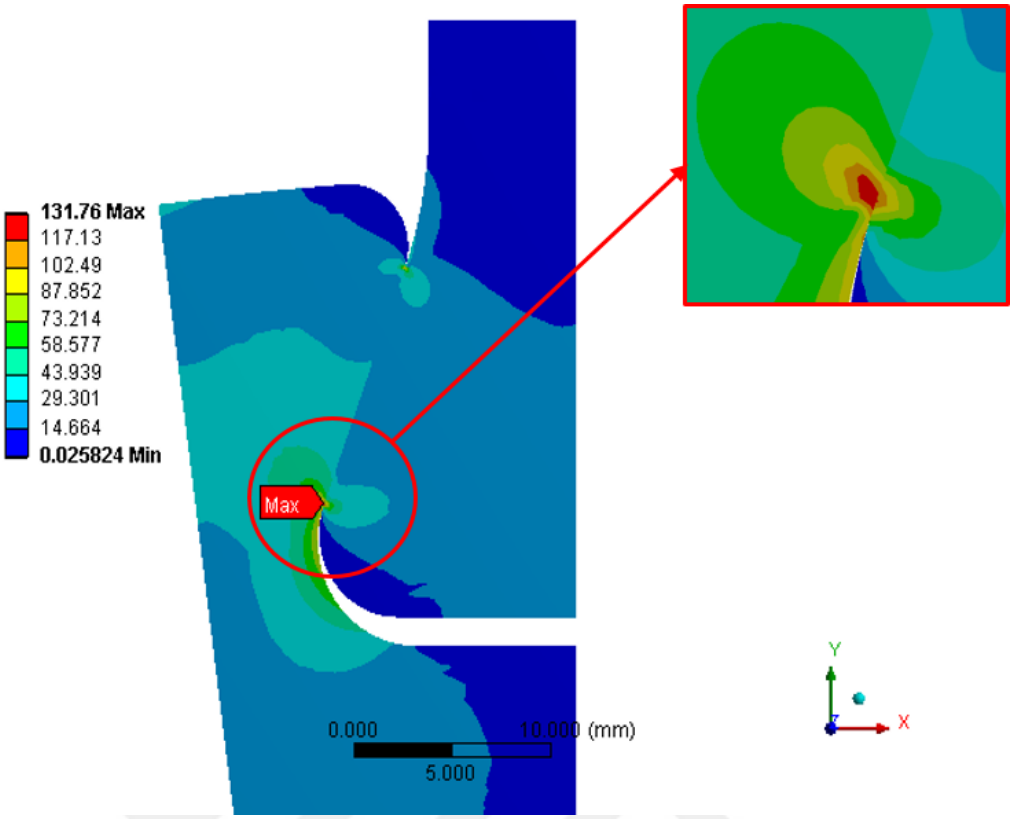


Figure 3.23: Equivalent stress distribution of 2D dovetail model with coarse mesh

Table 3.12: Maximum equivalent stress for coarse, medium, fine global models and their convergence checks

Stress Component	**Coarse Mesh [MPa]**	**Medium Mesh [MPa]**	**Fine Mesh [MPa]**
σ_{eqv}	131.76	169	209.19
Convergence Check According to Equation 3.3		**Error Value ϵ According to Equation 3.4**	
Not satisfied		0.19	

model.

$$
\begin{aligned}
|\sigma^{F}_{max} - \sigma^{M}_{max}| &> |\sigma^{F}_{max} - \sigma^{SF}_{max}| \\
|209.19 - 169| &> |209.19 - 228.71| \\
30.19 &> 19.52
\end{aligned}
\tag{3.6}
$$

Initially the size of the submodel should be determined. Following the 9th step of the submodelling procedure explained in Section 3.2, at the 0.25mm thickness the convergence of the equivalent stress has seen in the desired limits. Accordingly, the submodel shown in Figure 3.24 is created. Mesh parameters used on the submodel are boundary layer size, N_3 and N_4. Values set for those are given in Table 3.13.

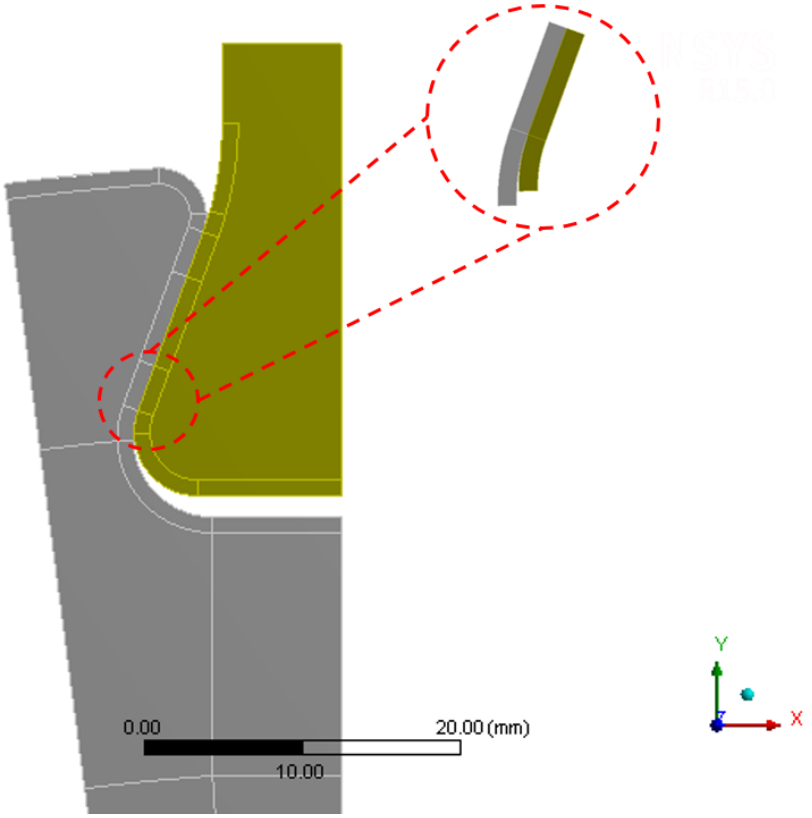


Figure 3.24: Submodel

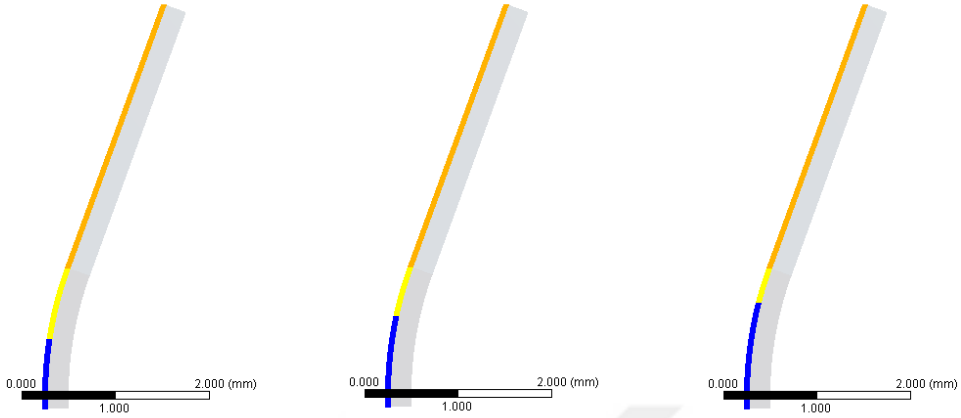
Table 3.13: Mesh parameters used for coarse, medium and fine submodels

Edge Name	**Coarse Submodel**	**Medium Submodel**	**Fine Submodel**	**Type of Sizing**
boundary layer	0.015625	0.0078125	0.00390625	element size [mm]
N_3	128	256	512	number of division
N_7	96	192	384	number of division

3.4.6 Results

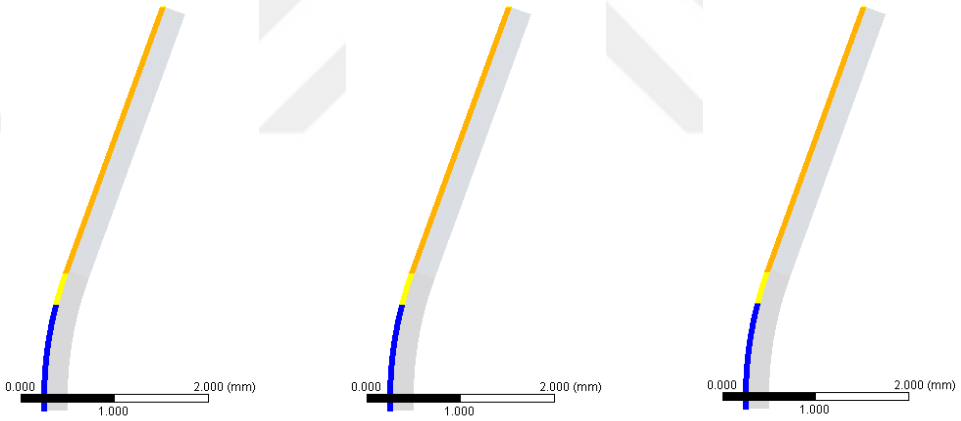
The condition of the contact is given in Figures 3.25, 3.26 and 3.27 for the stages corresponding to 0.1 times, 0.5 times and 1 times of the maximum loading, respectively.

It is seen that contact is in sliding condition as soon as the loading is presented to the system. In the figures, orange color designates the "sliding" condition of the contact, yellow and blue colors are the conditions for "near contact" and "far contact.



(a) Coarse Submodel (b) Medium Submodel (c) Fine Submodel

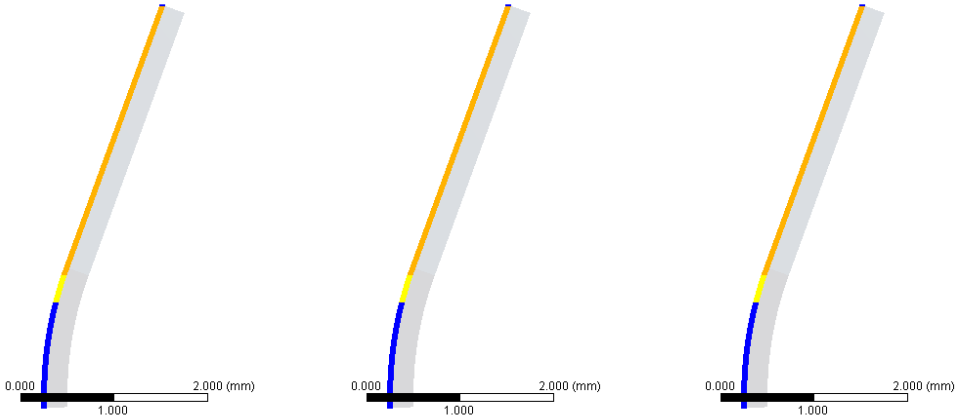
Figure 3.25: Condition of the contact at the stage of 0.1 times of the maximum loading



(a) Coarse Submodel (b) Medium Submodel (c) Fine Submodel

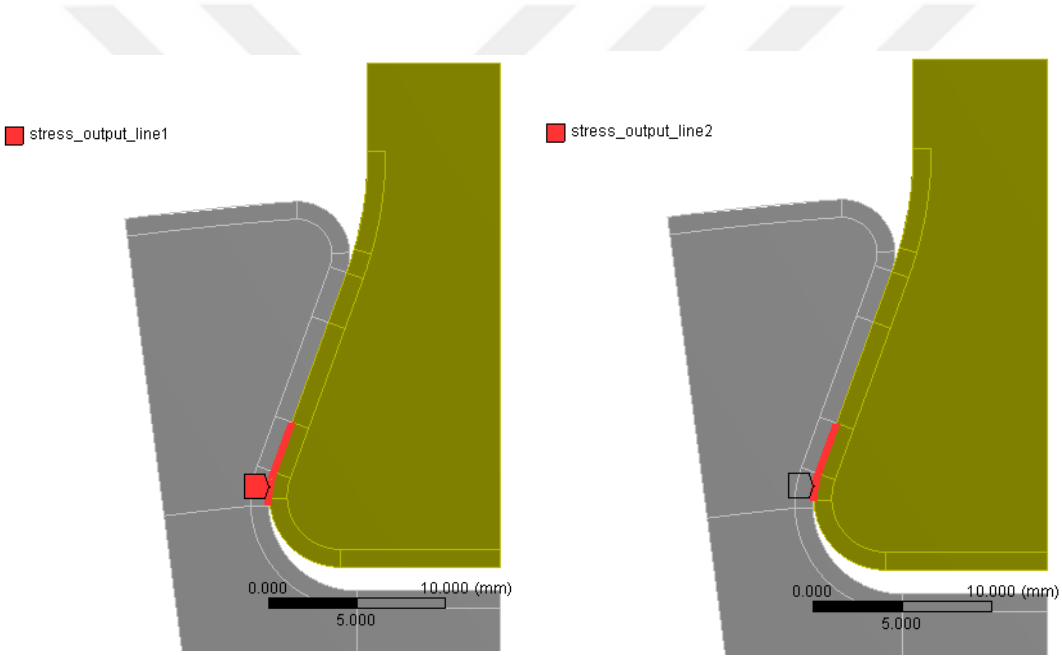
Figure 3.26: Condition of the contact at the stage of 0.5 times of the maximum loading

Because of the loading and the boundary conditions applied, high local edge of contact stresses occur at the neighbourhood of bottom contact area. Figure 3.23 shows the location of the peak contact stress for the coarse global model. To visualize the convergence of the peak stresses, two paths are defined on the lower and the upper blocks as shown with red color in Figure 3.28. Identical paths are also defined on submodels to have consistence results.



(a) Coarse Submodel (b) Medium Submodel (c) Fine Submodel

Figure 3.27: Condition of the contact at the maximum loading



(a) On the disc (b) On the blade

Figure 3.28: The paths defined for the stress output (shown in red)

A coordinate system is defined on bodies as shown in Figure 3.29. Stress results are presented according to the defined coordinate system. On the coordinate system, x and y directions defined as parallel and perpendicular to the contact line, respectively. In Tables 3.14 and 3.15, the maximum peak stress values on the disc and the blade are presented, respectively. Hence, the error values defined in Equations 3.4 and 3.5 are calculated for each stress component. They are calculated between the medium and

the fine meshes of each global and submodel results. By individually comparing each stress component with the global model and the submodel results, it is seen that after the implementation of the submodelling approach, the stress results are converged in desired limits. The error in the global stiffness of the system calculated between the medium and the fine global models is around 1.2 percent, whereas from the table the difference in the peak stress is at least 10 percent for the global models. Therefore, the global models could be satisfactory for the global response of the system while the submodelling is needed for the accurate computation of stress values in stress concentration zones.

In Figures 3.30 - 3.35, the peak stress results on the defined path is visualized. Convergence of the peak stresses with submodelling can be observed in the zoomed views on peak locations.

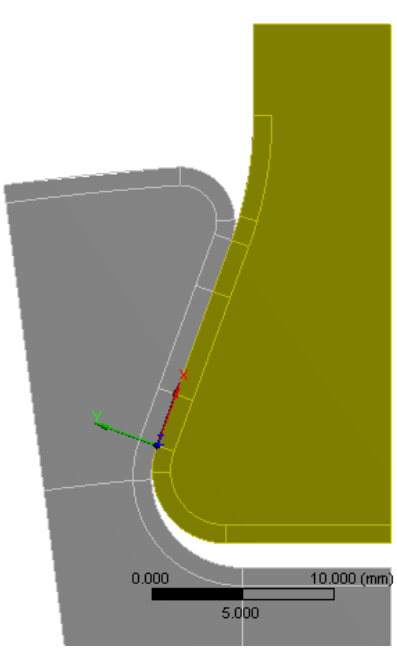


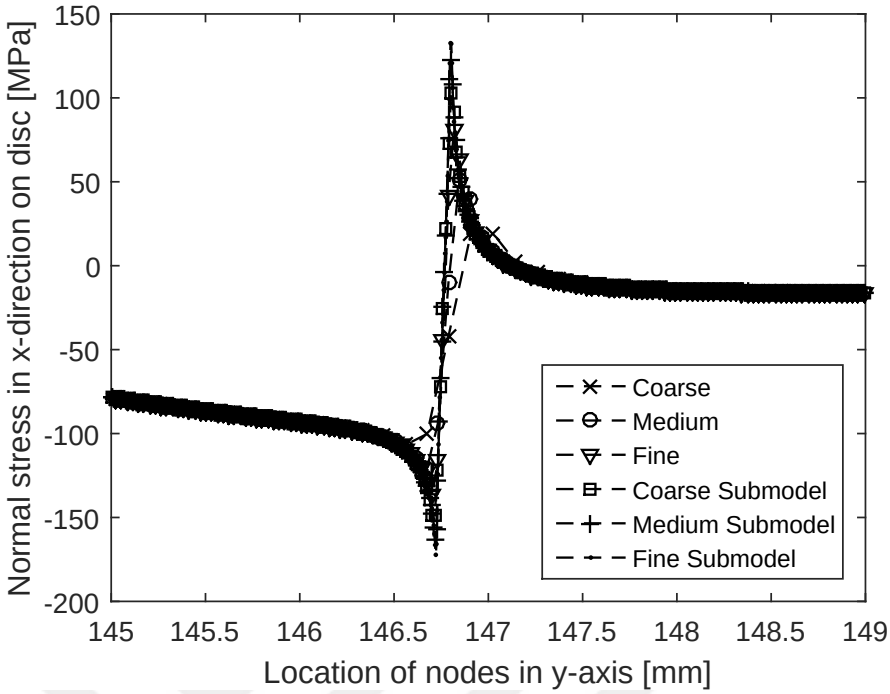
Figure 3.29: Coordinate system defined for stress outputs

Table 3.14: Maximum normal and shear stresses at the edge of contact on the disc for both global and submodels with their errors

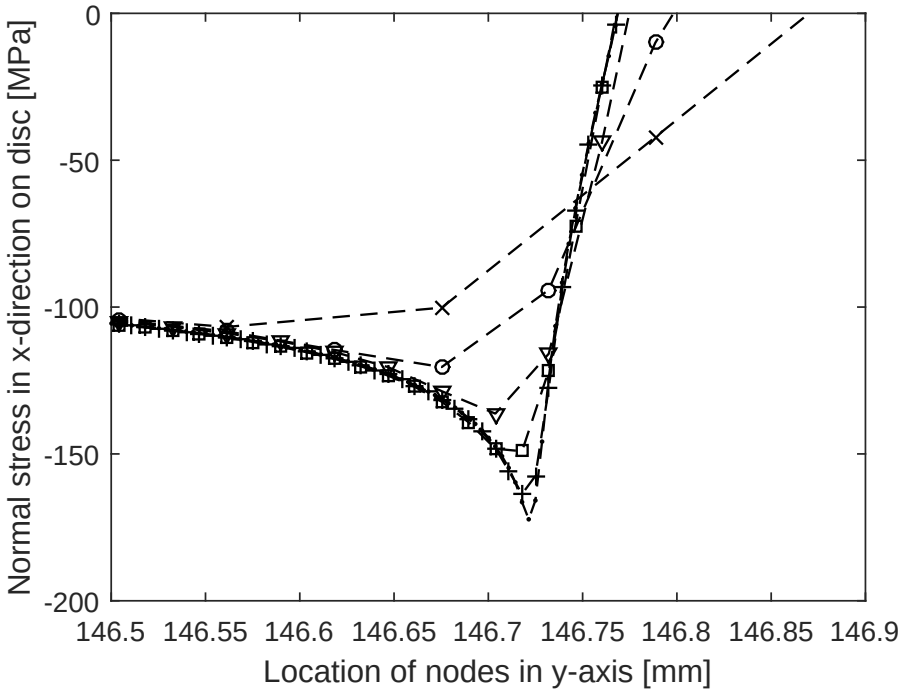
Models	**Peak Stress Components**	**Coarse [MPa]**	**Medium [MPa]**	**Fine [MPa]**	**Error, ϵ [-]**
Global	$\sigma_{x,max}$	106.77	120.42	136.28	0.12
	$\sigma_{y,max}$	109.64	151.47	179.71	0.16
	$\tau_{xy,max}$	30.34	34.54	45.91	0.25
Submodel	$\sigma_{x,max}$	149.08	163.65	172.25	0.05
	$\sigma_{y,max}$	202.76	223.90	224.67	0.0034
	$\tau_{xy,max}$	53.67	61.37	63.66	0.036

Table 3.15: Maximum normal and shear stresses at the edge of contact on the blade for both global and submodels with their errors

Models	**Peak Stress Components**	**Coarse [MPa]**	**Medium [MPa]**	**Fine [MPa]**	**Error, ϵ [-]**
Global	$\sigma_{x,max}$	108.62	151.43	201.06	0.25
	$\sigma_{y,max}$	103.93	150.25	174.74	0.14
	$\tau_{xy,max}$	31.76	41.72	49.58	0.15
Submodel	$\sigma_{x,max}$	228.39	246.57	252.73	0.024
	$\sigma_{y,max}$	211.82	224.89	225.13	0.001
	$\tau_{xy,max}$	56.40	61.64	64.79	0.049

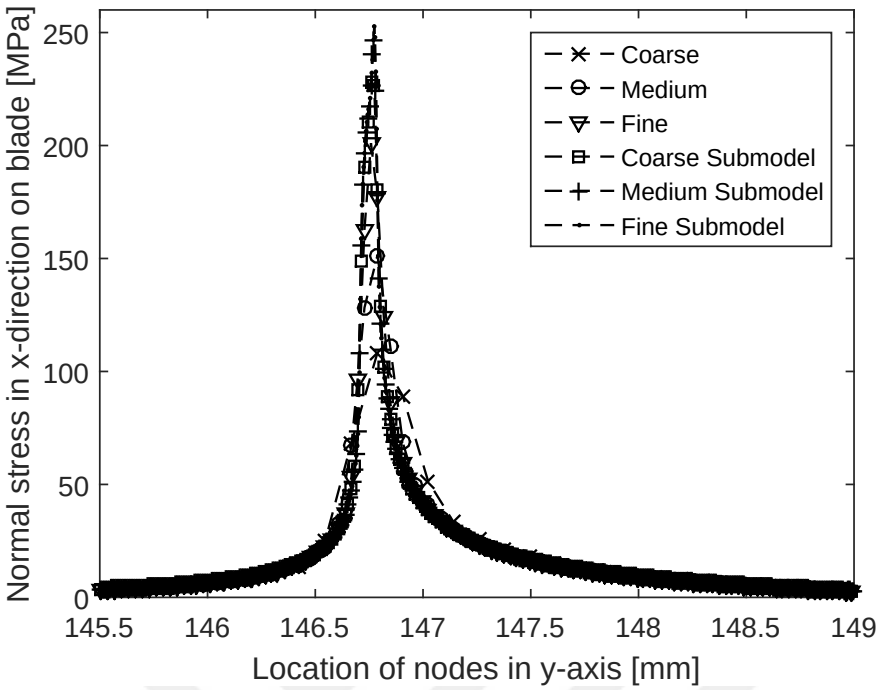


(a) General view

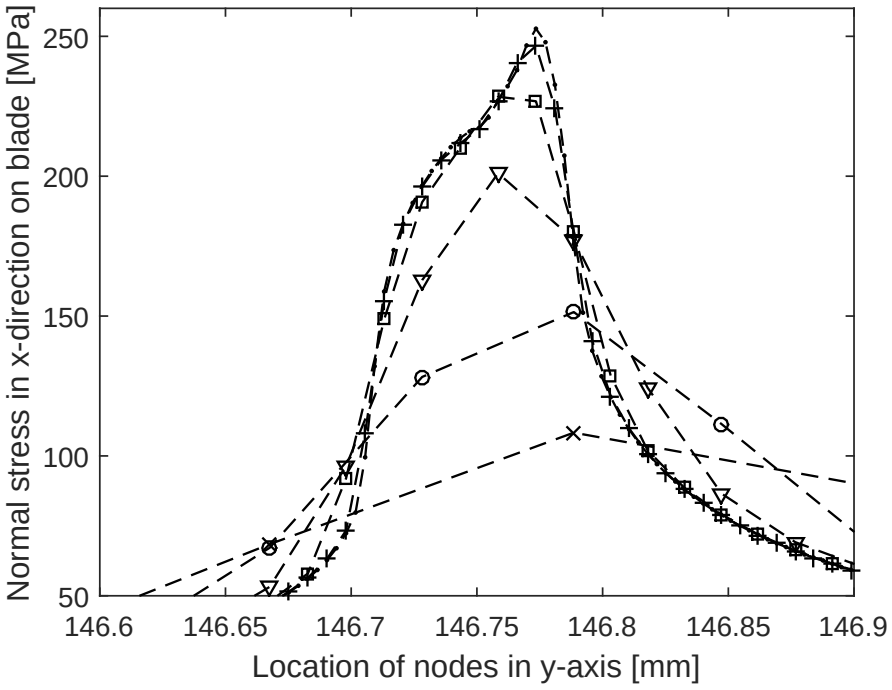


(b) Zoomed view on the peak location

Figure 3.30: Normal stress in x-direction σ_x on the disc for three global and three submodels on the defined path

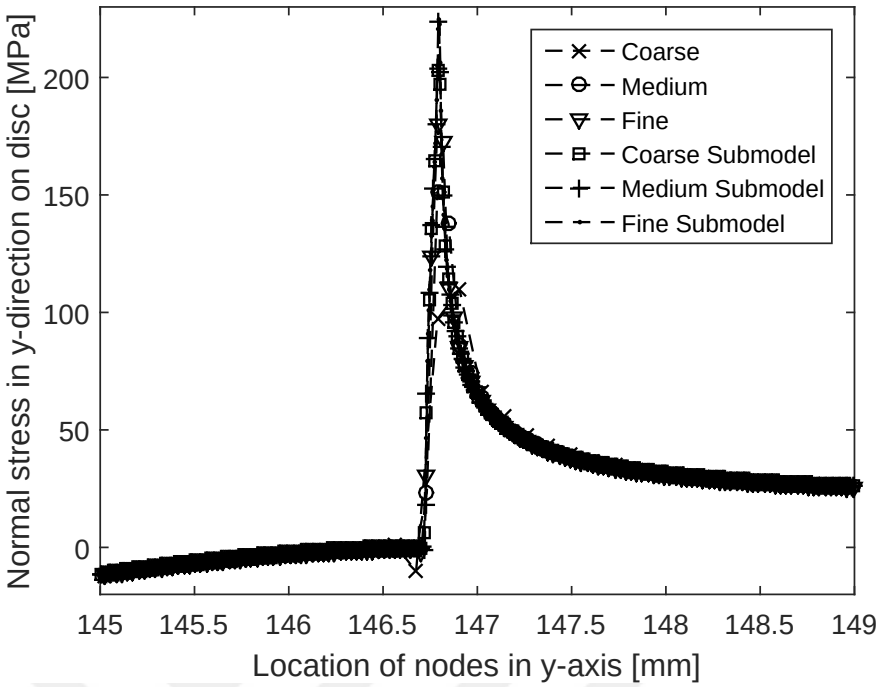


(a) General view

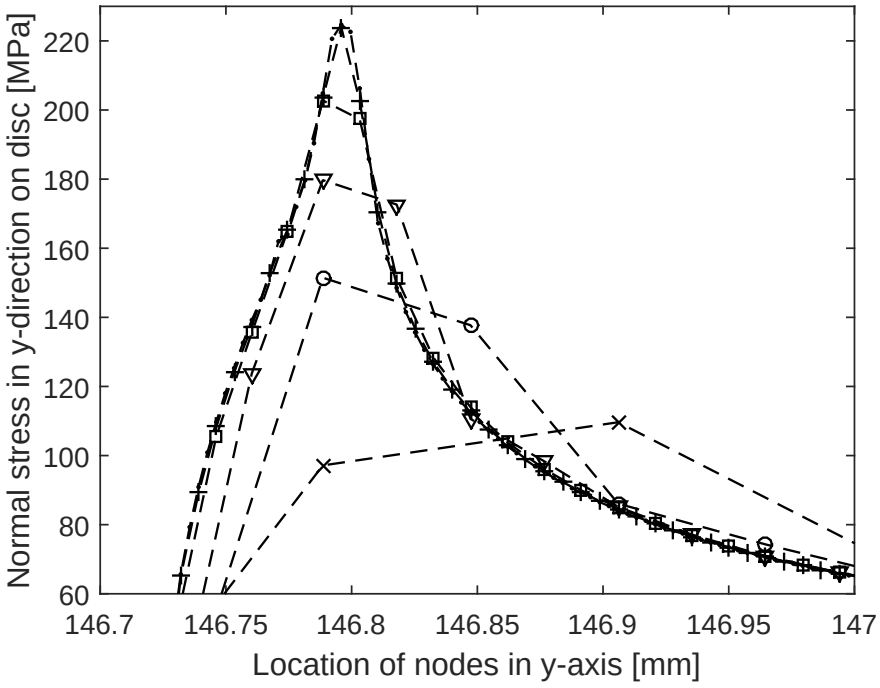


(b) Zoomed view on the peak location

Figure 3.31: Normal stress in x-direction σ_x on the blade for three global and three submodels on the defined path

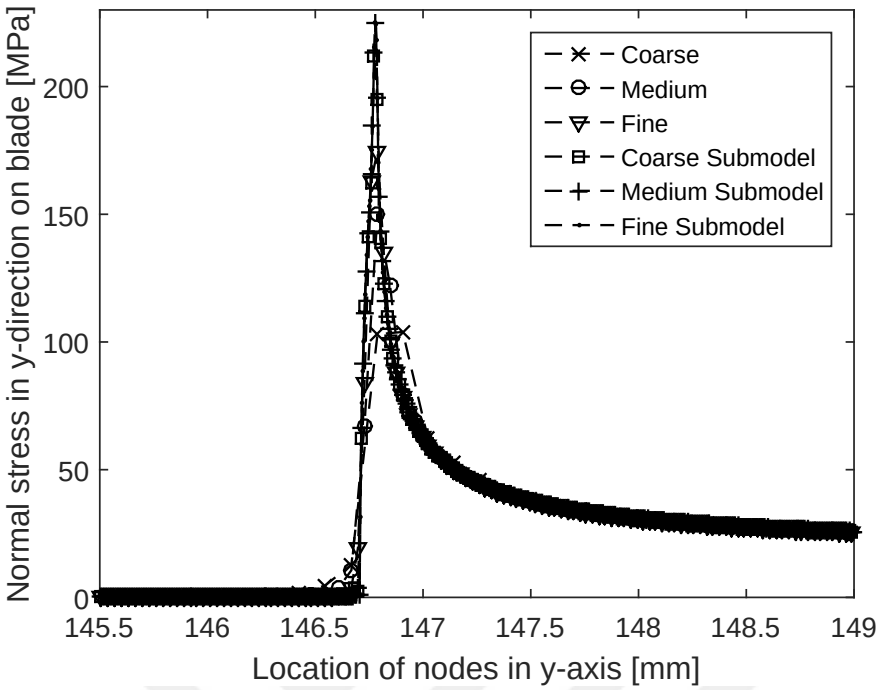


(a) General view

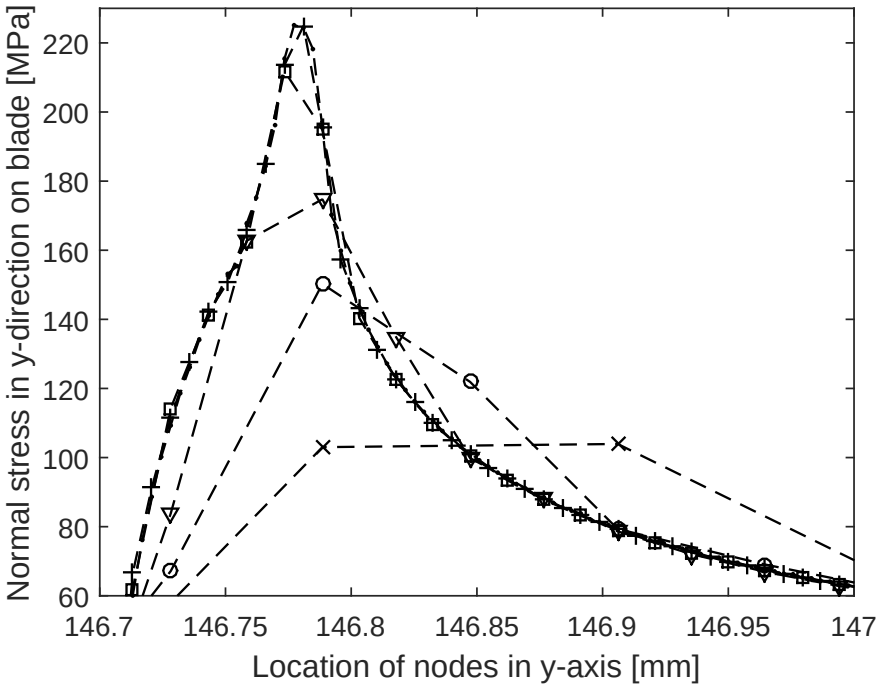


(b) Zoomed view on the peak location

Figure 3.32: Normal stress in y-direction σ_y on the disc for three global and three submodels on the defined path

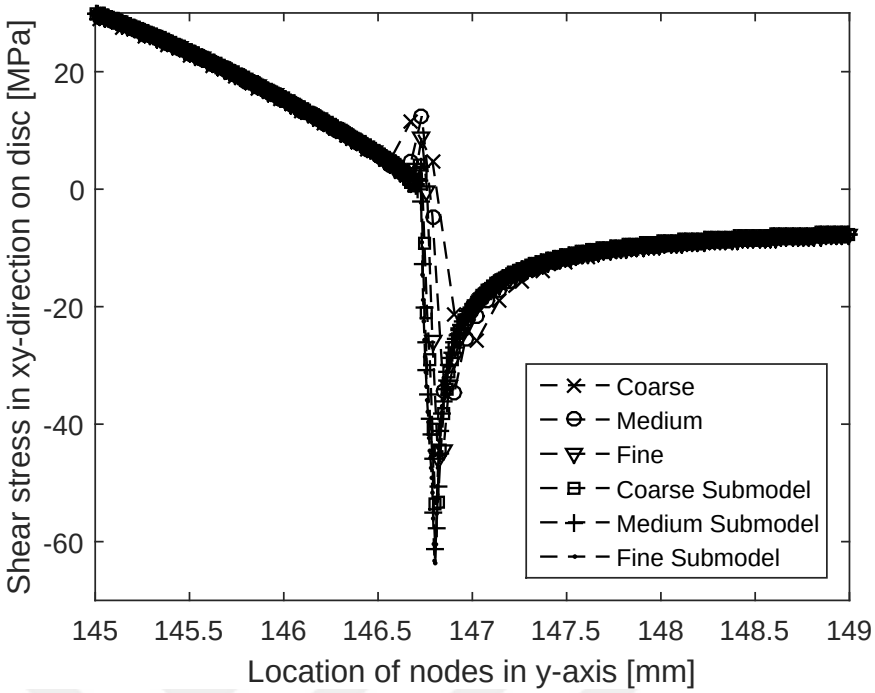


(a) General view

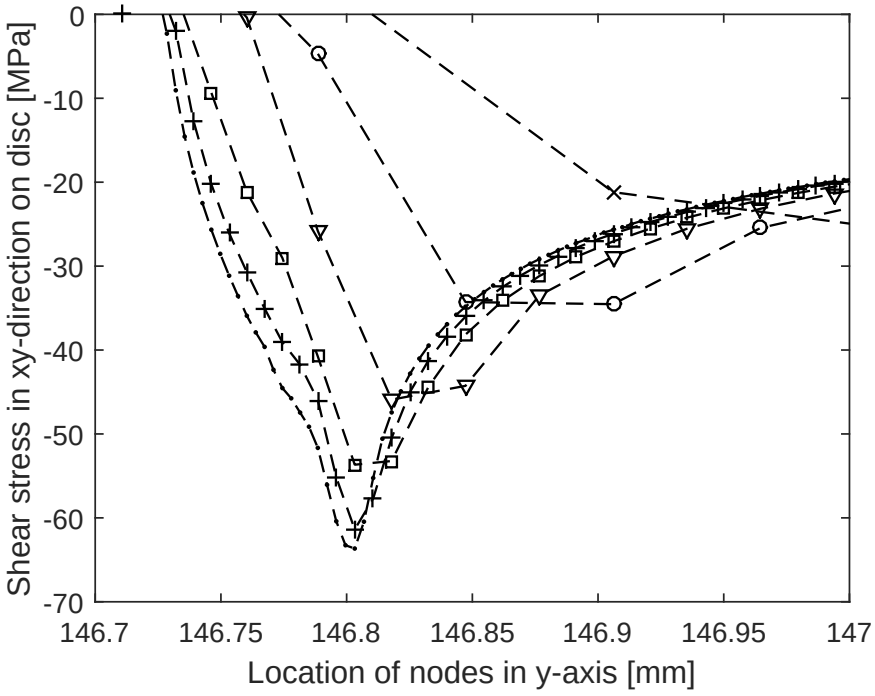


(b) Zoomed view on the peak location

Figure 3.33: Normal stress in y-direction σ_y on the blade for three global and three submodels on the defined path

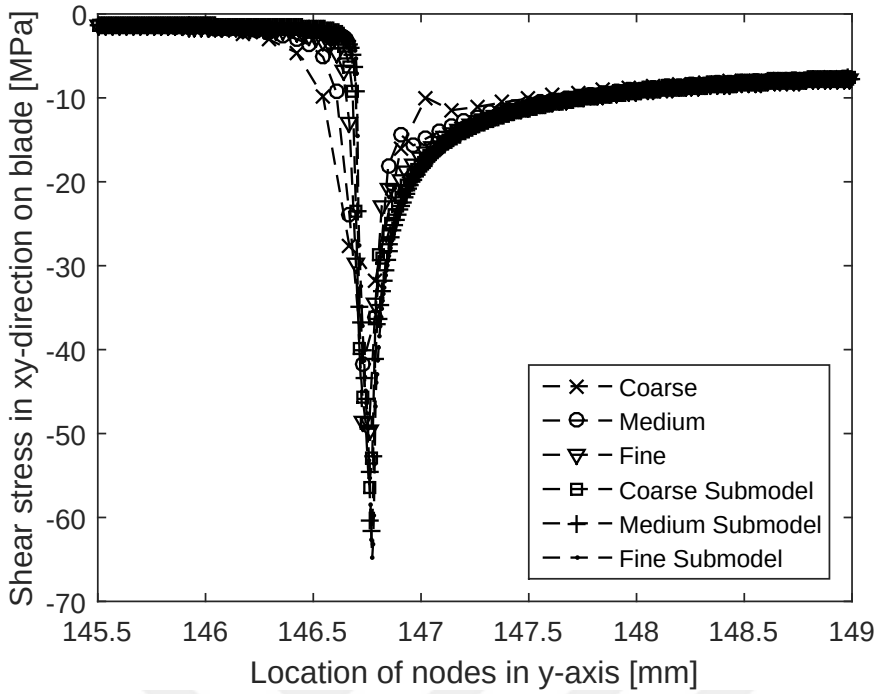


(a) General view

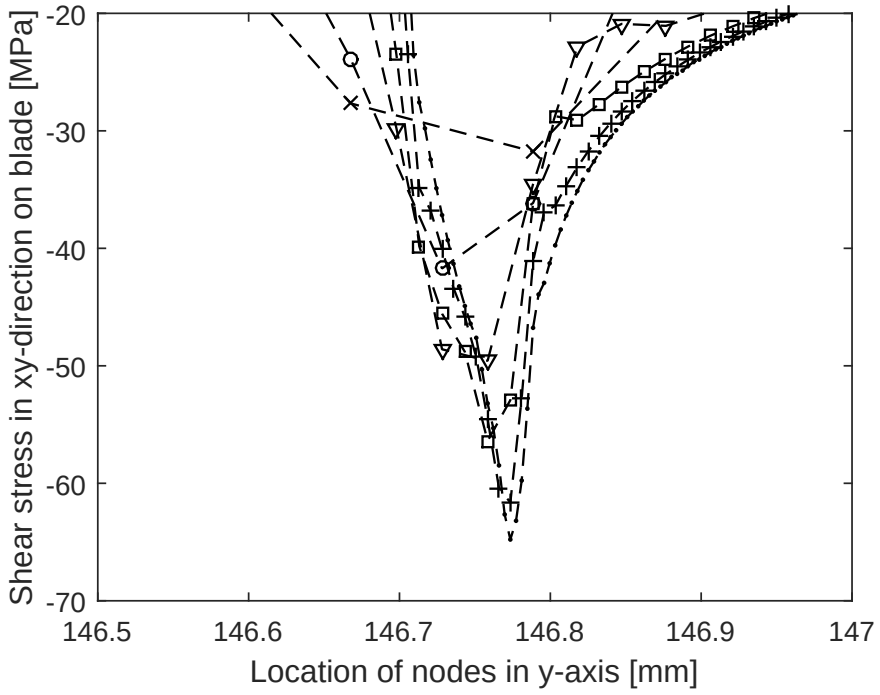


(b) Zoomed view on the peak location

Figure 3.34: Shear stress in xy-direction τ_{xy} on the disc for three global and three submodels on the defined path



(a) General view



(b) Zoomed view on the peak location

Figure 3.35: Shear stress in xy-direction τ_{xy} on the blade for three global and three submodels on the defined path

Furthermore, in order to compare the accuracy of the submodel, two more global models are created with smaller mesh sizes compared to fine global model. These models are called as the superfine (S) and the extra-superfine (ES) global models. Meshing parameters used to create these two finer models are given in Tables 3.16 and 3.17. In Figure 3.21, edge names associated with these sizing are highlighted on dovetail geometry. This approach is not logical computational-wise; however, it is possible to ensure the correctness of the submodelling approach. The results of these models are presented in Figure 3.36. It is seen that two lines of the different models are almost on top of each other. Solution times of the global models and the submodels are presented in Table 3.18. It is observed that the fine submodel has the accuracy close to the extra-superfine global model with a eight-nine times quicker solution time.

Table 3.16: Mesh parameters used outside of the boundary layer for superfine (S) and extra-superfine (ES) global models

Edge Name	**Superfine Mesh (S)**	**Extra-superfine Mesh (ES)**	**Type of Sizing**
L1_t	4	8	element size [mm]
L1_r	4	8	number of division
L_2	16	32	number of division
L_3	48	96	number of division
L_4	24	48	number of division
L_5	24	48	number of division
L_6	48	96	number of division

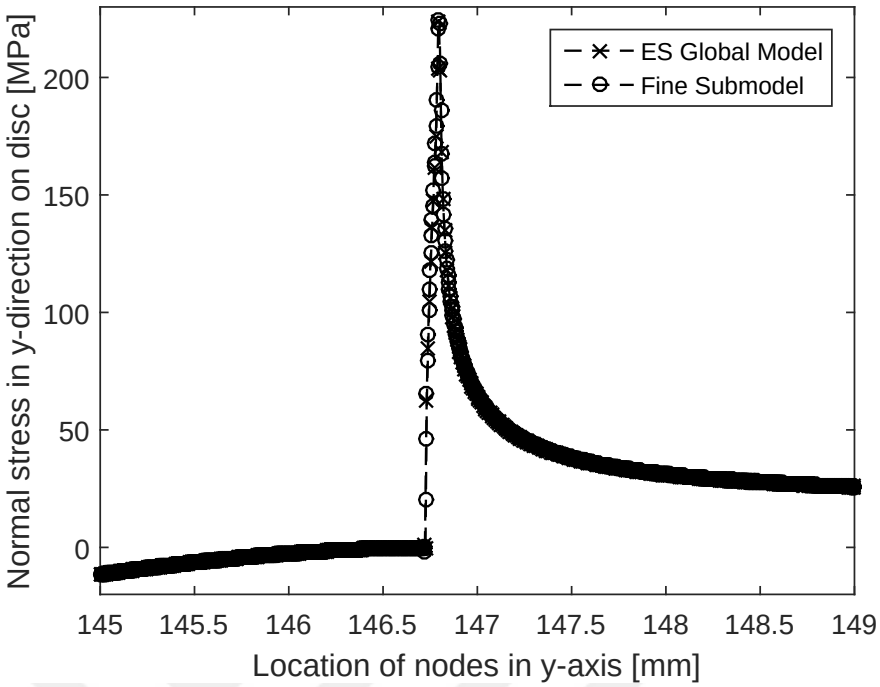
Table 3.17: Mesh parameters used inside of the boundary layer for superfine (S) and extra-superfine (ES) global models

Edge Name	**Superfine Mesh (S)**	**Extra-superfine Mesh (ES)**	**Type of Sizing**
boundary layer	0.015625	0.0078125	element size [mm]
N_1	288	576	number of division
N_2	64	128	number of division
N_3	128	256	number of division
N_4	512	1024	number of division
N_5	320	640	number of division
N_6	80	160	number of division
N_7	96	192	number of division
N_8	384	768	number of division

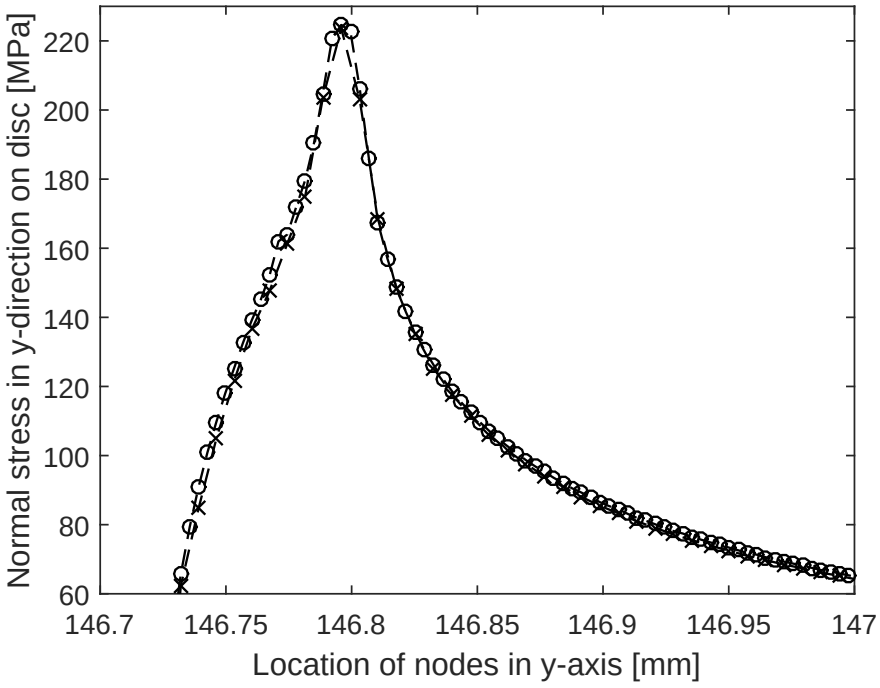
Table 3.18: Solution times of the global models and the submodels

	Solution Time [s]				
Models	**Coarse**	**Medium**	**Fine**	**Superfine**	**Extra-superfine**
Global Model	20.0	60.8	229.0	840.3	6664.6
Submodel	48.7	197.5	800.5	N/A	N/A

The loadings and the boundary conditions of the dovetail model is taken from [1]. To validate the results obtained, the converged contact stress results in the article are presented in Figure 3.37. In the article, a 3D dovetail model is solved. In the figure, the axis shown with "x/a" defines the contact line between the disc and the blade, and the axis shown with "y/a" represents the thickness direction. The stress peak located around (x/a = -0.1) is the location of the peak stress that is converged in this study. In the figure, it is seen that the maximum converged contact stress has an approximate value of 210-220 MPa, which is consistent with the contact stress results (σ_y) obtained with the submodelling given in the Table 3.15.



(a) General view



(b) Zoomed view on the peak location

Figure 3.36: Normal stress in y-direction σ_x on disc for extra-superfine global model and fine submodel on the defined path

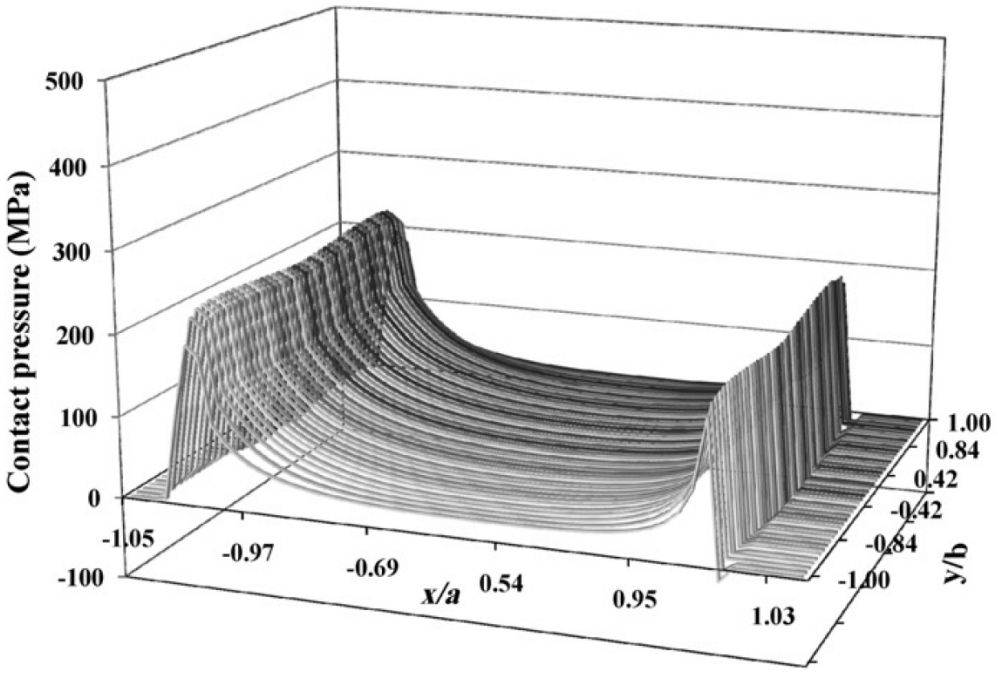


Figure 3.37: Contact stress distribution between the disc and the blade [1]

CHAPTER 4

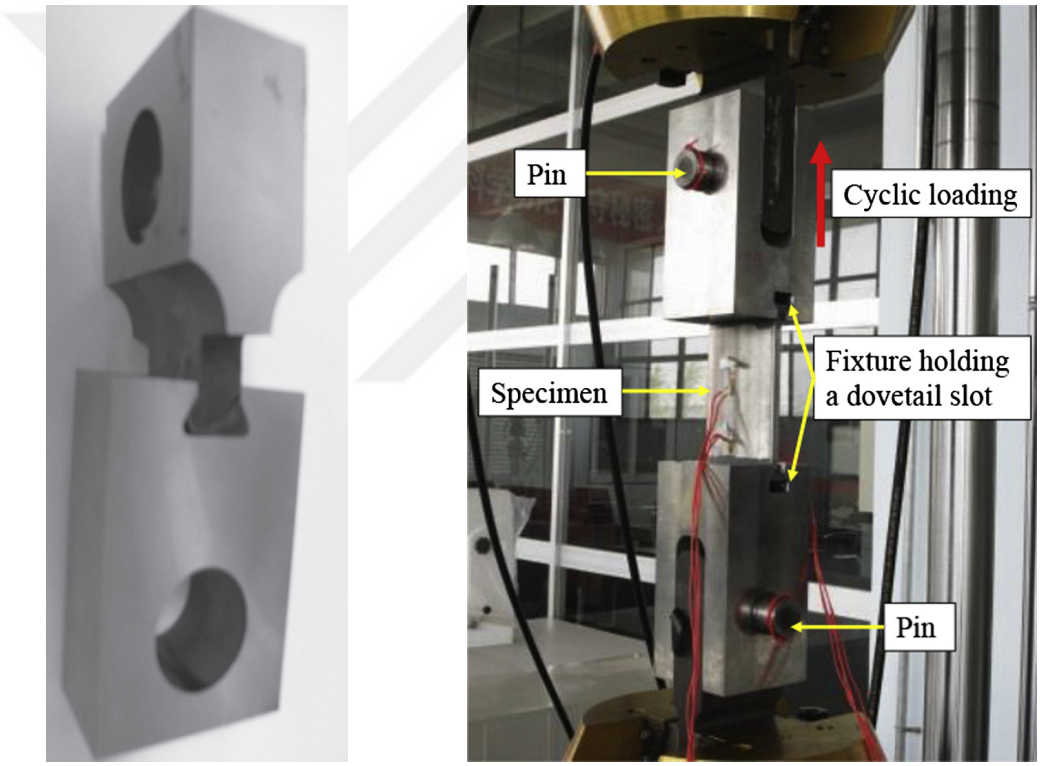
EXPERIMENTAL STUDY OF THE DOVETAIL SPECIMEN UNDER TENSILE LOADING AND VALIDATION WITH THE FINITE ELEMENT ANALYSIS

In this chapter, static tensile experiments are conducted on dovetail geometry. In the first Section 4.1, components of the test setup are introduced. Results of a preliminary finite element analysis of the experimental setup is presented in this section. Hence, experimental procedure is explained in this section as well. In the following Section 4.2, finite element models created to simulate the experiments are described. In the last Section 4.3, results of the experimental study and the finite element analysis are given. Moreover, causes of the discrepancies between the results are discussed in this section. In the Section 4.4, a third experiment conducted on the dovetail specimen is discussed. Finite element analysis comparison with the experimental results are conducted in this section. Hence, differences between the first two experiments and the last experiment are explained. In the last Section 4.5, a brief conclusion of the experimental studies is presented.

4.1 Experimental Study

At the design stage of the experiment, the configurations of the fatigue test set-ups in the literature are investigated. It is seen that to reduce the additional bending moment during the experiment, a pair of pins which are orthogonal to each other are used in the literature [19, 25]. The test set-ups investigated are shown in Figure 4.1. A similar design is used in the experiments conducted in this thesis study.

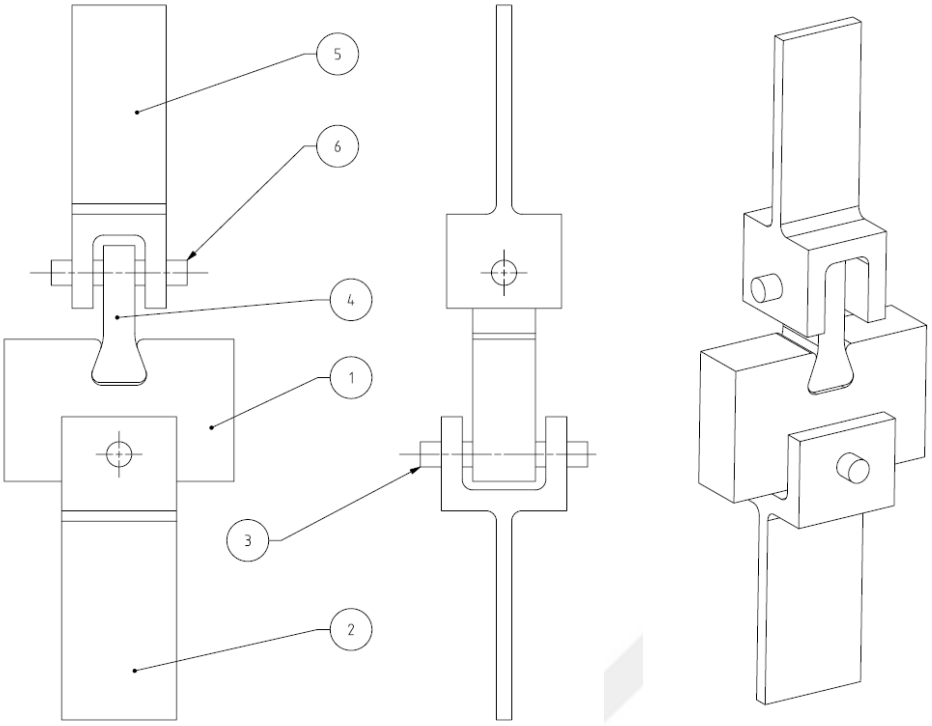
The dovetail specimen is subjected to a tensile loading of 20 kN. Components of the experimental setup are given in Figure 4.2. The components highlighted with numbers 1 and 4 are the disc and the blade specimens, respectively. The components identified with numbers 2 and 5 are the holders (adapters) that are designed to connect the specimens to the test set-up. The pins used to attach holders to specimens are indicated with numbers 3 and 6 in the figure. In order to determine the dimensions of the holders and pins to be used, a finite element model of the test set-up is created. In the following Section 4.1.1, the finite element model of the experimental set-up is presented. Then, in Sections 4.1.2-4.1.4 details of the components of the experimental setup are presented. In Section 4.1.5, experiment conducted on the dovetail specimen is discussed in detail.



(a) Test set-up introduced in [19]

(b) Test set-up introduced in [25]

Figure 4.1: Experimental set-up's used in the literature



(a) Front and right views of experimental set-up (b) Isometric view of experimental set-up

Figure 4.2: Components of the experimental setup

4.1.1 Preliminary Finite Element Analysis Model of the Experimental Setup

The finite element model of the experimental set-up is given in Figure 4.3. Loadings and boundary conditions are highlighted in the figure. Displacements of the pins their axes are constrained from the lateral surfaces of the pins as shown with letters A and B for the upper and the lower pins, respectively. Nodes highlighted with letters C, D, E and F in the figure represent the nodes that are held by the grips of the testing machine. 60 mm of the adapters are held by the grips of the tensile test machine. The load is applied from the bottom nodes. Boundary conditions applied are given in Table 4.1. In order to realize the realistic gripping conditions, displacements of the nodes highlighted with letters D and F in z direction are not constrained. However, to prevent the rigid body motion, displacements of their counter nodes highlighted with letters C and E are constrained in z direction. A total force of 20 kN is applied as two 10 kN forces to the two faces of the bottom adapter.

Frictional contact with a friction coefficient of 0.3 is defined between the disc and the

Table 4.1: Boundary conditions of the finite element model of the experimental setup

Boundary Condition ID	Displacement in x-direction [mm]	Displacement in y-direction [mm]	Displacement in z-direction [mm]	Applied force in y-direction [kN]
A	0	free	free	0
B	free	free	0	0
C	0	0	free	0
D	0	0	0	0
E	0	free	free	-10
F	0	free	0	-10

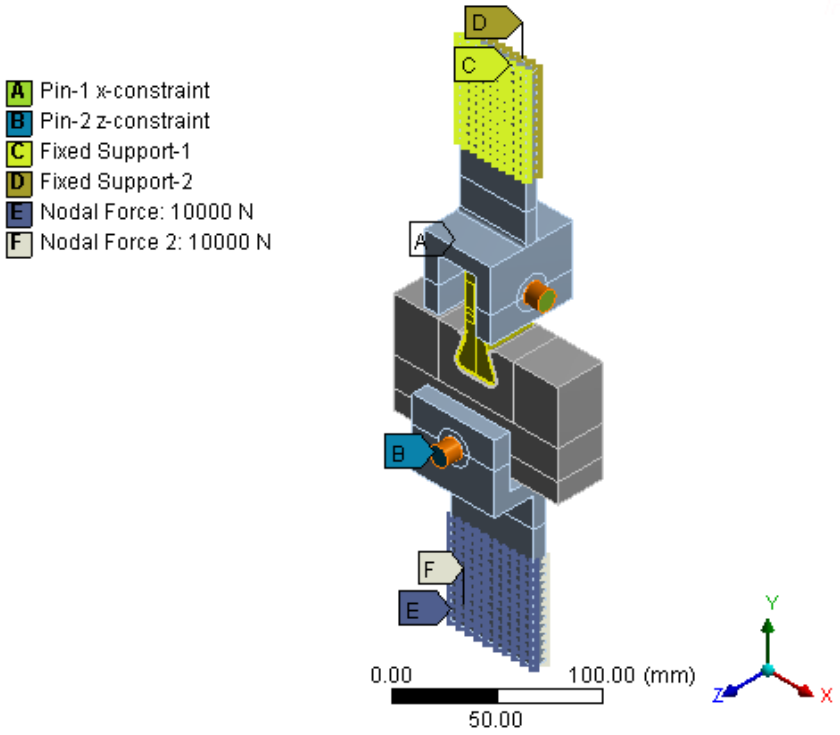


Figure 4.3: Finite element model of the experimental setup with loadings and boundary conditions

blade specimens. The Normal Lagrange formulation is used as contact enforcement method. Frictionless contacts are used to formulate the contact between the holders and the pins, and between the pins and the specimens.

3D finite element analysis of the model is carried out in one load step. Auto time stepping of the ANSYS is used with an initial substep size of 40, and minimum and maximum substep sizes of 25 and 40, respectively. Materials used in the analysis are

assumed to have isotropic linear elastic behaviour.

The finite element mesh of the experimental setup model is presented in Figure 4.4. Linear quadrilateral elements are used in the analysis. The finite element model consists of 296500 nodes and 291026 elements.

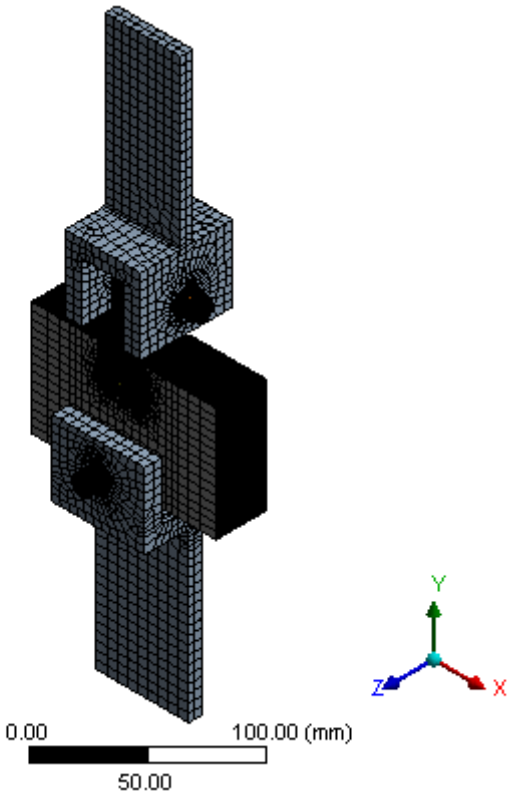


Figure 4.4: Finite element mesh grid of the experimental setup

4.1.2 Specimen

Geometric features of the blade and the disc specimen are given in Figures A.1 and A.2, respectively. Specimens are manufactured from Inconel 718 Alloy - AMS 5663. Material properties are given in Table 4.2.

Table 4.2: Material properties of Inconel Alloy 718 - AMS 5663

Elastic Modulus [GPa]	**Poisson's Ratio [-]**	**Density [g/cm^3]**	**Yield Strength [MPa]**
203	0.29	8.22	1030

Due to the loading and the boundary conditions discussed in Section 4.1.1 high stress

gradients occur around the upper hole region of the blade part. An equivalent stress contour plot of the specimen is given in Figure 4.5. It is seen that the maximum equivalent stress on the specimen under 20 kN tensile loading is around 630 MPa which is significantly lower than the yield stress of the Inconel Alloy 718 (1030 MPa). Therefore, the presented specimen design for the disc and the blade is in the elastic limits and may be used for the experiment.

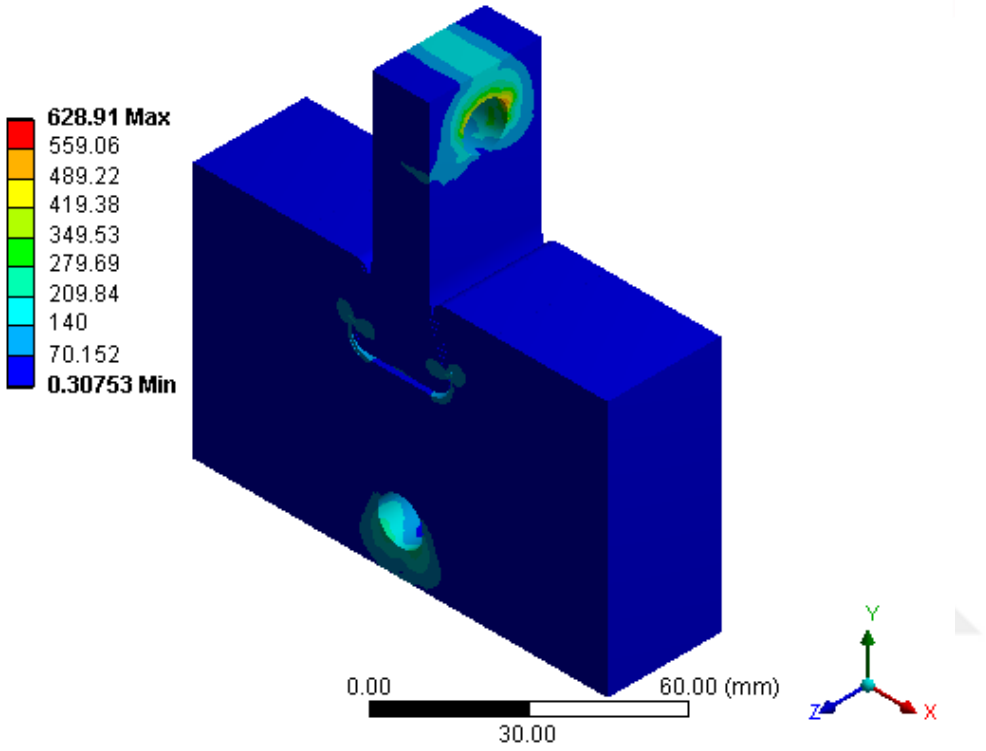


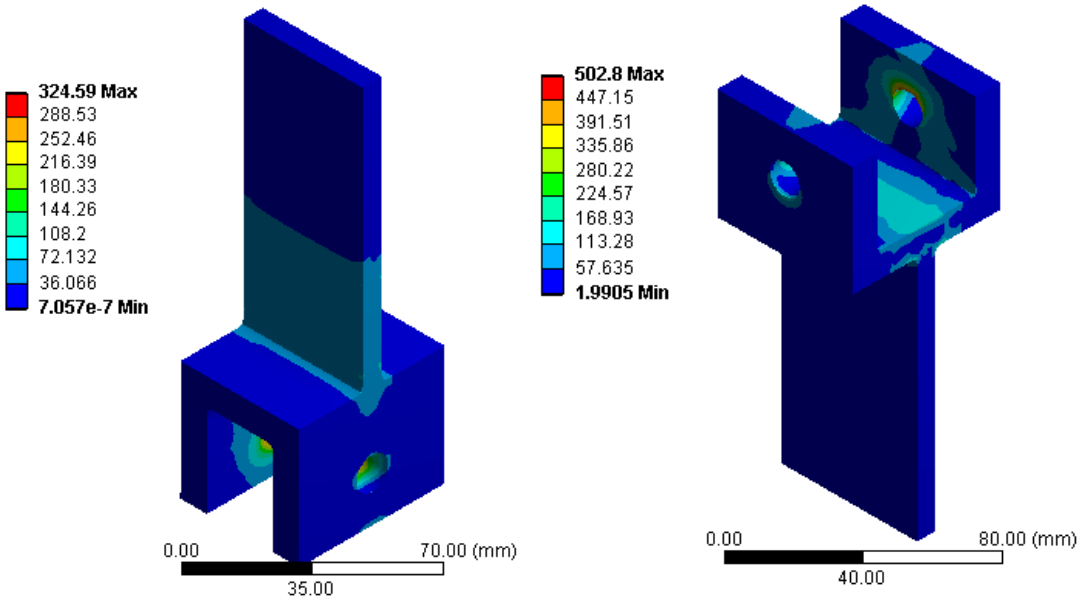
Figure 4.5: Equivalent stress on the specimen under 20 kN tensile loading

4.1.3 Holders

Geometric dimensions of the holders (adapters) are given in Figures A.3 and A.4 for the upper and the lower adapters, respectively. Materials used for the production of the adapters is Inconel 718 Alloy - AMS 5663. Material properties of the alloy is given in Table 4.2.

In Figure 4.6, equivalent stress plots of the upper and the lower holders are presented. It is seen that the maximum stress values for the upper and the lower adapters are around 325 MPa and 500 MPa, respectively. Yield point of the material used for the

adapters is given as 1030 MPa. It can be deducted that the adapters will be in the elastic range at the experiment under the 20 kN tensile loading.



(a) Upper adapter (b) Lower adapter

Figure 4.6: Equivalent stress on the adapters under 20 kN tensile loading

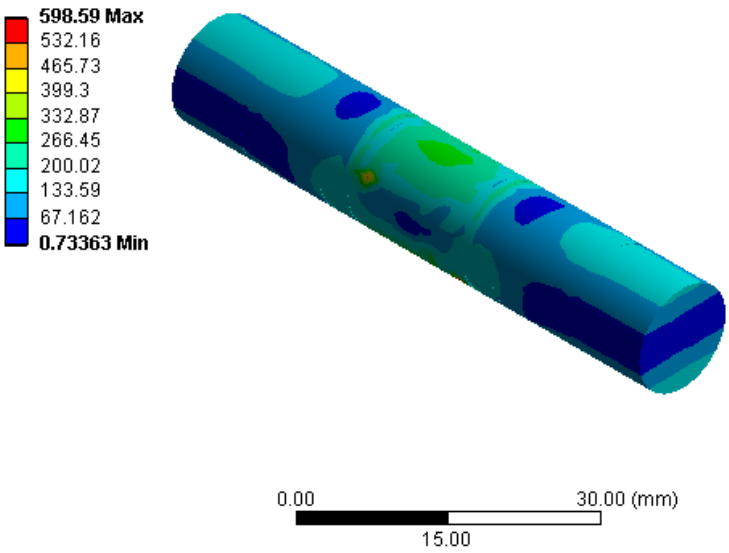
4.1.4 Pins

In the experiment, steel bolts with grade 12.9 are used as pins. In the finite element analysis, material properties of the structural steel are used for the pins. Material properties are given in Table 4.3.

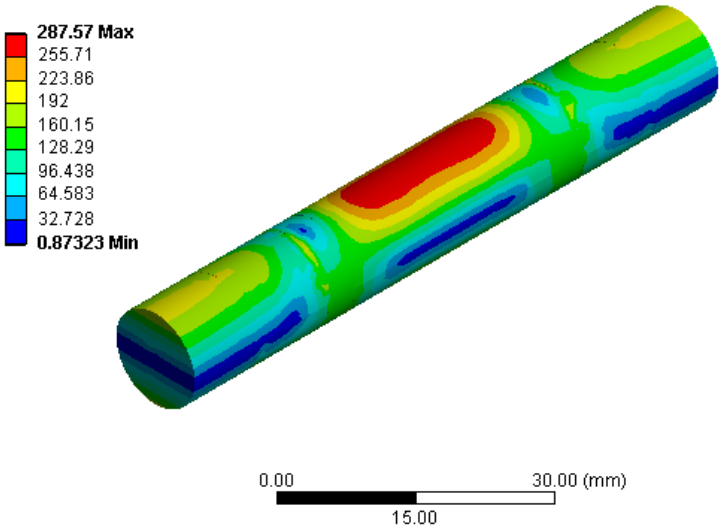
Table 4.3: Material properties of 12.9 grade structural steel

Elastic Modulus [GPa]	**Poisson's Ratio [-]**	**Density [kg/m^3]**	**Yield Strength [MPa]**
200	0.3	7850	1080

The pins are used for transferring the load between the adapters and the specimen. Due to the 20 kN applied tensile load, high stressed areas are seen on the pins. In Figure 4.7, it is highlighted that the maximum equivalent stress on the upper and the lower pins are around 600 MPa and 290 MPa, respectively. Yield limit for the 12.9 grade steel bolts are given as 1080 MPa. Therefore, the pins stay in the elastic range for the applied 20 kN tensile load.



(a) Upper pin



(b) Lower pin

Figure 4.7: Equivalent stress on the pins under 20 kN tensile loading

4.1.5 Experimental Setup

Two sets of experiments are conducted on the dovetail specimen. In the first experiment only the digital image correlation (DIC) technique is used to investigate the results of the experiment. In the second experiment, strain gauges are mounted to the pre-determined locations. Hence, the DIC technique is used together with the strain gauge measurements in the second experiment.

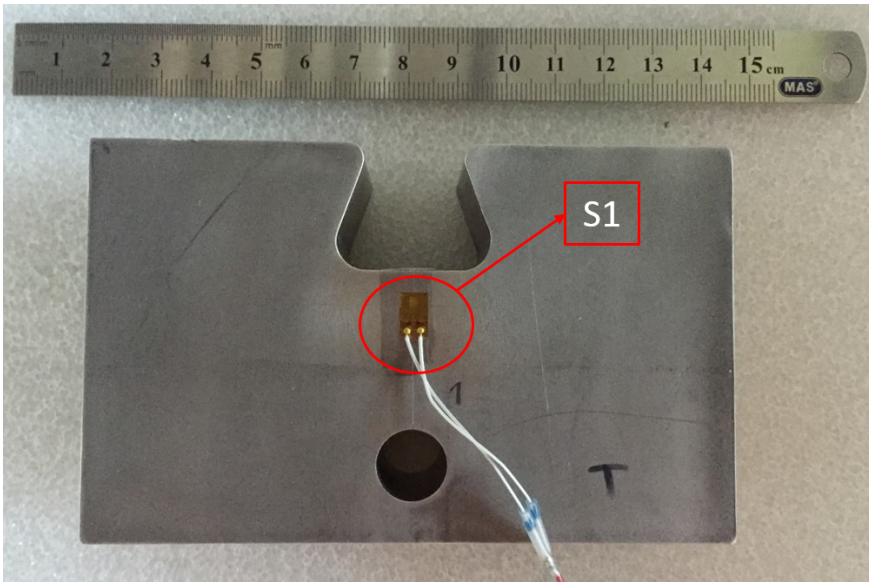
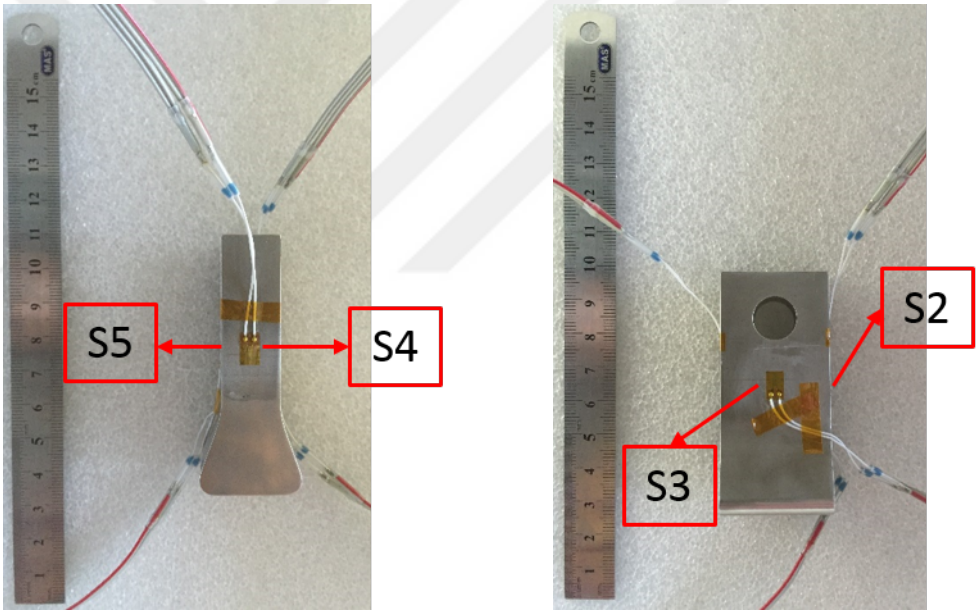


Figure 4.8: Strain gauge location on the disc specimen



(a) Front view (b) Side view

Figure 4.9: Strain gauge locations on the blade specimen

A total of 5 strain gauges are glued on to the specimen as 4 on the blade specimen and 1 on the disc specimen. All of the strain gauges measure the strain in the direction of the applied load (y direction). In Figure 4.8, location of the first strain gage (S1) on the disc specimen is presented. Remaining four strain gages are mounted on the four sides of the blade specimen as shown in Figure 4.9. Each of the two strain gages on the

counter faces (S2-S4 and S3-S5) share the same y-coordinate on the blade specimen. The reason for such a configuration is to check possible eccentricity that may occur during the experiment. Ideally, it is expected to have the same strain readings on the strain gages S2-S4 and S3-S5. In Figure 4.10, strain gage connections to the data acquisition system is presented. Strain measurements are taken with a frequency of 2 Hertz.

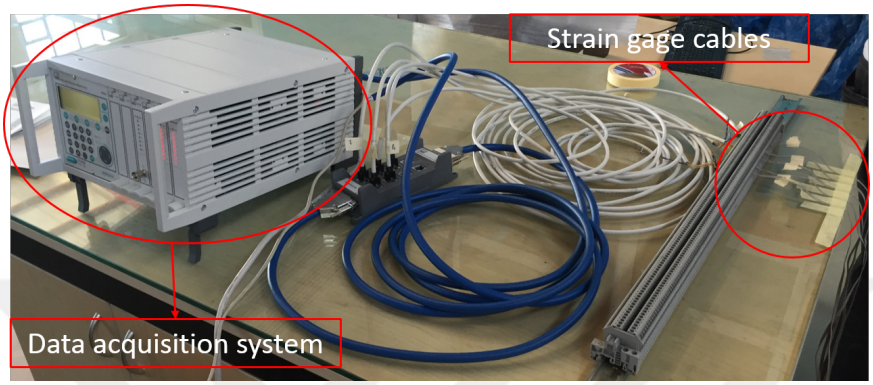
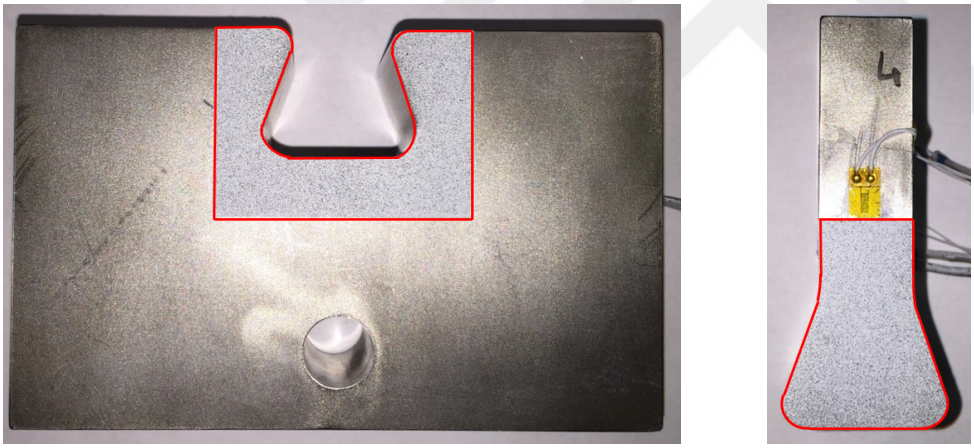


Figure 4.10: Strain gage connections to the data acquisition system



(a) On the disc

(b) On the blade

Figure 4.11: DIC paintings

Digital image correlation system (DIC) is capable of both taking 2-dimensional (2D) and 3-dimensional (3D) measurements. In the first experiment, a 3D digital image correlation (DIC) technique is used. However, due to the longer analysis time and harder calibration of the 3D digital image correlation, the results obtained in the first experiment are regarded as unsatisfactory. Therefore, 2D measurements are done in the second experiment. For this purpose, a pre-determined area of interest is painted

for DIC. Painted areas are the areas inside the red curves in Figure 4.11. Depending on the size of the painted area, DIC camera is set to a pre-defined distance. In Figure 4.12, the camera used for the DIC measurements is shown together with the test setup. DIC measurements are taken in a frequency of 1 Hertz. Start-up of the DIC system and strain gage measurements are done simultaneously just before the initiation of the experiment.

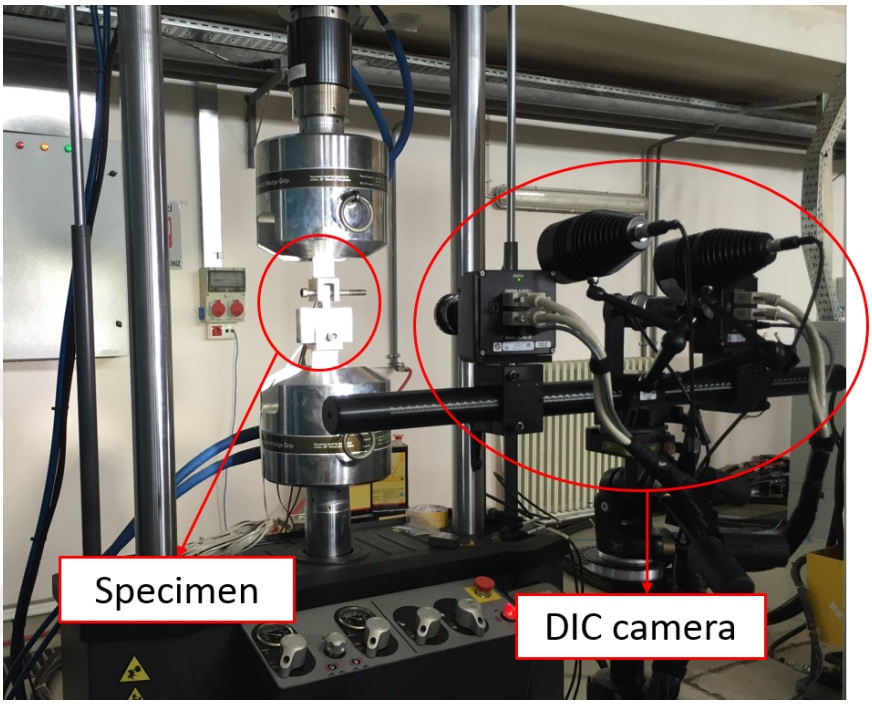


Figure 4.12: Experimental setup and DIC camera

In Figure 4.13, experimental setup is presented. MTS tensile testing machine with maximum tensile load capacity of 250 kN is used. 60 mm part of the adapters are placed inside the grips of the tensile testing machine. The upper grip fixes the specimen and the load is applied from the bottom grip. The experiment is carried out in a load-controlled way with a loading rate of 0.5 kN per second. The load spectrum of the experiment is presented in Figure 4.14. The experiment takes 83 seconds with 40 seconds of loading time, 5 seconds of dwell time and 38 seconds of unloading time.

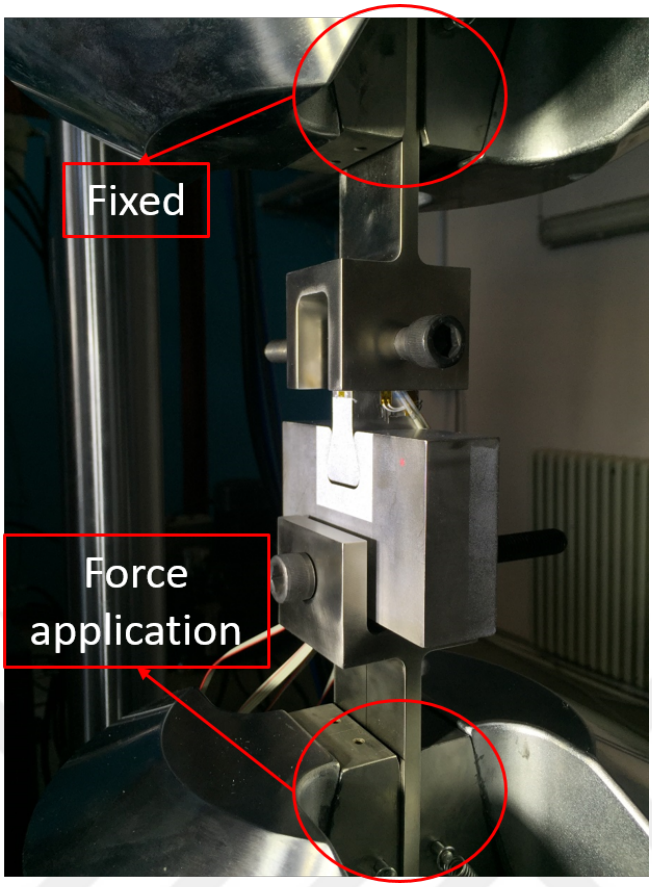


Figure 4.13: Experimental setup

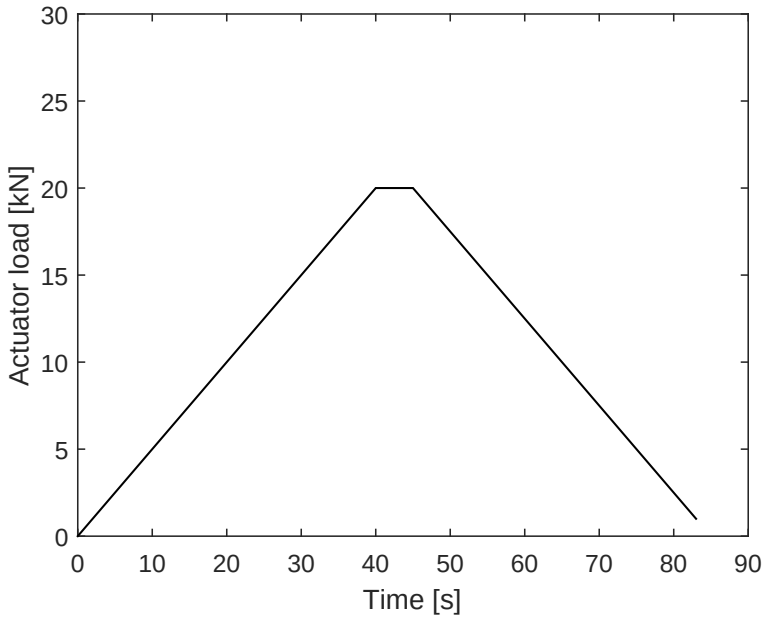


Figure 4.14: Loading rate

4.2 Finite Element Model of the Experimental Setup

Two set of finite element models are created to simulate the behaviour of the experimental setup. 3D finite element analysis are carried out for the both model. Specimens and adapters are manufactured from Inconel 718 - AMS 5563, and structural steel is used for pins. Material properties of the Inconel 718 and structural steel is given in Tables 4.2 and 4.3, respectively.

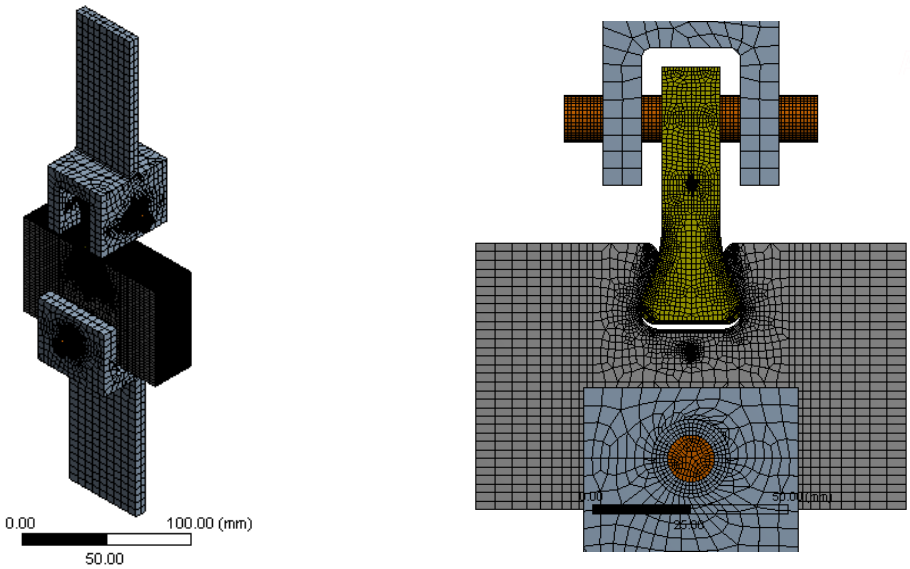
4.2.1 Full Finite Element Model of the Experimental Setup

The first model introduced is similar to the model used at the preliminary analysis conducted at the design stage of the experimental setup (Section 4.1.1). The model consists of all components of the experimental setup (adapters, pins and specimen).

The analysis is carried out in two load steps. The first step is the loading step until 20 kN maximum load is achieved and the second step is the unloading step until 1 kN load. The loading step is carried out in 10 substeps and the substep size of the unloading step is set as program controlled. Boundary conditions given in Table 4.1 and in Figure 4.3 of the previous section are used for the full finite element model of the experimental setup.

The finite element mesh of the full model of the experimental setup is given in Figure 4.15. Linear quadrilateral elements are employed. The finite element model has 195719 nodes and 195698 elements. 0.5 mm element size is defined at the contact region between specimens and 1 mm element size is defined in the thickness direction (z direction). At the strain gauge locations, rectangular surfaces with 1.5 mm width and 3 mm height are defined and these surfaces are finely meshed with an element size of 0.25 mm. An example of these meshes are highlighted in Figure 4.16 for the strain gauge on the disc specimen (S1).

There exist 6 contact regions on the model. These contact areas are highlighted in Figure 4.17. For the contacts between pins and adapters, and between pins and specimens all curved surface of the pins and inner surfaces of the holes are defined as contact surfaces. For these contact definitions with frictionless or frictional contact,



(a) Full setup

(b) Specimens section

Figure 4.15: Finite element mesh of the full model of the experimental setup

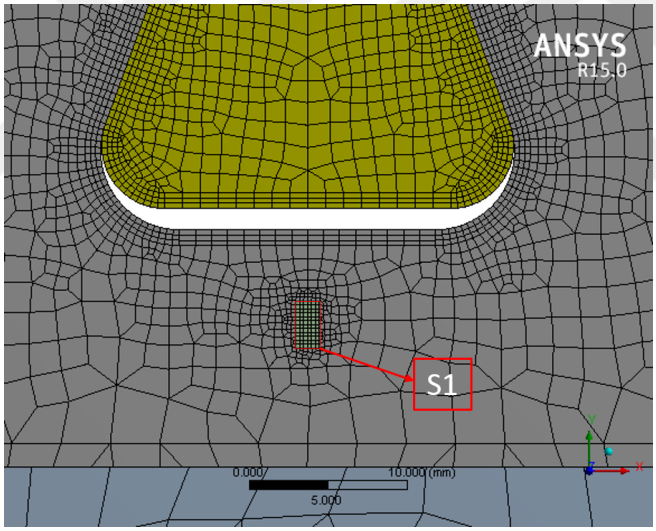
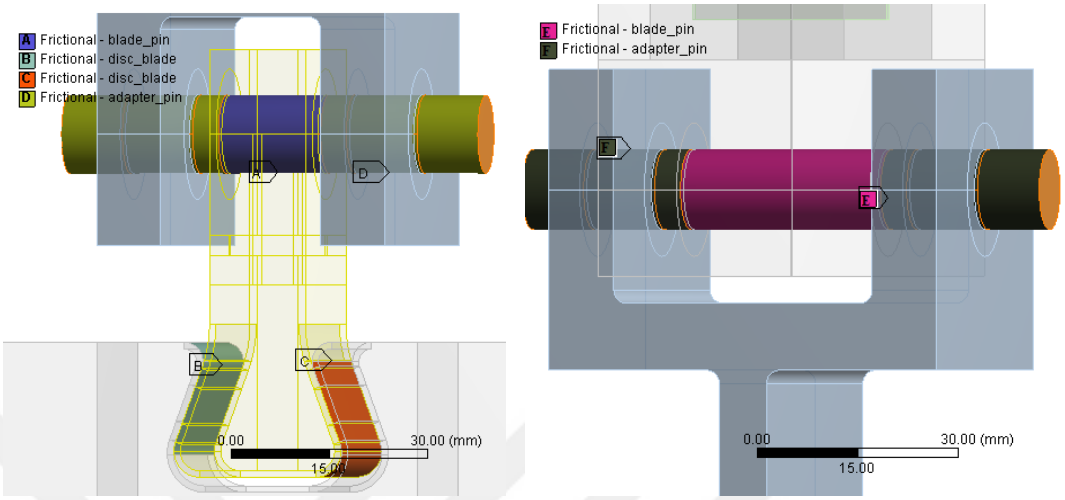


Figure 4.16: Refined mesh at the location of the strain gauge on the disc

it is not advised to define only the half of the surface of the holes and pins, which will be in the contact with the presence of loading, as contact areas. Such definitions of the contact yield an unrealistic change in the stiffness of the global system at the first substep of the analysis. However, if bonded contact is going to be used for these contact definitions, then half of the surface of the holes and pins should be defined as contact areas, since introducing all of the surfaces of the pins and holes as contact

areas will add extra unrealistic stiffness to system.

Frictional contact with a friction coefficient of 0.3 is defined for all the contact pairs with the Normal Lagrange formulation.



(a) Upper contact region (b) Lower contact region

Figure 4.17: Contact regions of the full model of the experimental setup

4.2.2 Simplified Finite Element Model of the Experimental Setup

The second model used to simulate the experimental setup is the simplified model which includes only the specimens (the disc and the blade) and disregards the adapters and pins. The simplified model with the boundary conditions is shown in Figure 4.18.

The analysis of the model is carried out in two load steps. At the first step, a 20 kN loading is applied in -y direction to the nodes highlighted with letter A in Figure 4.18 and at the second step, unloading is performed until a 1 kN force in -y direction. The loading step is applied in 10 substeps and the substep size of the unloading step is selected as program default option of the ANSYS. Displacements of the nodes highlighted with letter B are constrained in all direction for the both load steps. As it is seen from the figure, boundary conditions are applied to the nodes on the relevant half surfaces of the holes, since in the experiment pins are in the contact with the holes from these surfaces.

The finite element mesh of the experimental setup is given in Figure 4.19. Linear

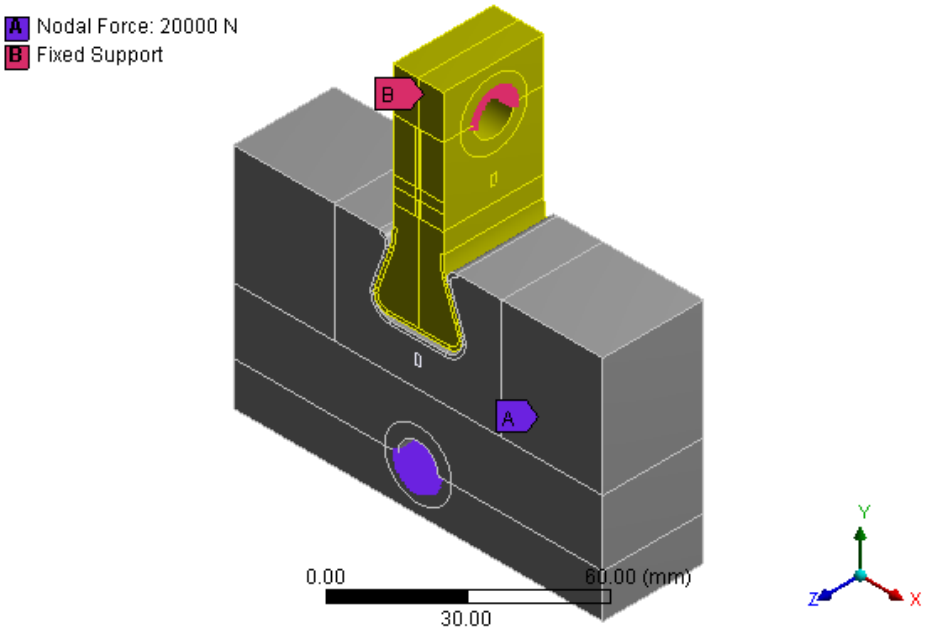


Figure 4.18: Boundary conditions of the simplified model

quadrilateral elements are employed. The finite element model consists of 113430 nodes and 109279 elements. 0.5 mm mesh size is defined on the region of contact and 1 mm element size is used in the thickness direction (z direction). Rectangular surfaces with size of 3 mm height and 1.5 mm width are defined on the location of the strain gauges. An example of the mesh in the neighbourhood of the strain gauge S3 on the blade is shown in Figure 4.20.

In total two contact pairs are defined between the disc and the blade. Contact surfaces are shown in Figure 4.21. Frictional contact with a 0.3 friction coefficient is defined. The Normal Lagrange formulation is used as the constraint enforcement method.

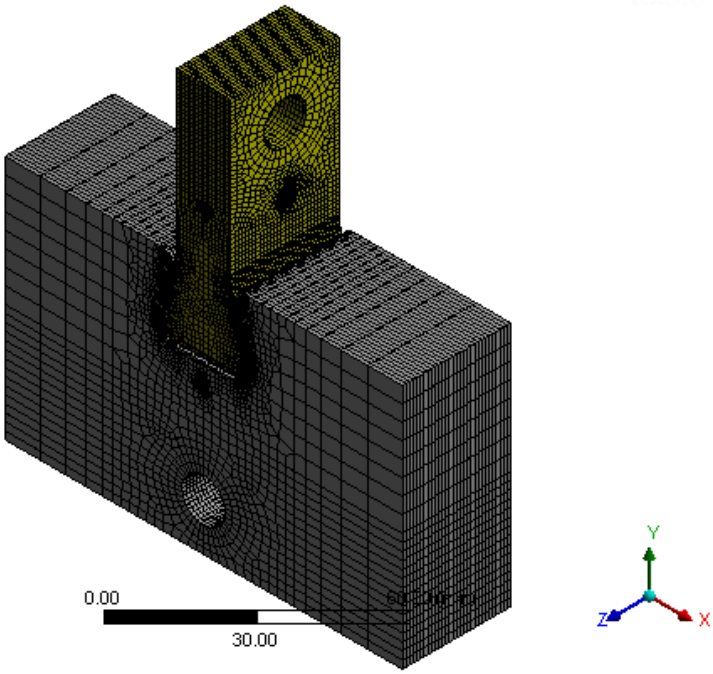


Figure 4.19: Finite element mesh of the simplified model of the experimental setup

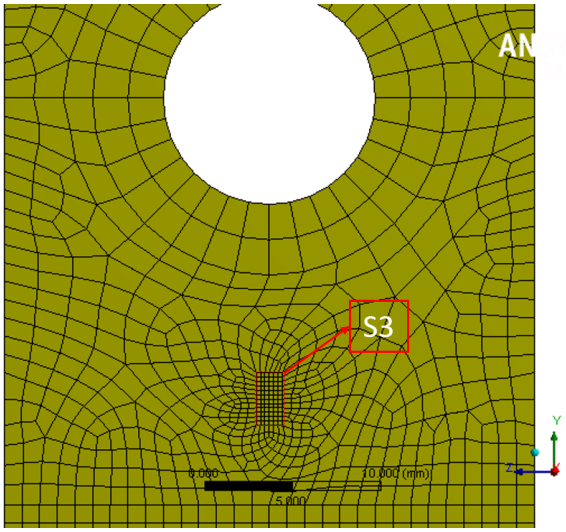


Figure 4.20: Refined mesh at the location of the strain gauge on the blade (S3)

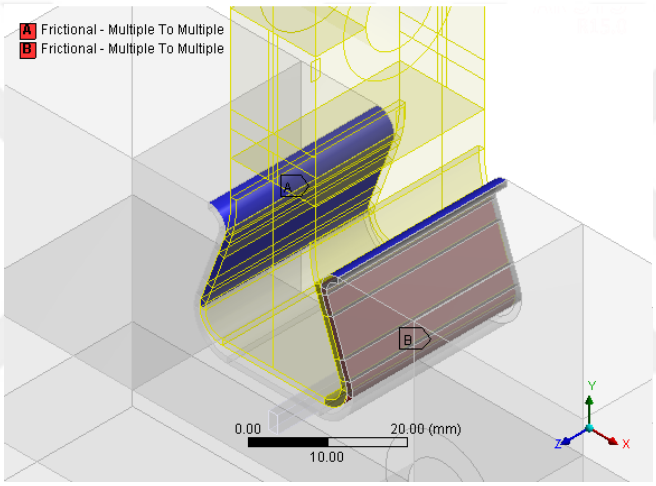


Figure 4.21: Contact regions of the simplified model of the experimental setup

4.3 Results

4.3.1 Experimental and Finite Element Analysis Results

Three different measurement techniques are used in the experiment. The load and the corresponding displacements are obtained from the tensile test machine. Strain readings are extracted from five strain gauges glued on the specimens. Lastly, for a full-field displacement and strain measurement of the blade and the disc digital image correlations (DIC) system is used. In the following sub-chapters, these results together with finite element analysis results are presented.

4.3.1.1 Global Load Displacement Results

From the software of the tension test setup, the loading data and their corresponding displacement values in the direction of the applied force is extracted. Force controlled finite element analysis is carried out. Average displacements of the nodes that are subjected to loading in the direction of loading are exported from the finite element analysis. For the simplified model, the load displacement data is not presented, since that model does not include the adapters and the pins. Load displacement curves of the experiment and the full finite element analysis of the experimental setup are given in Figure 4.22. In the experiment, it is seen that the global stiffness of the system shows a non-linear behaviour, whereas this behaviour is linear in the finite element analysis. For the both curves, it is observed that loading and unloading curves do not coincide.

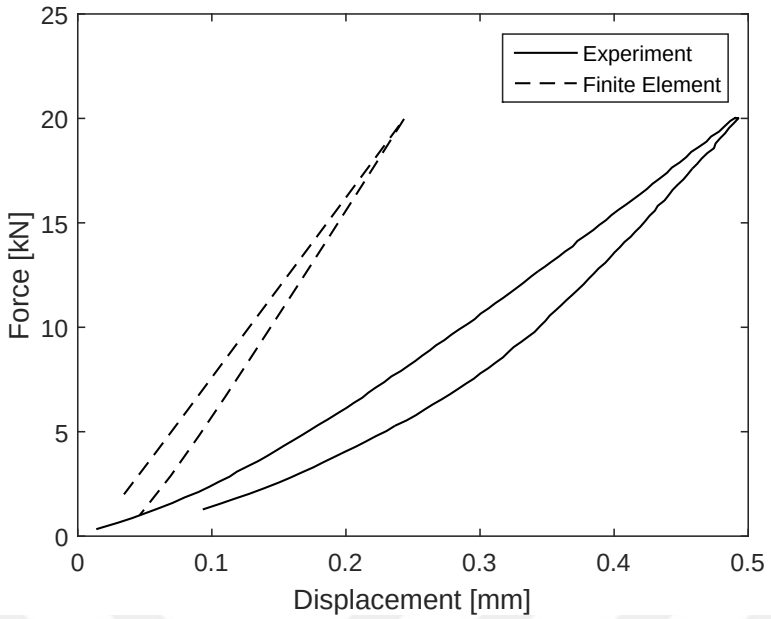


Figure 4.22: Load displacement curve of the system obtained from the tensile testing machine

4.3.1.2 DIC Results

Details of the area painted for the DIC measurement are explained in Section 4.1.5. In Figure 4.11, the area of interest is highlighted on the disc and the blade specimens. By post-processing the DIC results, it is possible to observe the behaviour of the contact between the specimens. During the experiment, 98 stages are captured by the DIC camera. Setting the initial stage as reference stage, displacements and strains in any desired stage are obtained.

The first observation made on DIC results is at the beginning of the experiment. With the presence of the loading, rigid body motions of the specimens are seen. To verify this observation, 11 stage points are defined on the specimens on various locations. In Figure 4.23, locations of these stage points are presented. Displacements of these stage points in x-direction are extracted and given in Figure 4.24. It is seen that all of the stage points defined on the specimens have a positive x displacement at the beginning of the experiment (until strain stage 12).

Moreover, rigid body motion can further be justified by investigating the displace-



Figure 4.23: Stage points defined on the specimens

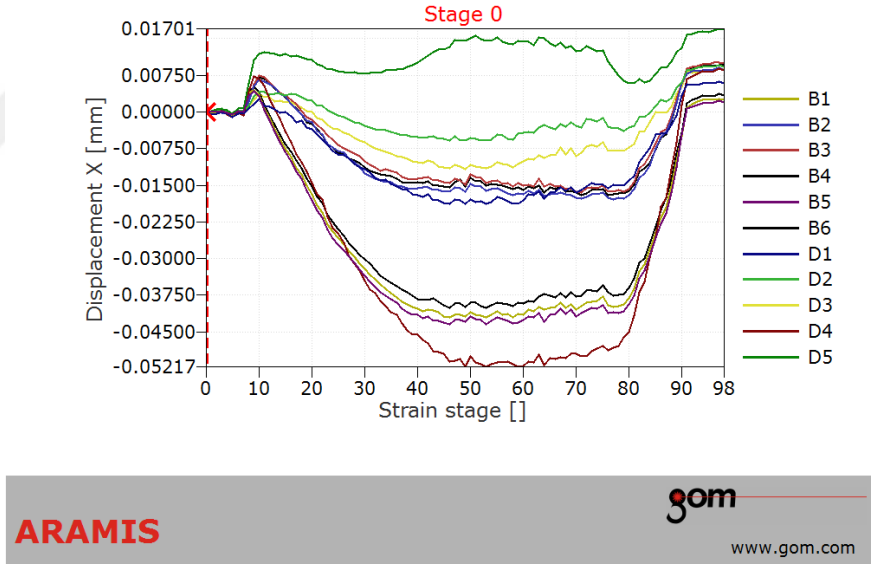


Figure 4.24: Displacements in x direction of the stage points defined on the specimens

ments of the stage points in y direction given in Figure 4.25. It is observed that the points defined on the disc specimen has a negative displacement in y direction at the end of the experiment. Hence, this displacement value roughly equals to the displacement values of those points at the beginning of the experiment (around strain stage 12). From these observations, it can be deducted that at the initial stages of the exper-

iment, specimens align themselves and close the gaps at the contact with rigid body motion. After that deformation of the bodies start.

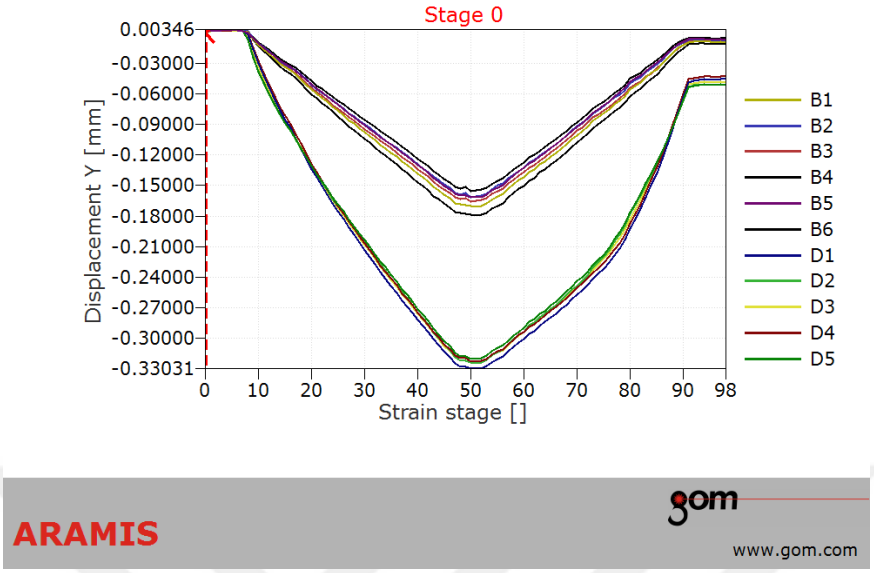
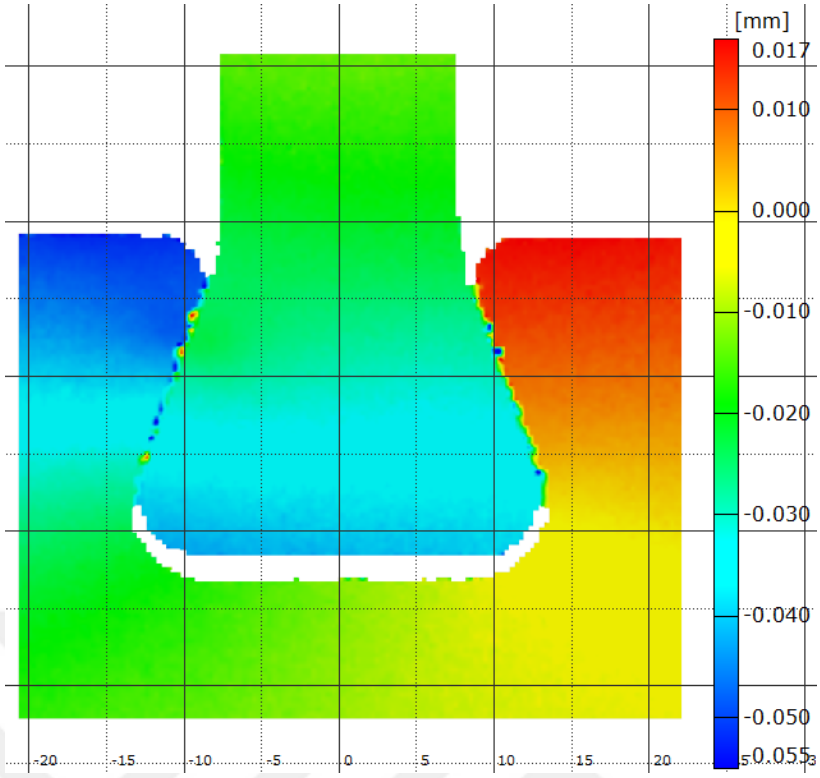
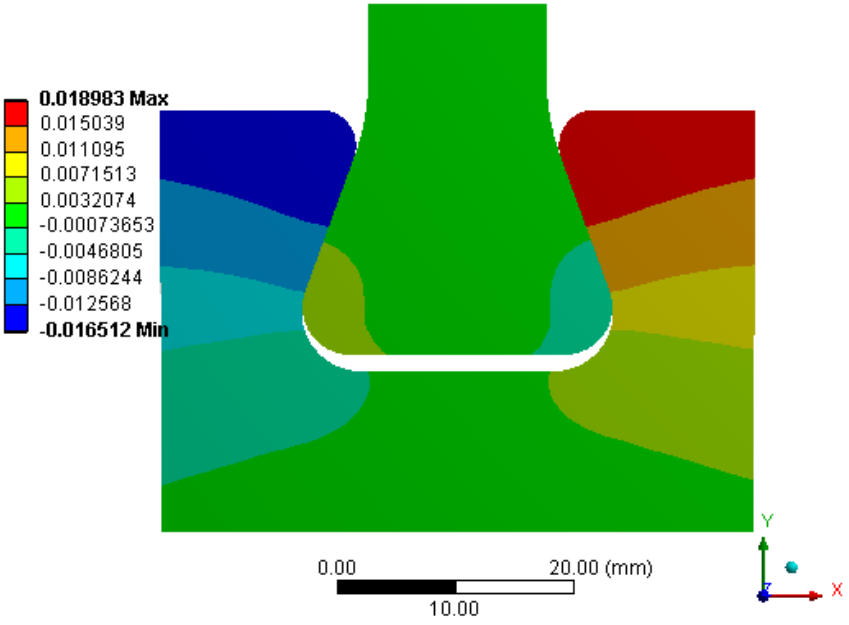


Figure 4.25: Displacements in y direction of the stage points defined on the specimens

The second observation made on the DIC results is the asymmetry in the experiment. In Figures 4.26 and 4.27, displacement in x and y directions for the DIC and the finite element analysis are visualized. By comparing the contours of the experiment and the finite element analysis, the symmetry in the finite element analysis contour is not seen in the experiment. Moreover, in Figure 4.28, von Misses strain contours for the experiment and finite element analysis are presented. In the experiment, peaks of the von Misses strain are localized in the regions of the lower parts of the right contact area and upper part of the left contact area. However, in the finite element analysis it is seen that peaks of the von Misses are observed at the same locations for the right and the left contact areas. This result further justifies the asymmetry in the experiment. A vertical path from the mid-line of the disc and the blade is defined on the DIC results as shown in Figure 4.29. In Figure 4.30, displacements of the points located on this path in x direction are presented. In an ideal case, it is expected to observe a zero displacement in x direction on this path. However, it is seen that throughout the experiment from stage 1 (initial stages) to stage 5 (stage of maximum loading), there exist non-zero x displacements of the points on the path defined. This behaviour further justifies the rigid body motion occurs during the experiment.

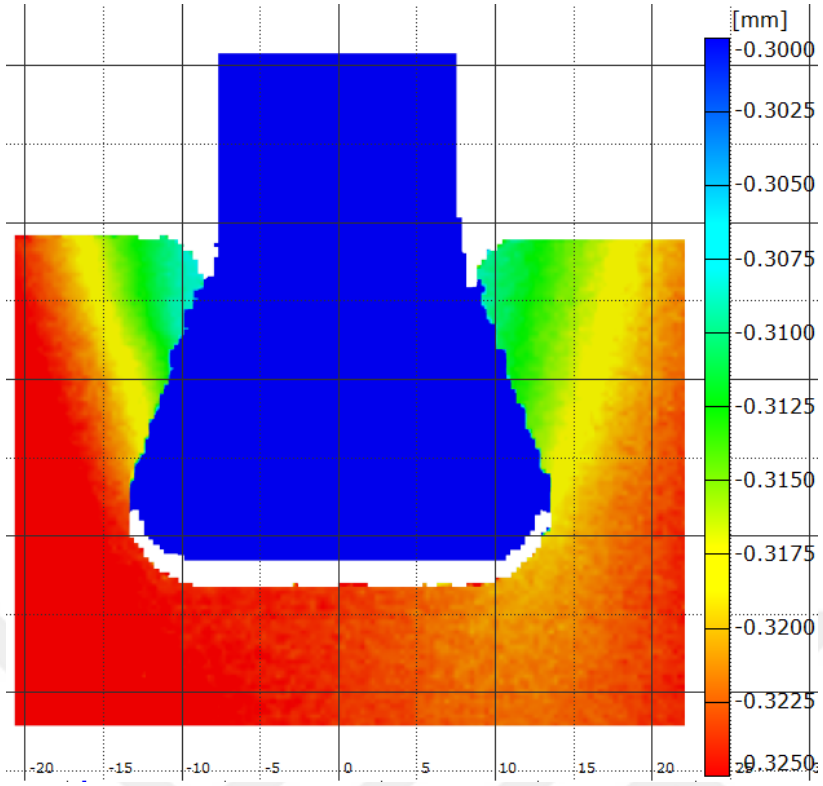


(a) Experiment

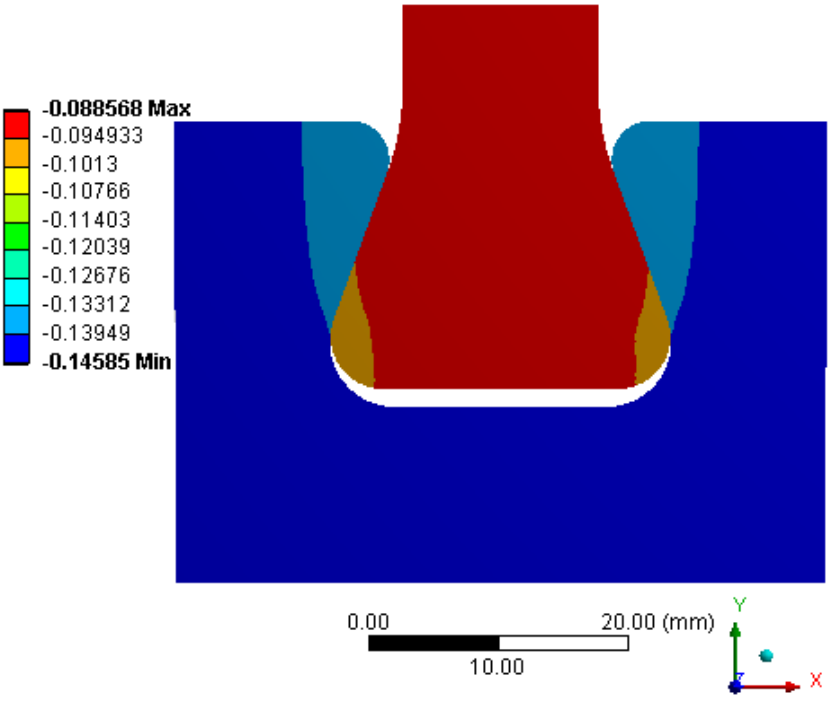


(b) Full finite element model

Figure 4.26: Displacements in x direction at the stage of 20 kN maximum load

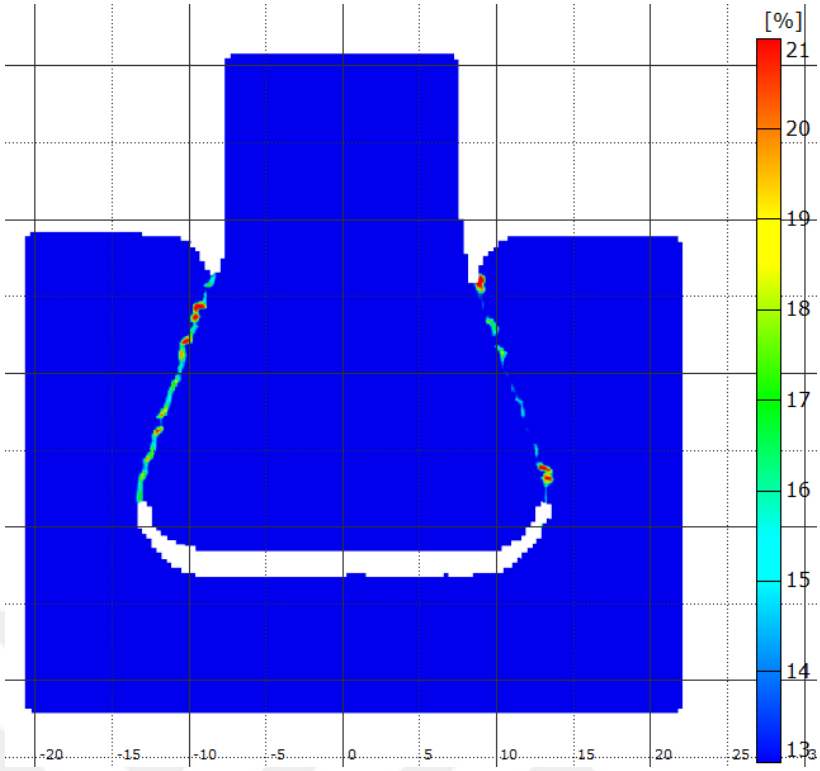


(a) Experiment

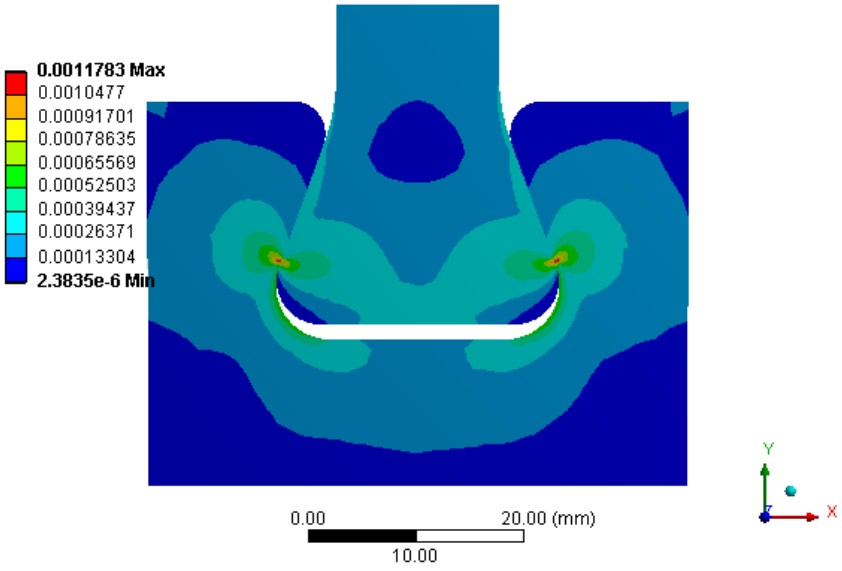


(b) Full finite element model

Figure 4.27: Displacements in y direction at the stage of 20 kN maximum load



(a) Experiment



(b) Full finite element model

Figure 4.28: Von Misses strain at the stage of 20 kN maximum load

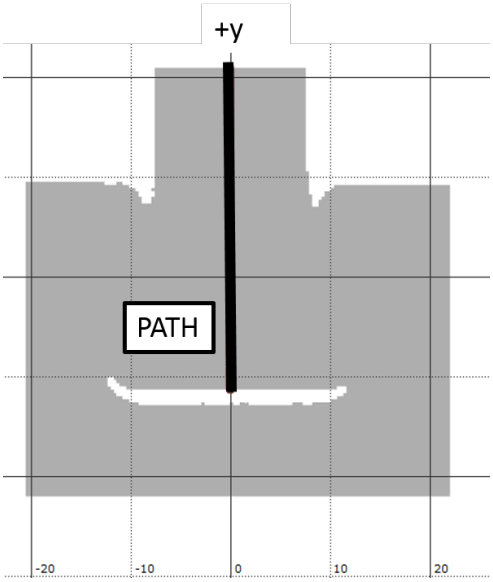


Figure 4.29: Path defined for the displacement output

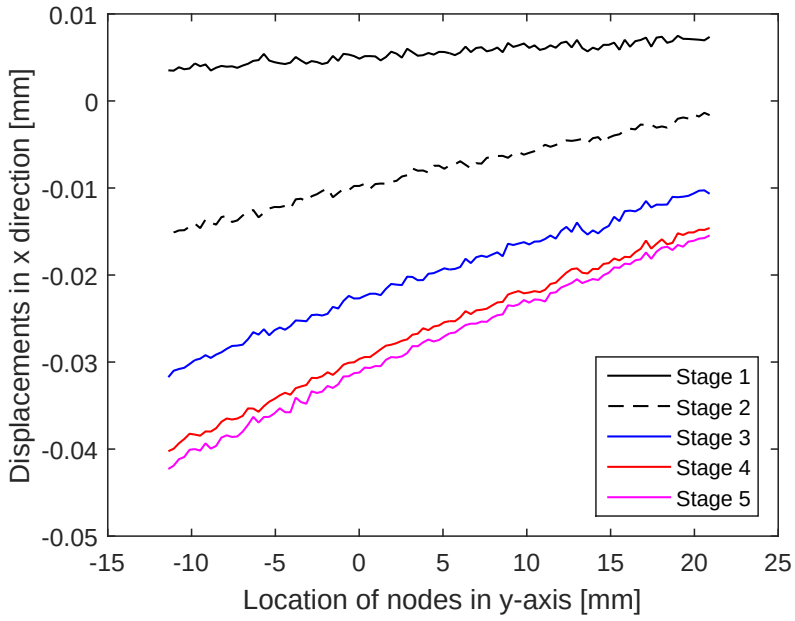


Figure 4.30: Displacements in x direction of the nodes that are located at the vertical path defined on the DIC results

Lastly, four paths are defined on the DIC results of the specimens. These paths are given in Figure 4.31. In the finite element model, nodes associated with the coordinates of these paths are selected. At every load step, the average displacement of each path in y direction is calculated. Then, relative displacements of the paths are calculated between paths 1 and 2, 1 and 3, and 1 and 4. Load displacement curves

are extracted by using these relative displacements. By using the relative displacements between the paths on the specimens, it is possible to remove the effects of the displacements caused by the pins and the adapters and focus on the specimens.

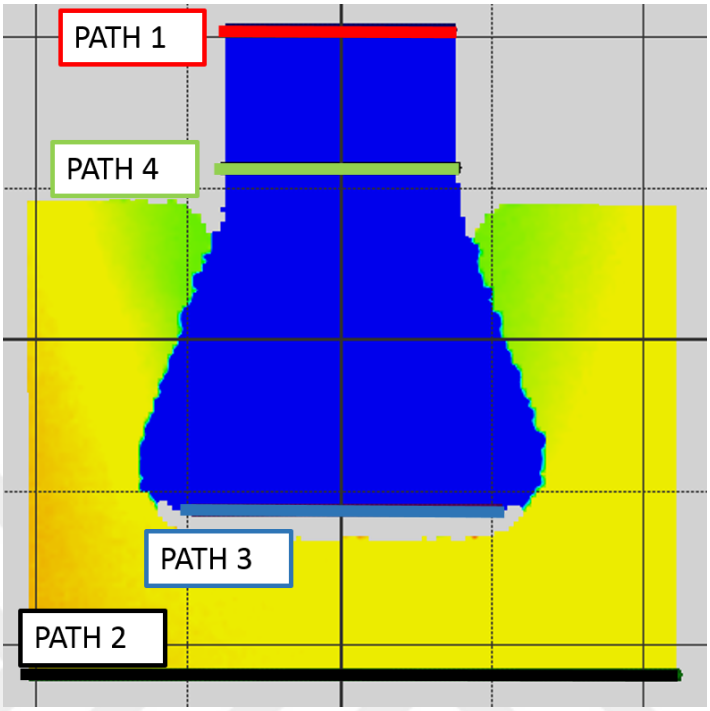


Figure 4.31: Paths defined on the specimens

Load displacement curves obtained by using relative displacements of the paths 1-2, 1-3 and 1-4 are given in Figures 4.32, 4.33 and 4.34. It is seen that the highest discrepancy between the experiment and the finite element results is for the one calculated between paths 1-2. Hence, the nonlinear behaviour observed in the global load displacement curve of the system (Figure 4.22) is seen on this result. Since the paths used in Figure 4.34 are selected on the same body and above away from the contact area, that gives the most consistent result. It actually demonstrates the material behaviour of the blade specimen.

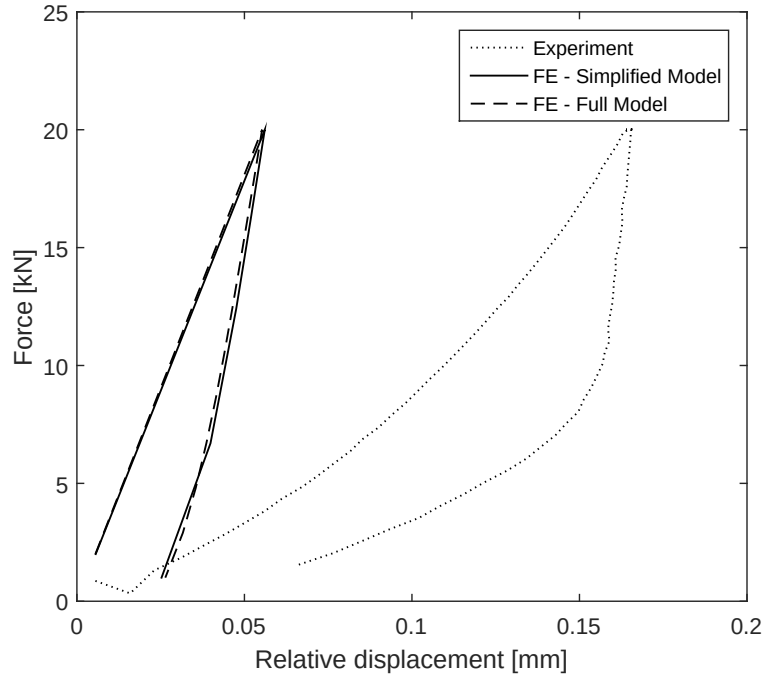


Figure 4.32: Load displacement curve of the system obtained from the relative displacements between paths 1 and 2

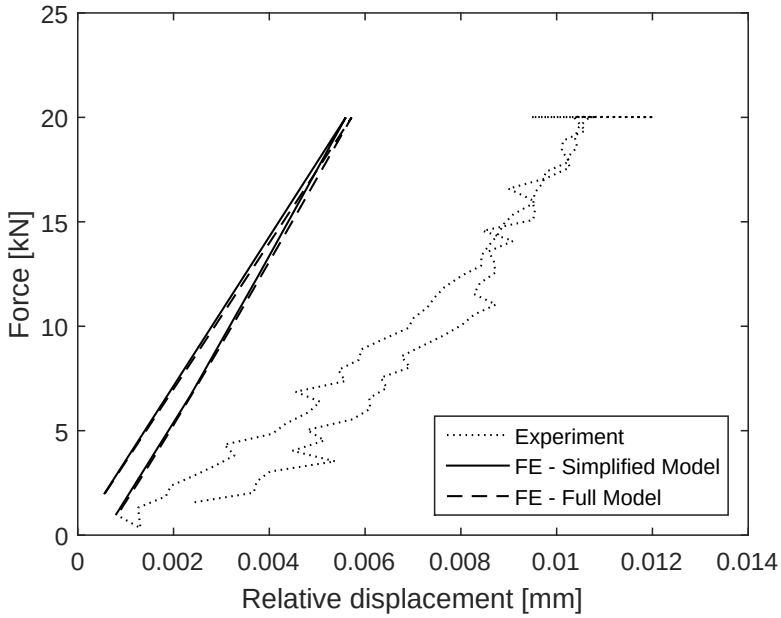


Figure 4.33: Load displacement curve of the system obtained from the relative displacements between paths 1 and 3

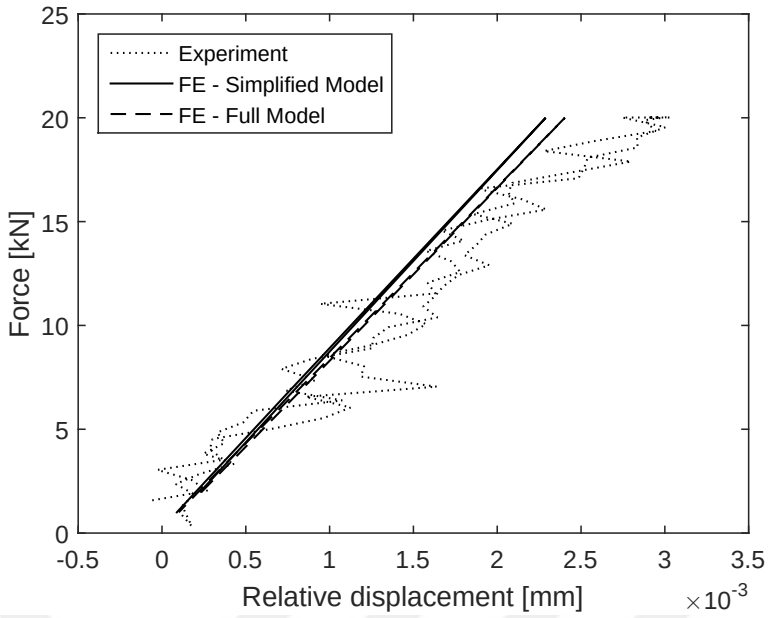
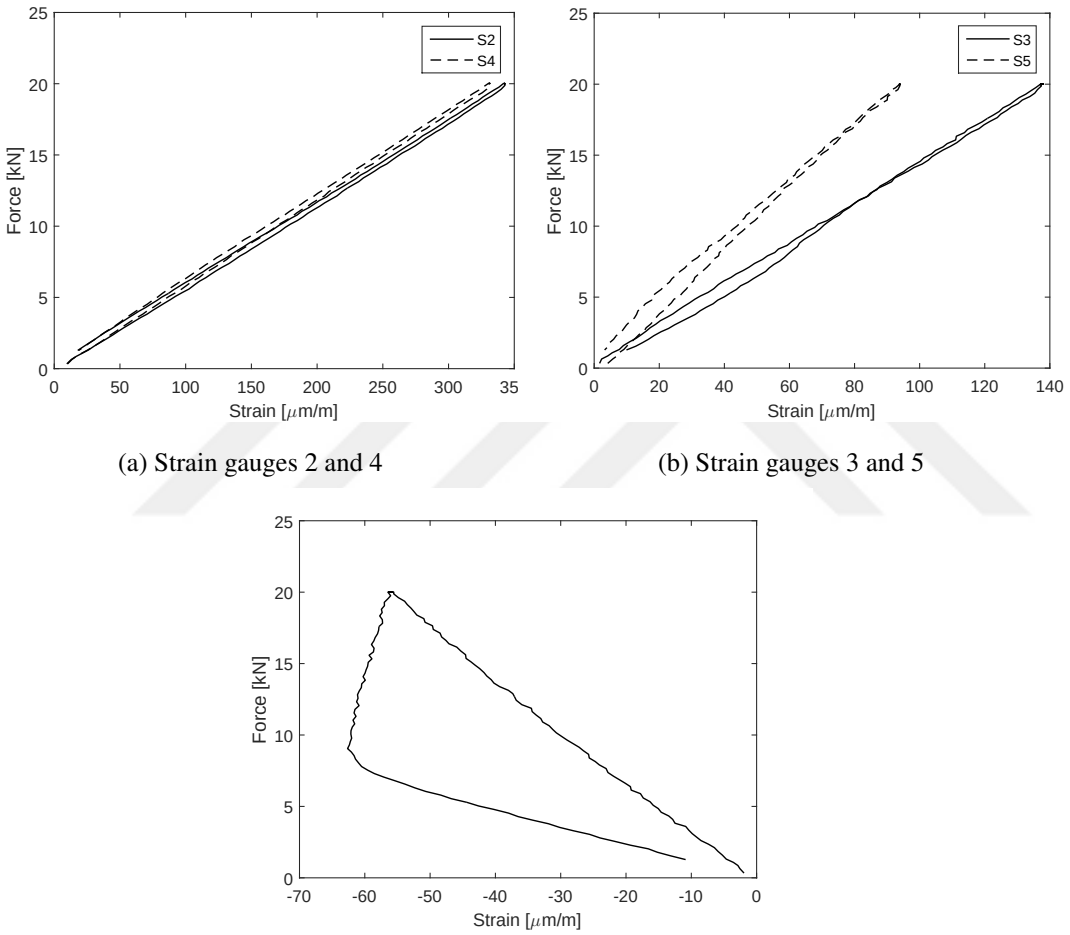


Figure 4.34: Load displacement curve of the system obtained from the relative displacements between paths 1 and 4

4.3.1.3 Strain Gauge Results

As it is explained in Section 4.1.5, there are 5 strain gauges attached on the surfaces of the disc and the blade specimens. Locations of the strain gauges used in the experiment are given in Figures 4.8 and 4.9. In the experiment, strain values in the direction of the applied force on those locations are obtained. Strain gauge readings of the experiment with the applied load is presented in Figure 4.35. In the Figure 4.35a, it is seen that strain gauges located at the frontal and backward surfaces (S2 and S4) of the blade specimen yields closer results, which demonstrates a uniform loading in the thickness direction. However, there exists a variation between the readings of the strain gauges mounted on the left and right surfaces (S3 and S5) as shown in Figure 4.35b. This results show that the blade specimen is subjected to a bending load due to an asymmetric loading. In Figure 4.35c, measurements of the strain gauge on the disc specimen (S1) are given. A negative strain is observed at this location. Due to the load transfer through the contact between the pin and the hole of the disc specimen, load is transferred diagonally in the disc specimen. Due to the higher normal stresses on the transverse direction to the applied load on the location of S1, strains on that

direction is higher and because of the Poisson's effect, negative strains are seen on S1 in the loading direction. At the beginning of the unloading step, it is seen that strain readings on S1 continues to be decreasing. This is due to the rigid body motion in the transverse direction to the load direction. The rigid body motion in x direction is explained in Section 4.3.1.2. Because of this rigid body motion, there exists an asymmetric stress state on the two sides of the disc body. Until the stress state on the two sides of the disc becomes equal, strain readings of the S1 decreases. After that it starts to increase and eventually reaches to the value of zero.



(a) Strain gauges 2 and 4

(b) Strain gauges 3 and 5

(c) Strain gauge 1

Figure 4.35: Strain gauge readings of the experiment

In the finite element model, the locations of these strain gauges are discretized with finer meshes. In Section 4.2.1, details of these meshes are explained. To evaluate the strains in the finite element analysis, average strains in the direction of the applied force are extracted from the nodes on these locations at every load step. Strain

readings of the gauge located on the disc (S1) are shown in Figure 4.36 for the experimental data, and simplified and full finite element models of the experimental setup. Averages of the strain readings of S2 and S4, and S3 and S4 are calculated for the experimental results and finite element results. Comparisons of these average strain results for the experiment and finite element analysss are given in Figures 4.37 and 4.38. It can be deducted that the full finite element model of the experimental result yields closer results to experimental results than the simplified model. The average strain readings of the S2 and S4 is the most consistent result to the finite element analysis results. Moreover, the consistency between the strain readings of S2 and S4 are proved in the Figure 4.35a.

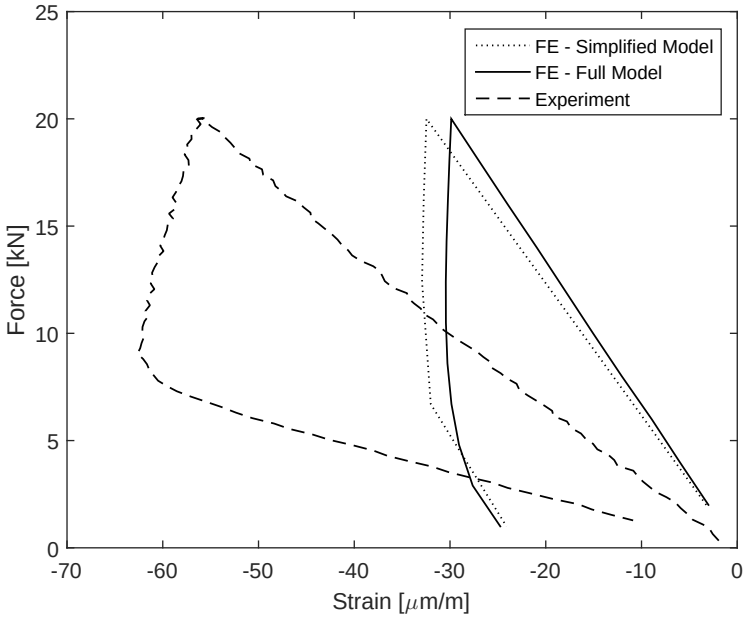


Figure 4.36: Comparison of strain readings S1 of the experiment, simplified finite element model and full finite element model

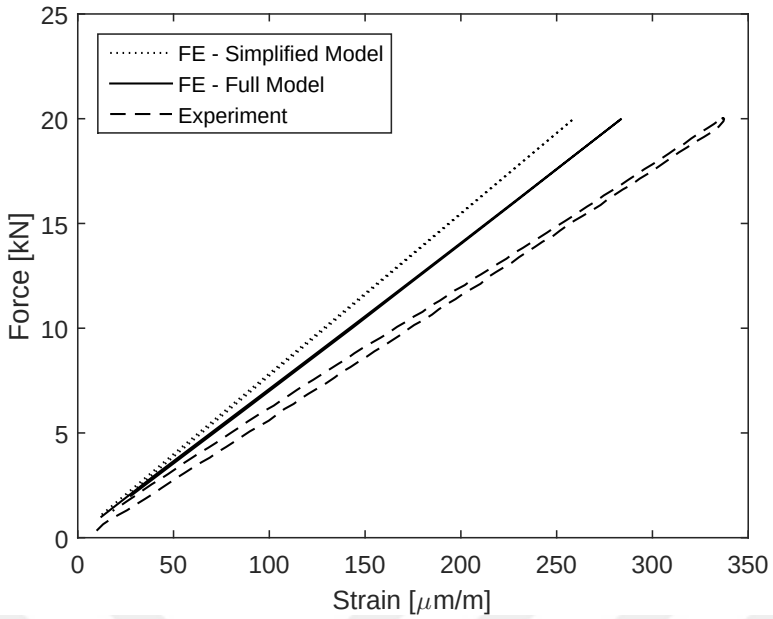


Figure 4.37: Comparison of average strain readings of S2 and S4 of the experiment, simplified finite element model and full finite element model

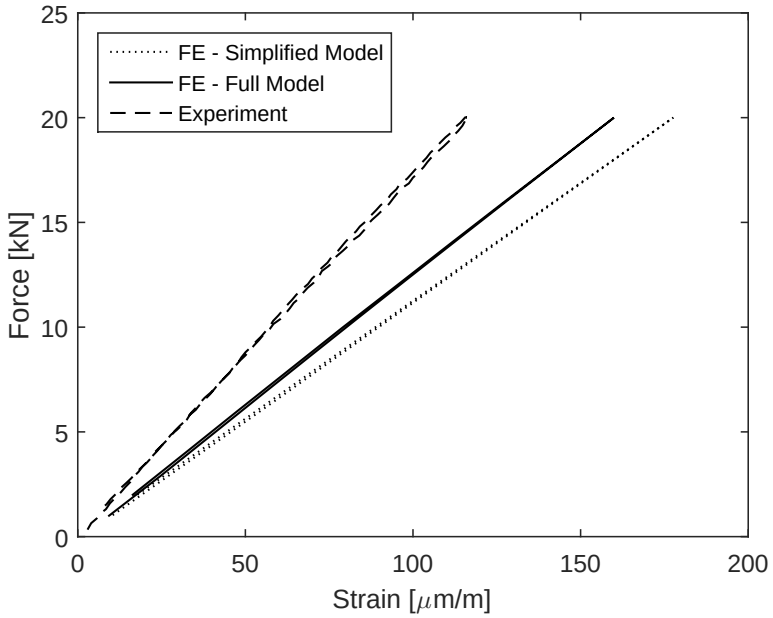


Figure 4.38: Comparison of average strain readings of S3 and S5 of the experiment, simplified finite element model and full finite element model

4.3.2 Assessment of Difference in Results

In Section 4.3, the finite element analysis results and the experimental results are presented. It is seen that there are discrepancies between the results of the experiment and the finite element analysis. The main cause of these discrepancies are stated as the asymmetry in the experiment. During the experiment, rigid body motion is observed between the bodies. In Figure 4.39, a close-up image of the contact region between the specimens at zero load level is given. Two dashed horizontal lines are drawn on the figure, which show the upper level of the disc bodies from the left and the right sides of the blade. It is clearly seen that at the beginning of the experiment, the disc specimen is not aligned perfectly and there exists a difference (approximately 0.3 mm) between the upper sides of the disc. Hence, the left contact pair is more open than the right contact pair. This situation is more clearly seen through the DIC images of the experiment at low load levels. The left contact pair closes when the loading begins, whereas the right contact pair is more in sticking condition. After the gaps between the bodies close, deformation starts. However, in the perfectly symmetric finite element models, the gaps between the contact surfaces are zero and deformation directly starts with the presence of the external loading.

To verify the asymmetry in the contact pairs between the blade and the disc with the finite elements, two cases are created. Firstly, an eccentric loading loading is defined to create asymmetry in the model. Secondly, different friction coefficients are defined on the two contact pairs between the disc and the blade. These conditions are simulated only for the simplified finite element model.

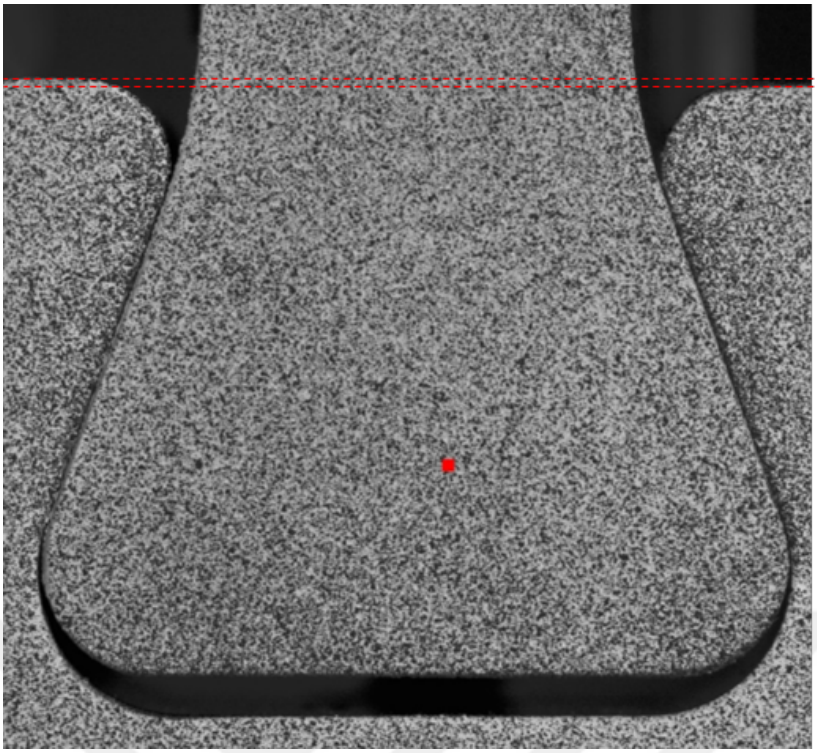


Figure 4.39: Close-up DIC image of the contact region between the disc and the blade at the beginning of the experiment

4.3.2.1 Eccentric Loading Case

The loading and the boundary conditions of the simplified model is discussed in Section 4.2.2. To create an eccentric loading case, loading is applied in both x and y directions. Resultant of the forces in the two directions is equal to the maximum load of 20 kN applied by the testing machine. Two finite element models with 1° and 3° eccentricities in loading are created.

In Figure 4.40, the load displacement curves calculated by averaging the displacements of the paths 1 and 2 given in the Figure 4.31 are presented. It is seen that the eccentric loading does not have a significant impact on the load displacement curve.

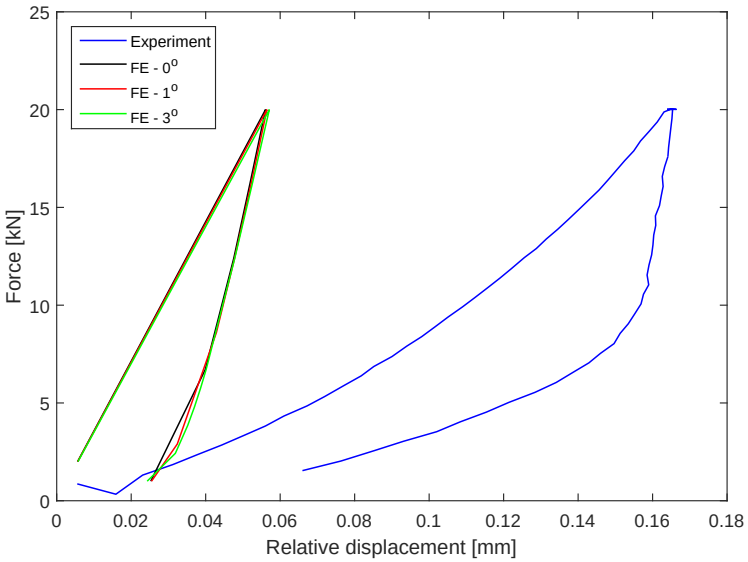


Figure 4.40: Load displacement curves of the system obtained from averaging displacements of paths 1 and 2. Finite element results are presented for perfectly symmetric and two eccentric loading cases.

4.3.2.2 Different Friction Coefficients Between Two Contact Surfaces

To demonstrate the uneven contact states between the left and the right contact pairs that occur during the experiment, different friction coefficients are assigned to the contact pairs in the finite element analysis. Two models are created with frictions coefficients 0.01-0.3 and 0.05-0.3 defined on the contact surfaces.

In Figure 4.41, the load displacement curves calculated by averaging the displacements of the paths 1 and 2 given in the Figure 4.31 are presented. In the figure, it is seen that the definition of the asymmetric contact condition with smaller friction coefficient assigned on the left contact pair (assuming the DIC area as frontal area) make the finite element results closer to the experimental results.

Equivalent (von Misses) strain contour plots of the experiment and the finite element analysis with uneven friction coefficients of 0.01 and 0.3 defined on the contact surfaces are presented in Figure 4.42. It is seen that for the finite element model with asymmetric contact definition, the peak of the equivalent strain is localized at the bottom of the right contact pair. Hence, besides the peak value, the left contact pair

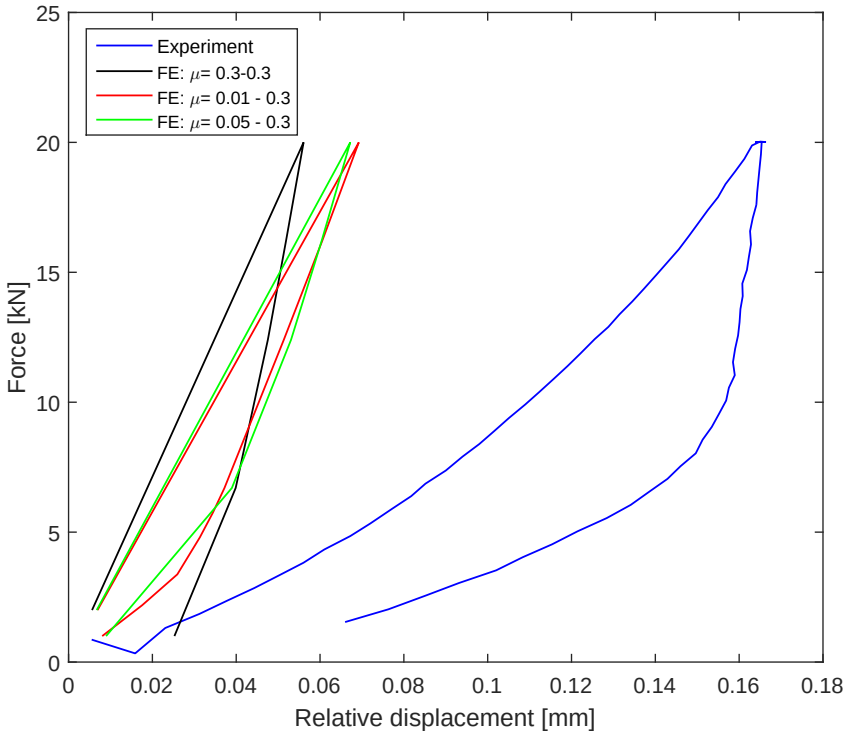
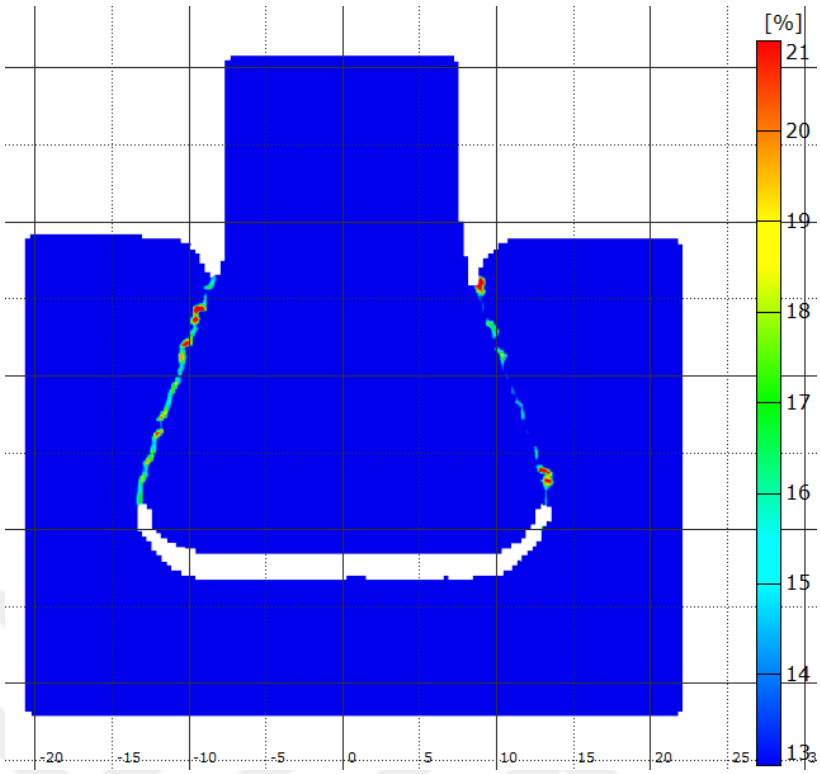
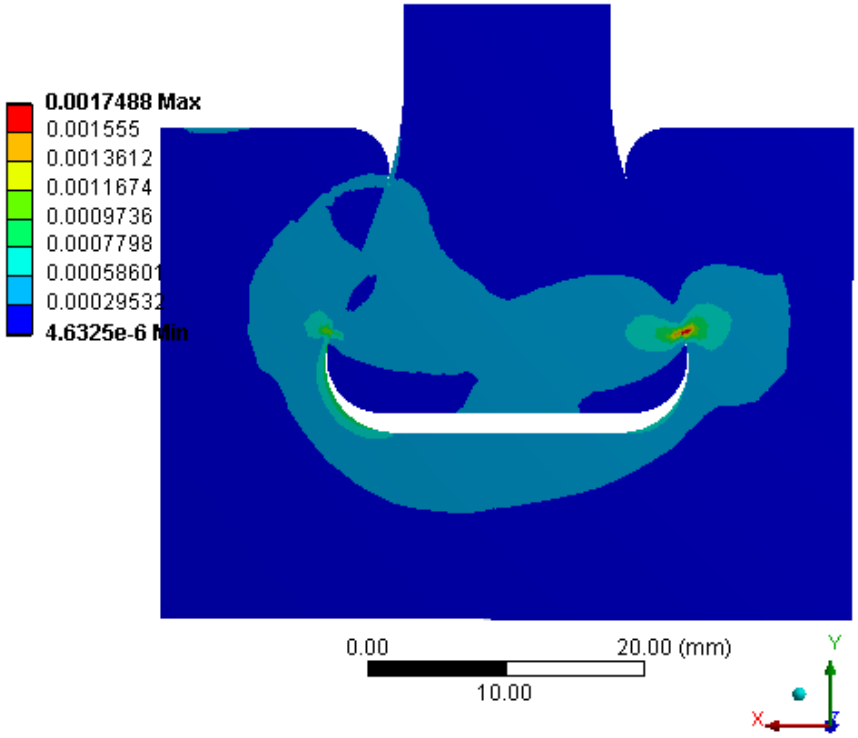


Figure 4.41: Load displacement curves of the experiment and the finite element model obtained from averaging displacements of paths 1 and 2. Finite element results are presented for perfectly symmetric and two uneven friction coefficient cases.

has a higher equivalent strain distribution than the right contact pair. The same phenomenon is seen in the experimental results as well.



(a) Experiment



(b) Finite element model with 0.01 and 0.3 friction coefficients on contact surfaces

Figure 4.42: Von Misses strain at the stage of 20 kN maximum load

4.4 Third Experiment on the Dovetail Specimen

The possible reasons for the differences between the results of the finite element analysis and the experimental study are discussed in the previous section. The main problem in the first two experiments can be summarized as the difference between the slip-stick conditions of the two contact pairs defined between the disc and the blade caused by the misalignment of the specimens. This misalignment resulted in a rigid body motion at the beginning of the experiment, before any deformation starts. To overcome this problem, a third experiment is conducted. Some modifications are made in the experimental procedure. In the following subsections, firstly the modifications are explained and then, the updated finite element model is discussed. Lastly, results of the updated finite element model are discussed with the findings of the third experiment.

4.4.1 Alterations of the Third Experiment and the Finite Element Model

The first alteration made is to attach the components of the experiment upside-down. In Figure 4.43, the experimental setup of the third experiment is given. In the new setup the disc (the heavier part) is attached to the upper grip while the blade (the lighter part) is attached to the lower grip. Therefore, the force applied to the dovetail connection from the blade.

Another difference made in this experiment is the manual loading of the dovetail. Hence, a displacement controlled loading up to the 20 kN load is made. The loading of the parts is performed slower compared to the first two experiments and at each load step, strain gauge readings are controlled and the asymmetry is checked. Before starting the experiment, parts are incrementally loaded to 20 kN to check the misalignments between the bodies after the installation. During the loading of the specimens, at the 0.22 mm, 0.39 mm and 0.48 mm actuator displacement levels, the screw connecting the blade and the adapter is tapped until the strain readings of the S3 and S5 (strain gauges that show the bending in the system) yield closer measurements. The strain readings before and after tapping are shown in Table 4.4. After reaching the maximum load of 20 kN, unloading is performed until a load of 3 kN

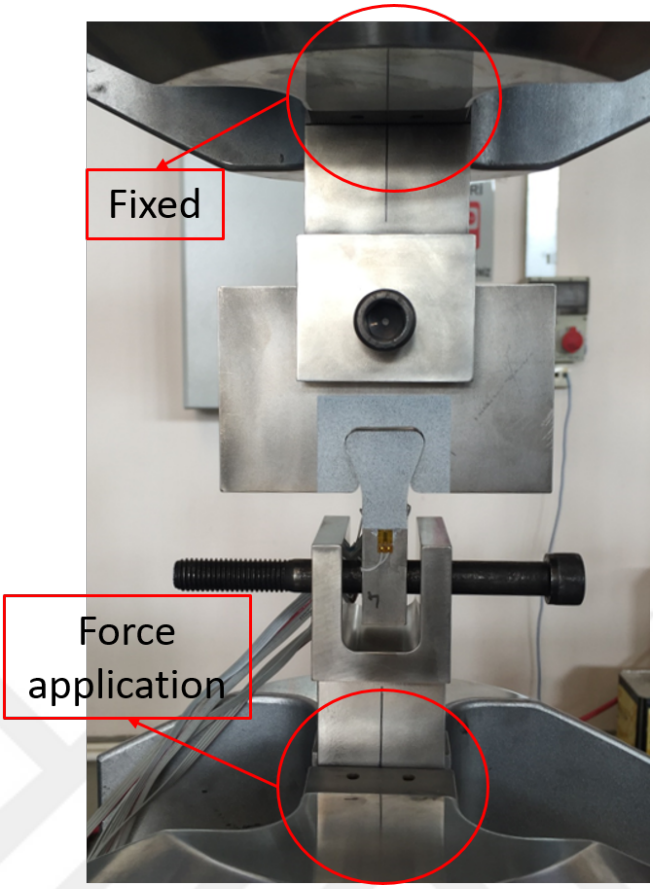


Figure 4.43: Modified experimental setup

and the last tapping is done at this stage. Having set the 3 kN load level as the initial (zero) stage of the experiment, the experiment starts with the incrementally applied displacements until 20 kN force is achieved. In Table 4.5, load stages of the third experiment is given. Strain and DIC measurements are taken at these load stages.

Table 4.4: Strain gauge readings of S3 and S5 before and after tapping at the pre-loading stage of the third experiment

	Disp [mm]	**Load [kN]**	**S3 [µm/m]**	**S5 [µm/m]**
Before 1.tap	0.22	5.19	-7	42
After 1.tap	0.22	6.05	20	20
Before 2.tap	0.39	15.02	78	64
After 2.tap	0.39	13.77	62	69
Before 3.tap	0.48	19.88	105	94
After 3.tap	0.48	19.50	97	99
Before 4.tap	0.16	3	-5	10
After 4.tap	0.16	3.5	5	5

Table 4.5: Load steps of the third experiment

Stage	Displacement [mm]	Measured Force [kN]	Stage	Displacement [mm]	Measured Force [kN]
0	0.15	3.5	**7**	0.28	10.06
1	0.17	4.50	**8**	0.33	12.1
2	0.18	5.06	**9**	0.37	14.2
3	0.20	6.13	**10**	0.40	15.9
4	0.22	7.06	**11**	0.44	18.1
5	0.24	8.08	**12**	0.47	19.9
6	0.26	9.02			

The first change in the new finite element models is the load application nodes. In Section 4.2, details of the boundary conditions of the models are explained. The load application nodes and fixed nodes are switched in accordance with the experiment. Secondly, in the simplified finite element model of the experimental setup, after switching the load applied nodes and the fixed nodes, it is seen that the shape of the upper hole deforms to an elliptic like shape with the presence of loading. To prevent this unrealistic change to occur, two additional constraints are defined on the simplified model. In Figure 4.44, the nodes that are subjected to new constraints are highlighted and the defined constraints are given in Equations 4.1a and 4.1b.

$$u_x^A - u_x^B = 0 \tag{4.1a}$$

$$u_y^A - u_y^B = 0 \tag{4.1b}$$

All the other parameters (parameters regarding to mesh, contact, etc.) are kept same. The analyses are carried out in 13 load steps with 1 substep defined in each load step. Force controlled analyses are carried out with the loading applied accordingly to the load stages of the experiment presented in Table 4.5.

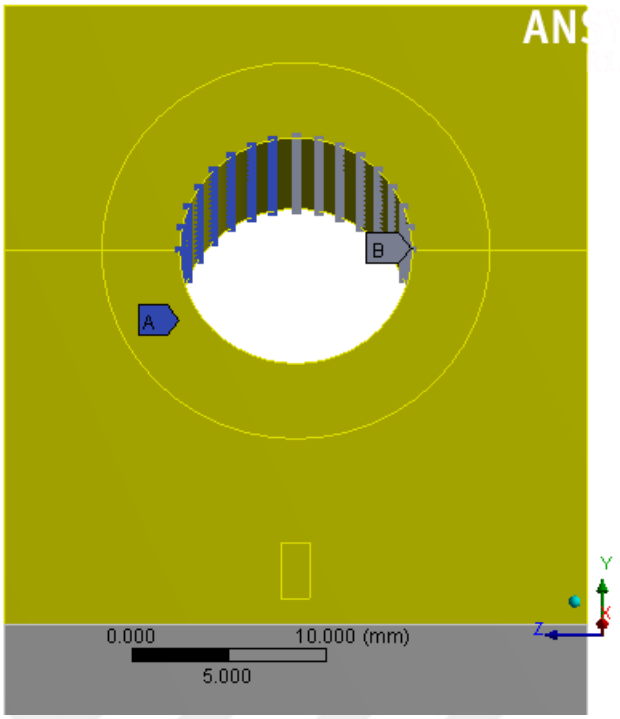


Figure 4.44: Nodes that additional constraints are defined on for the simplified finite element model of the third experiment

4.4.2 Comparison of the Finite Element and Experimental Results

Applied displacements and their resultant forces measured in the experiment are tabulated in Table 4.5. In the full finite element model of the experimental setup, it is possible to obtain the displacements of the nodes that are subjected to external forcing. In Figure 4.45, the load displacement curve of the global system is presented for the experiment and the full finite element model. By comparing Figures 4.22 and 4.45, it is clearly seen that the global response of the system in the experiment is close to be linear compared to the previous experimental result presented in Figure 4.22. Hence, the discrepancy between the experimental and the finite element results is decreased.

In Section 4.3.1.2, the methodology to obtain the load displacement curves by using DIC results are explained in detail. Following the same procedure, the relative displacements of the paths 1 and 2, and paths 1 and 3 defined in Figure 4.31 are calculated at the each load step. In Figures 4.46 and 4.47, load displacement curves

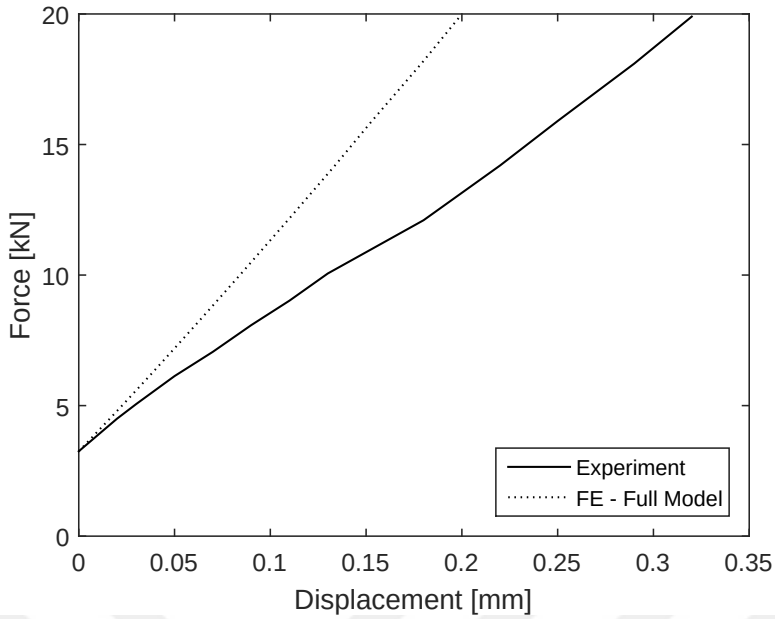


Figure 4.45: Load displacement curve of the global system

extracted by using DIC results are presented together with finite element results. By individually comparing Figures 4.46 and 4.32, and 4.47 and 4.33, it can be stated that the results of the third experiment are more consistent with the finite element analyses results compared to the previous experiments. Moreover, the difference between the finite element results are small. In Figure 4.46, the two finite element results are almost on top of each other and the difference between the displacement values at the last load stage is 1 μm in Figure 4.47.

In Section 4.1.5, details of the strain gauges used in the experiment are discussed. In Figures 4.8 and 4.9, locations of these strain gauges are given. Strain readings obtained in the third experiment are presented in Figure 4.48. It can be deducted from the Figure 4.48a that, strain readings of the gauges mounted on the front and the back surfaces of the blade (S2 and S4) are very consistent. Amount of bending experienced during the experiment can be visualized by investigating the strain measurements between the gauges on the left and the right side of the blade (S3 and S5). In Figure 4.48b, readings of these strain gauges are given. Even though a perfect alignment is tried to be achieved in this experiment, there exists still asymmetry and bending on the blade. However, the discrepancy between the strain readings of S3 and S5 is smaller compared to the previous experiment.

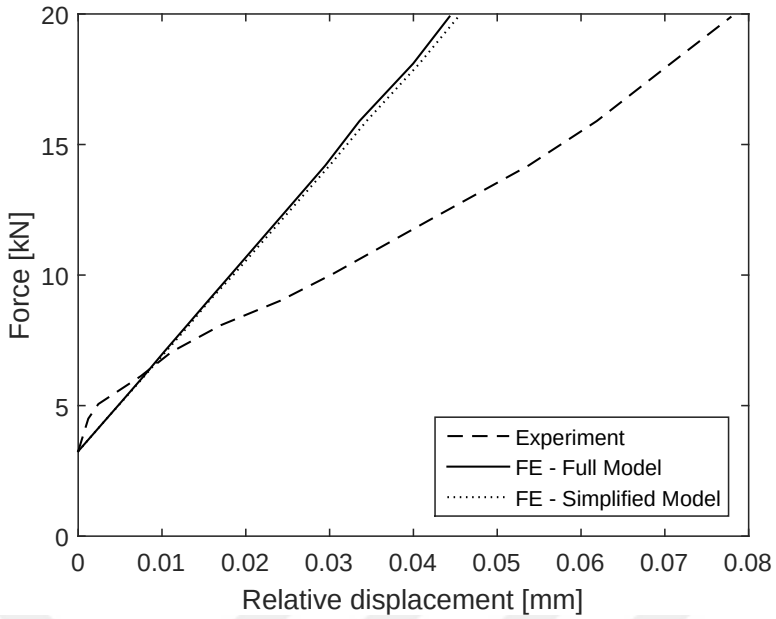


Figure 4.46: Load displacement curve of the system obtained from averaging displacements of path 1 and 2

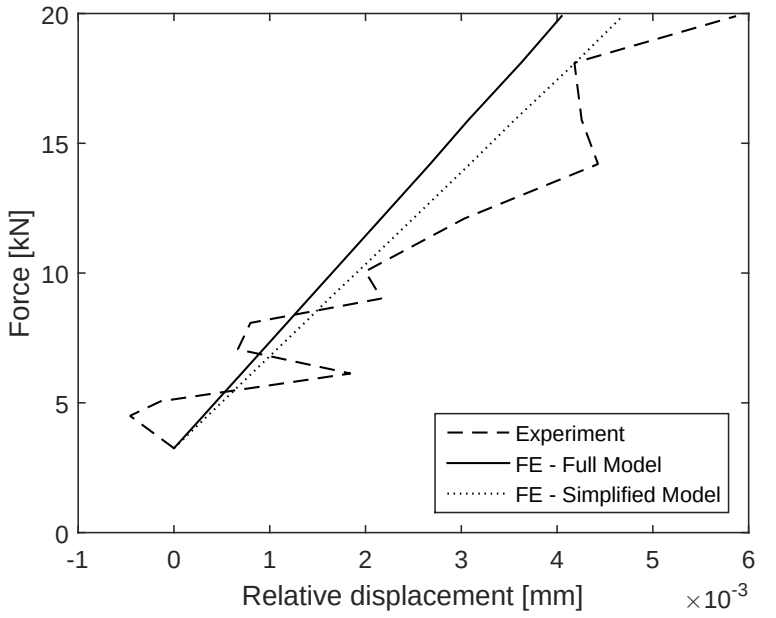
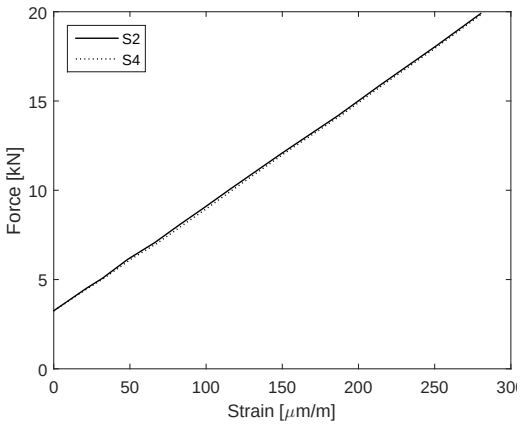
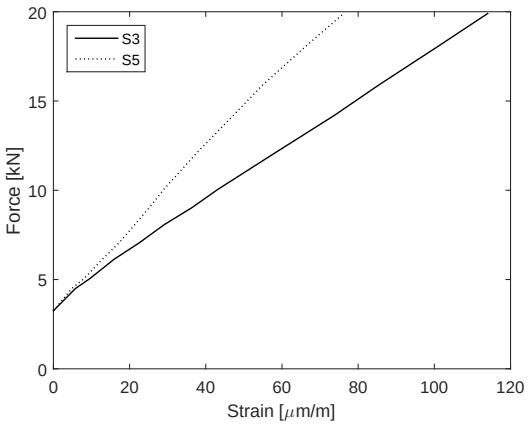


Figure 4.47: Load displacement curve of the system obtained from averaging displacements of path 1 and 3

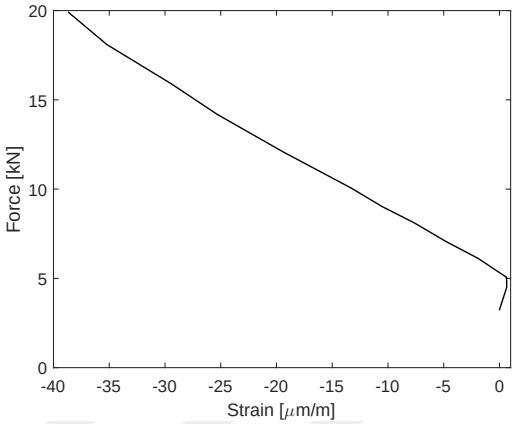
In Figure 4.49, the strain reading of S1 is given with the result of the two finite element models. In Figures 4.50 and 4.51, average strain readings of the strain gauges S2 and



(a) Strain gauges 2 and 4



(b) Strain gauges 3 and 5



(c) Strain gauge 1

Figure 4.48: Strain gauge readings of the thirdexperiment

S4, and S3 and S5 are presented. It is clearly seen that the finite element analyses results and the experimental results are more consistent compared to the previous experiments. Hence, the strain results of the simplified finite element model of the experimental setup are closer to the experimental data compared to the full finite element model.

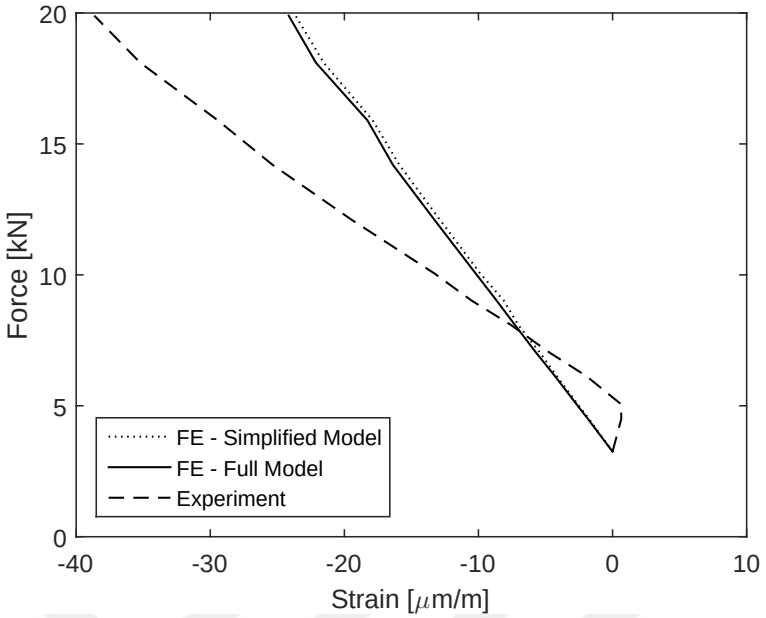


Figure 4.49: Strain readings S1 of the experiment, simplified finite element model and full finite element model

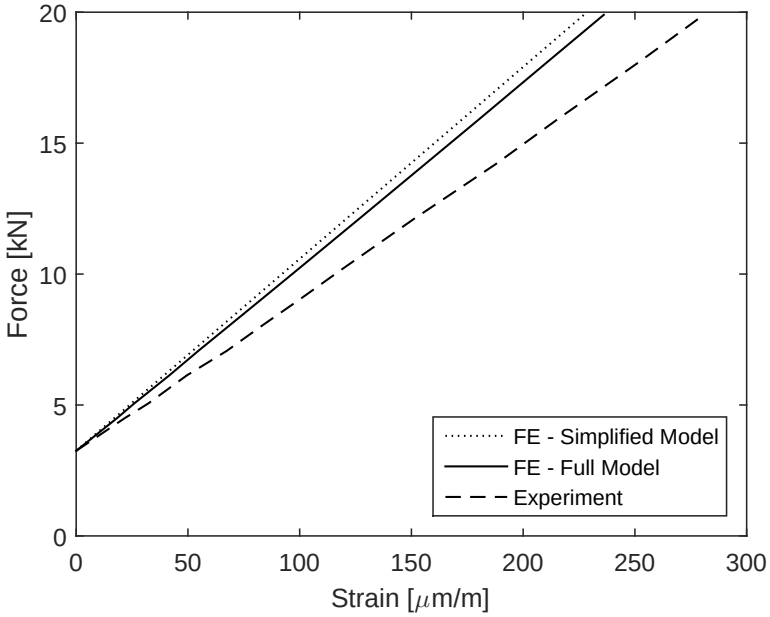


Figure 4.50: Average strain readings of S2 and S4 of the experiment, simplified finite element model and full finite element model

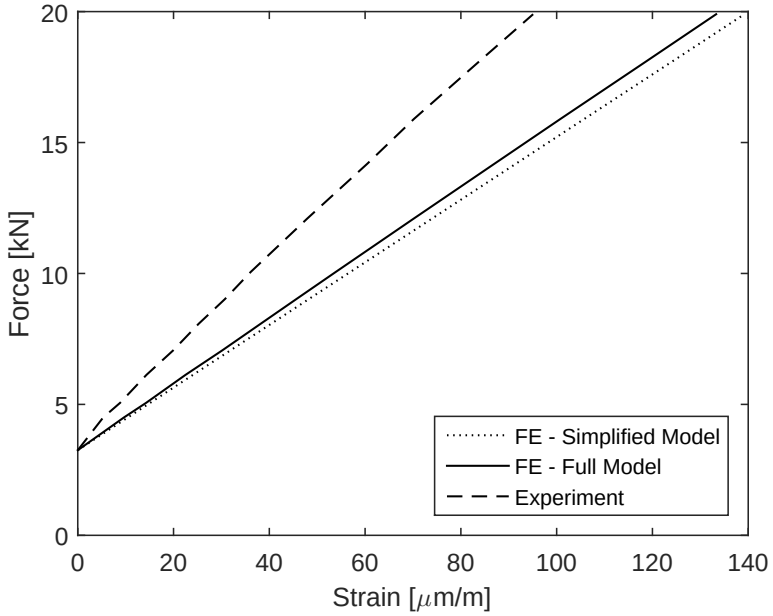


Figure 4.51: Average strain readings of S3 and S5 of the experiment, simplified finite element model and full finite element model

4.5 Conclusion of the Experimental Studies

In total of three experiments of the dovetail specimen are conducted. Results of the first experiment is not presented in the thesis work, since only 3D DIC technique is used without strain gauges in that experiment and the resolution of the results is considered as unsatisfactory. Therefore, in the second and the third experiments, 2D DIC measurements are done on the disc and the blade specimens. Post-processing the DIC results, displacements in the load direction and its transverse direction, von-Misses strain plots and relative displacements of the paths defined on the interested area of DIC are extracted. In addition to DIC measurements, five strain gauges are used in the second and the third experiments. Four of the strain gauges are mounted on the blade and one of them is glued on the disc. From the strain gauge readings on the blade, it is possible to observe the bending of the blade specimen during the experiment. Moreover, the load and the displacement values are extracted from the tensile testing machine.

In the first two experiments, a strong asymmetry is observed. A non-linear behaviour in the load-displacement curves obtained by using DIC and tensile testing machine are seen in Figures 4.22 and 4.32. Hence, there exist inconsistency between the finite element results and the experimental results. The misalignment of the disc and the blade parts at the beginning of the experiment, geometric imperfections caused by the manufacturing of the parts and inequality of contact conditions of the two contact regions between the disc and the blade are the causes of these inconsistencies. To overcome some of these issues, a third experiment is conducted. In this experiment, the components of the experimental setup are installed to the tensile test system upside-down. Load is applied from the blade side and the disc side becomes the fixed part. Furthermore, a pre-loading stage is done before starting the real experiment. At this stage, by externally tapping the screws (pins) at certain load levels, asymmetry in the parts is tried to be reduced. After the pre-loading stage, parts are unloaded to 3 kN level. In order not to loose the alignment achieved in the pre-loading, parts are not unloaded to a load level below 3 kN. The experiment is started from this load level and results are compared by assuming this level as zero load level. In Appendix A.4, experimental and finite element results of the second and the third experiments are

presented. The results of the last experiment are closer to and more consistent with the results of the finite element model. Such consistency has not been achieved in the first two experiments.

To sum up, it can be concluded that tensile testing of the dovetail specimen requires a very high attention at the preparation of the experiment. Installation of the components of the experiment should be made with significant caution. It is seen that a relatively small imperfections and misalignments during the experiment result in inconsistencies in both the global and the local results.

CHAPTER 5

CONCLUSION

In the first part of the thesis, Chapter 2, a parametric study is presented. A simple 2D finite element model consisting of two rectangular blocks on top of each other is selected for the analyses. During the parametric study, investigation of the effects of the parameters that define contact is conducted. The parameters investigated defines the behaviour of the contact in normal and in tangential directions. These parameters can be listed as: the normal stiffness factor, the penetration tolerance factor, the elastic slip tolerance factor, the friction coefficient and the constraint enforcement methods, which are the Normal Lagrange method, the Pure Penalty method and the Augmented Lagrange method. Due to the loading and the boundary conditions of the model, high contact stresses occur at the contact surfaces between two blocks. At one edge of these contact surfaces, stress values have a peak. The effect of the contact parameters are investigated on the contact stresses in the neighbourhood of the peak contact stress and at their peak values. It is concluded that the change in the normal stiffness factor only affects the peak value of the contact stress. For the normal stiffness factors smaller than 1, the peak value of the contact stress is dependent on the factor chosen. After the value of 1, it is seen that the peak contact stress does not fluctuate with the alteration of the normal stiffness factor. However, convergence difficulties are observed for very high values of the normal stiffness factor. It is concluded that values between 1 and 2 for the selection of the normal stiffness is adequate for this model. The effect of the penetration tolerance factor is only seen in the neighbourhood of the peak contact stress. As the penetration tolerance factor increases beyond program default value of 0.1, a decrease in the peak contact stress is observed. It is observed that the elastic slip tolerance factor does not affect the contact stress. The program

default value of 0.01 can be used for the elastic slip tolerance factor. The peak value of the contact stress is dependent on the friction coefficient. The friction coefficient has also a direct effect on the slip-stick condition of the contact. Choice of the friction coefficient should be made according to the material set chosen for the analysis. For all three constraint enforcement methods, it is seen that the contact stress results are identical. Detailed formulation of these methods are discussed in Section 2.2.6.

In the second part of the thesis, Chapter 3, submodelling technique is discussed. Firstly, the justification of non-singular peak stresses at the edges of a contact is given. Then, the procedure of the submodelling technique is explained in detail. After explaining the implementation of submodelling technique to a finite element problem with non-singular stress concentration, submodelling is used on two finite element models. The first model is the two rectangular block model discussed in Chapter 2. High contact stresses occur at the bottom left corner of the upper block due to the loading and the boundary conditions applied. Second model is chosen to be the dovetail-rim attachment. It is a widely used real aeroengine compressor disc component. Dovetail consists of two parts; the blade and the disc. Due to the rotation of the engine shaft, centrifugal forces acts on the blade which give an radial outward motion to the blade part. However, this movement is constraint with the disc part and the contact stresses occur at contact surface between the blade and the disc. At the edges of the contact, these stresses have their peak values. Determination of the true contact stresses at these locations are crucial, since the crack initiations occur at these locations. It is seen that the bottom edge of the contact is more critical and the submodelling technique is implemented to this region. For both models, convergence of the peak contact stresses are observed in the submodels. To compare the accuracy of the submodels, global models having a similar mesh size to the fine submodel at the region of interest are created as well. These models are called as extra-superfine global models. It is seen that both submodels yield the same results with their corresponding extra-superfine global models with a significantly less computational time. The computations with submodelling technique run four/five times faster for the two rectangular block model and eight/nine times faster for the dovetail model.

In the last chapter of the thesis, an experimental study on the tensile testing of the dovetail-rim attachment is presented. Firstly, the design of the experimental setup is

presented. A preliminary finite element model of the experimental setup is created and the validation of the strength of the parts under 20 kN loading is checked. It is seen that the stresses occuring on components of the test setup under 20 kN loading are in elastic limits. Then, the experimental setup and the procedures of the experiment are given. The global load displacement data obtained from the tensile test machine, digital image correlation (DIC) measurements and strain gauges are used as the measurement tools in the experiments. In total of three experiments are conducted. In the first experiment, 3D DIC technique is used without the implementation of the strain gauges. Due to the harder calibration of 3D DIC, results obtained in the first experiment are regarded as unsatisfactory. In the second experiment, all of the measurement tools are used. To compare experimental results with the finite element results, two finite element models are created. One of the models created consists of all components of the experimental setup and the second model is a simplified model with only the disc and the blade specimens. By comparing the results of the second experiment with the finite element results, it is seen that there is a discrepancy between them. The causes of these differences are explained as the asymmetry in the slip-stick conditions on the contact pairs between the disc and the blade specimens, misalignment of the parts during the installation and geometric imperfections of the parts due to the manufacturing processes. To overcome these uncertainties, a third experiment is conducted. A pre-loading stage is included to the experimental procedure. During this pre-loading stage, alignment of the parts is aimed by externally tapping the pins. The results of the third experiment are more consistent with the finite element results. This justifies that the imperfections during the tensile testing of the dovetail-rim attachments result inconsistency in the results. Hence, handling and installation of the experimental setup should be made with caution. Close geometric tolerances should be set on the disc and the blade in order to prevent asymmetry as much as possible.

During the experiments of the dovetail-rim attachment, it is seen that the system is extremely stiff, the displacements and the strains measured are too small. For this reason, these measurements are highly sensitive on the tolerances and imperfections in the experiment. Therefore, for the future work, the experiment is planned to be conducted again with manufacturing the disc and the blade with a softer material

(such as aluminium). Comparison of the finite element and the experiment by using softer specimens will be more logical, since the strains and the displacements on the specimens will be higher and system will be less sensitive to the experimental imperfections.

REFERENCES

[1] K. Anandavel and R. V. Prakash. Effect of three-dimensional loading on macroscopic fretting aspects of an aero-engine blade–disc dovetail interface. *Tribology International*, 44(11):1544–1555, 2011.

[2] R. ANSYS. 14.5. *Academic, Structural Analysis Guide*, 2013.

[3] J. Beisheim and G. Sinclair. On the three-dimensional finite element analysis of dovetail attachments. *Journal of Turbomachinery*, 125(2):372–379, 2003.

[4] J. Beisheim and G. Sinclair. Three-dimensional finite element analysis of dovetail attachments with and without crowning. *Journal of Turbomachinery*, 130(2):021012, 2008.

[5] W. L. Briggs and A. M. Tutorial. *Society for Industrial and Applied Mathematics*. 1987.

[6] J. Carlberg and B. Toyib. Finite element modelling of interlaminar slip in stress-laminated timber decks, friction interaction modelling using abaqus. pages 15–17, 2012.

[7] D. Coker, G. Lykotrafitis, A. Needleman, and A. Rosakis. Frictional sliding modes along an interface between identical elastic plates subject to shear impact loading. *Journal of the Mechanics and Physics of Solids*, 53(4):884–922, 2005.

[8] D. Coker, A. Rosakis, and A. Needleman. Dynamic crack growth along a polymer composite–homalite interface. *Journal of the Mechanics and Physics of Solids*, 51(3):425–460, 2003.

[9] N. Cormier, B. Smallwood, G. Sinclair, and G. Meda. Aggressive submodelling of stress concentrations. *International Journal for Numerical Methods in Engineering*, 46(6):889–909, 1999.

[10] P. Golden and J. Calcaterra. A fracture mechanics life prediction methodology applied to dovetail fretting. *Tribology International*, 39(10):1172–1180, 2006.

[11] P. Golden and T. Nicholas. The effect of angle on dovetail fretting experiments in ti-6al-4v. *Fatigue & fracture of engineering materials & structures*, 28(12):1169–1175, 2005.

[12] A. Handbook. Vol 13: Corrosion. *ISBN: 0-08170-019-0. ASM International, USA*, 1987.

[13] H. Hertz. On the contact of elastic solids. *Journal für die reine und angewandte Mathematik*, 92(110):156–171, 1881.

[14] J. Jønsson, S. Krenk, and L. Damkilde. Recursive substructuring of finite elements. *Computers & Structures*, 54(3):395–404, 1995.

[15] S. Kuliyev. Two-dimensional problems of elasticity theory. *Proceedings of the XXIV International Conference on Concrete and Reinforced Concrete*, page 352, 1991.

[16] T. A. Laursen. *Computational contact and impact mechanics: fundamentals of modeling interfacial phenomena in nonlinear finite element analysis*. Springer Science & Business Media, 2013.

[17] A. Mechanical. Contact technology guide, 2009.

[18] S. Meguid, M. Refaat, and P. Papanikos. Theoretical and experimental studies of structural integrity of dovetail joints in aeroengine discs. *Journal of Materials Processing Technology*, 56(1):668–677, 1996.

[19] J. Murugesan and Y. Mutoh. Fretting fatigue strength prediction of dovetail joint and bolted joint by using the generalized tangential stress range–compressive stress range diagram. *Tribology International*, 76:116–121, 2014.

[20] T. Nicholas. Critical issues in high cycle fatigue. *International Journal of Fatigue*, 21:S221–S231, 1999.

[21] M. Ogino, A. Takei, S.-i. Sugimoto, and S. Yoshimura. A numerical study of iterative substructuring method for finite element analysis of high frequency electromagnetic fields. *Computers & Mathematics with Applications*, 2016.

[22] P. Papanikos, S. Meguid, and Z. Stjepanovic. Three-dimensional nonlinear finite element analysis of dovetail joints in aeroengine discs. *Finite Elements in Analysis and Design*, 29(3):173–186, 1998.

[23] I. Parsons and J. Hall. The multigrid method in solid mechanics: part i—algorithm description and behaviour. *International Journal for Numerical Methods in Engineering*, 29(4):719–737, 1990.

[24] I. Parsons and J. Hall. The multigrid method in solid mechanics: part ii—practical applications. *International Journal for Numerical Methods in Engineering*, 29(4):739–753, 1990.

[25] L. Shi, D.-s. Wei, Y.-r. Wang, A.-m. Tian, and D. Li. An investigation of fretting fatigue in a circular arc dovetail assembly. *International Journal of Fatigue*, 82:226–237, 2016.

[26] G. Sinclair, N. Cormier, J. Griffin, and G. Meda. Contact stresses in dovetail attachments: finite element modeling. *Journal of Engineering for Gas Turbines and Power*, 124(1):182–189, 2002.

[27] G. Sinclair and B. Epps. On the logarithmic stress singularities induced by the use of displacement shape functions in boundary conditions in submodelling. *Communications in Numerical Methods in Engineering*, 18(2):121–130, 2002.

[28] E. Steuermann. To hertz's theory of local deformations in compressed elastic bodies. In *Proceedings of the USSR Academy of Sciences*, volume 25, pages 359–361, 1939.

[29] M. Storti, N. Nigro, and S. Idelsohn. Multigrid methods and adaptive refinement techniques in elliptic problems by finite element methods. *Computer Methods in Applied Mechanics and Engineering*, 93(1):13–30, 1991.

[30] G. Strang and G. J. Fix. *An analysis of the finite element method*, volume 212. Prentice-hall Englewood Cliffs, NJ, 1973.

[31] D.-S. Wei and Y.-R. Wang. Analysis of fretting fatigue life of dovetail assemblies based on fracture mechanics method. *Engineering Failure Analysis*, 25:144–155, 2012.

APPENDIX A

TECHNICAL DRAWINGS OF THE COMPONENTS OF THE EXPERIMENTAL SETUP

A.1 Technical Drawing of the Blade Specimen

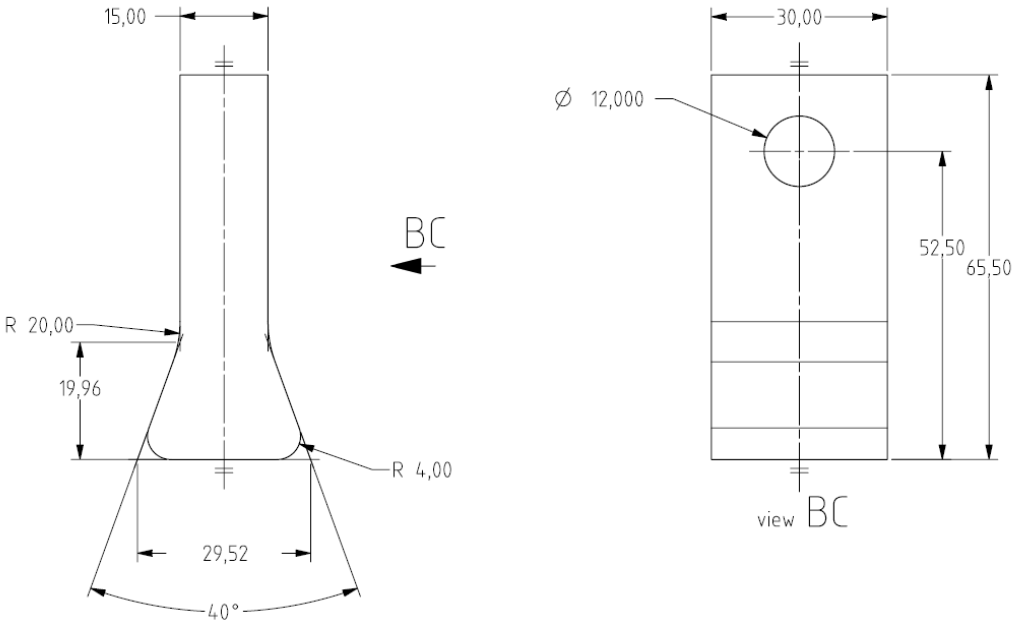


Figure A.1: Technical drawing of the blade specimen

A.2 Technical Drawing of the Disc Specimen

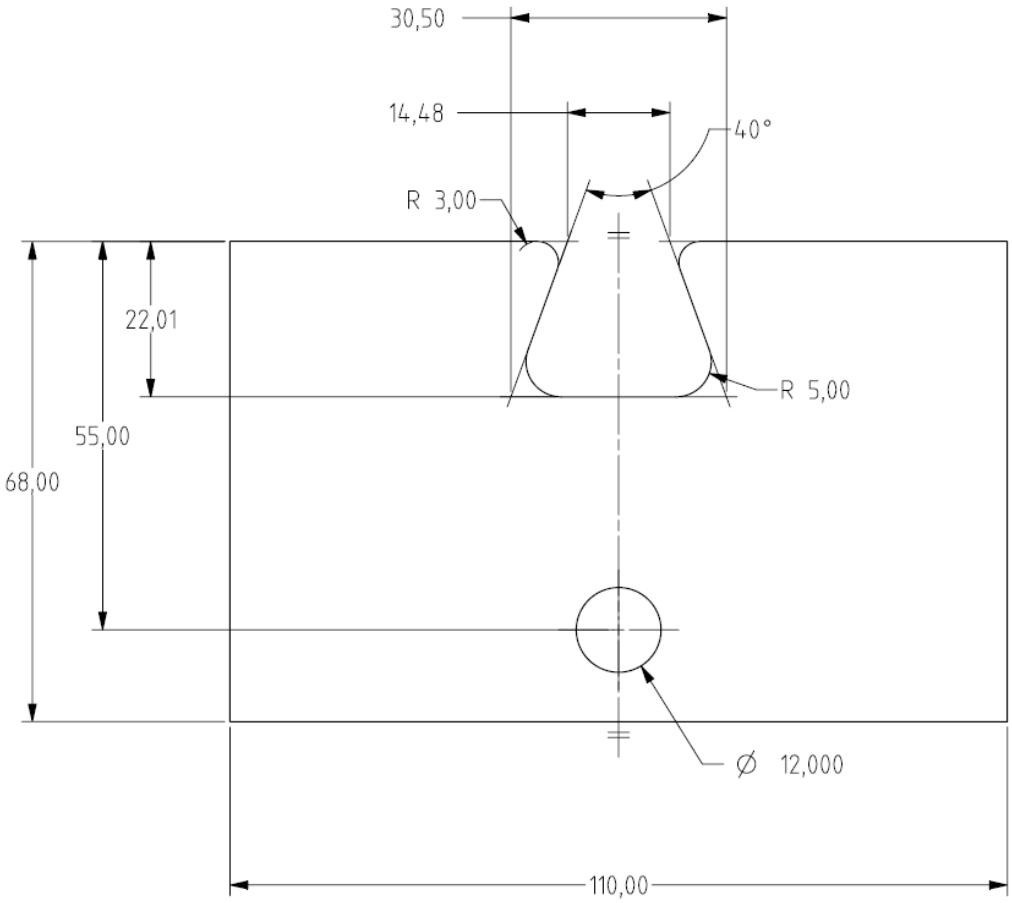


Figure A.2: Technical drawing of the disc specimen

A.3 Technical Drawing of the Holders

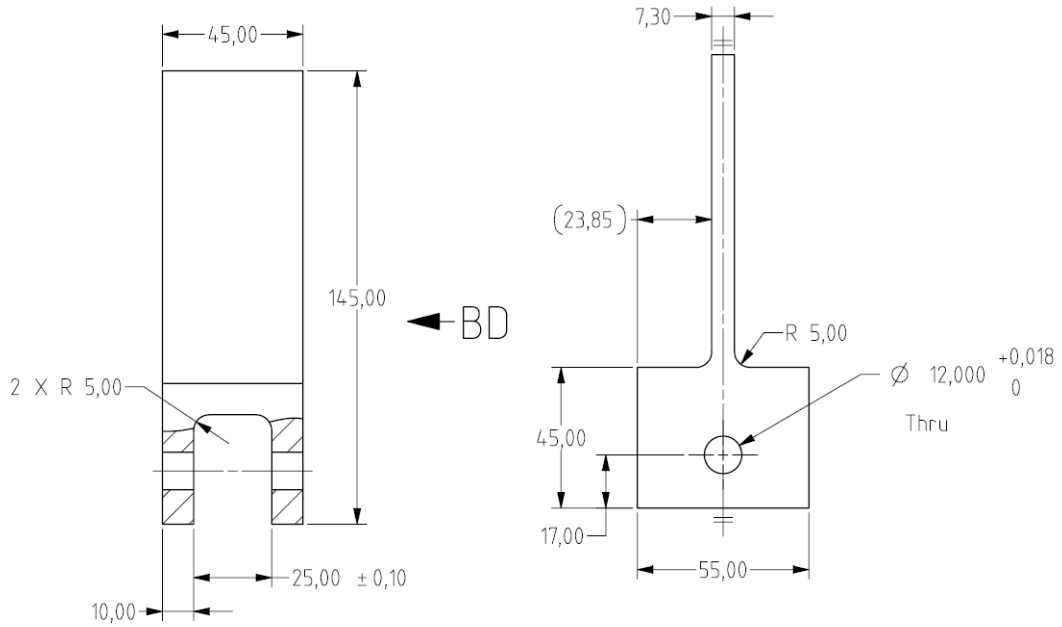


Figure A.3: Technical drawing of the upper holder

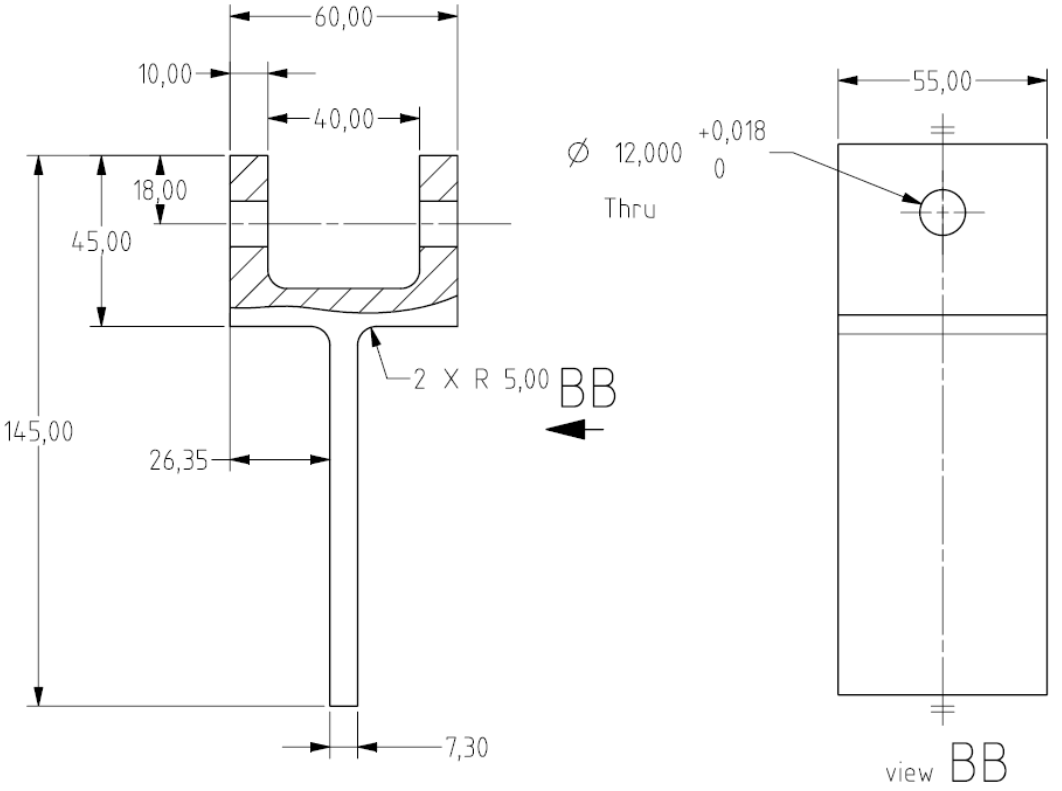
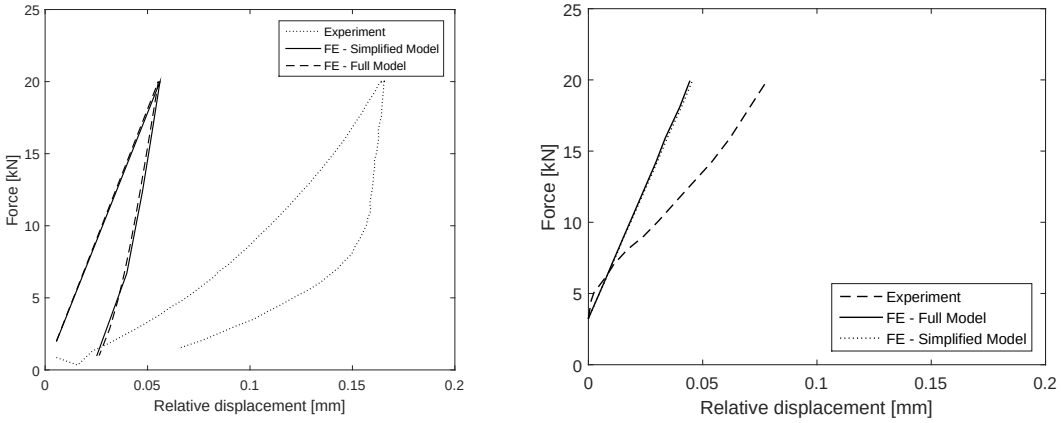


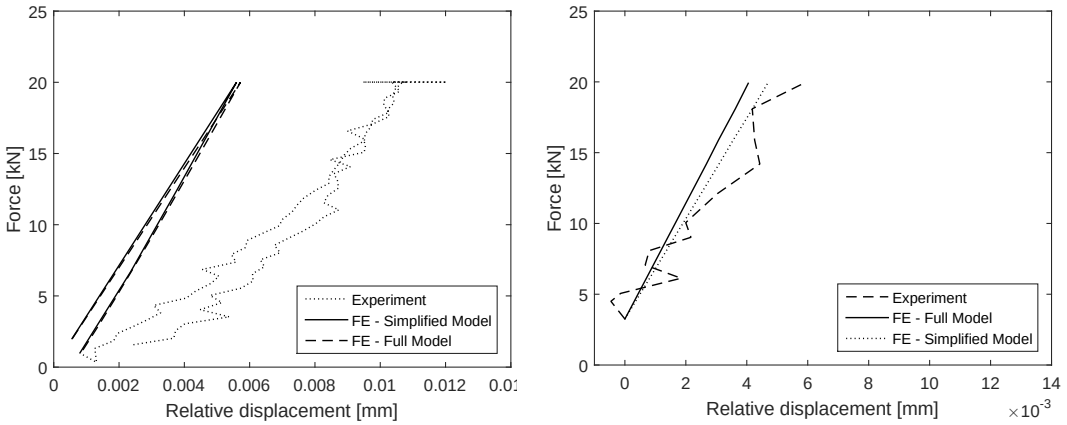
Figure A.4: Technical drawing of the lower holder

A.4 Comparison of the Second and the Third Experiments



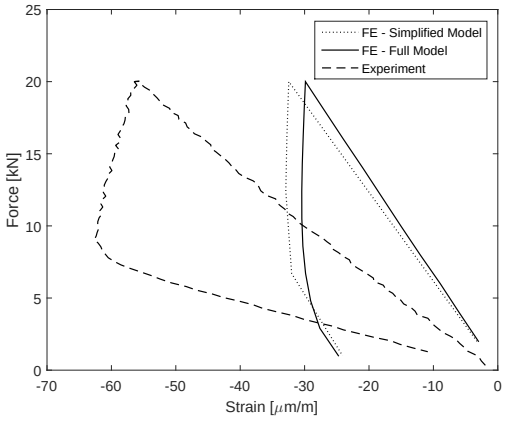
(a) Experiment 2 (b) Experiment 3

Figure A.5: Load displacement curve of the system obtained from averaging displacements of path 1 and 2

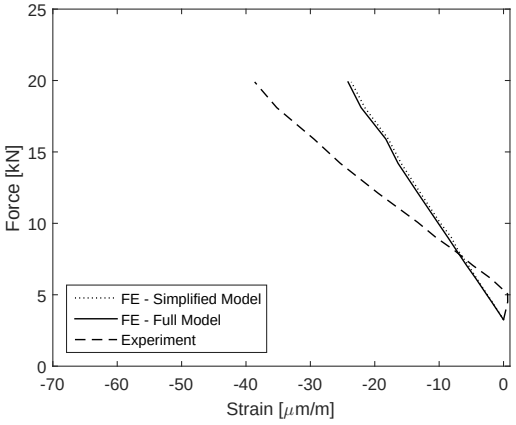


(a) Experiment 2 (b) Experiment 3

Figure A.6: Load displacement curve of the system obtained from averaging displacements of path 1 and 3

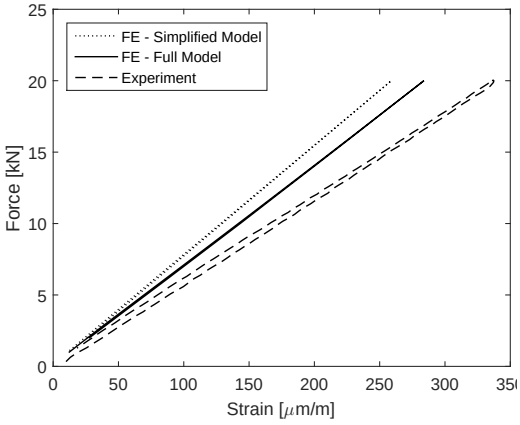


(a) Experiment 2

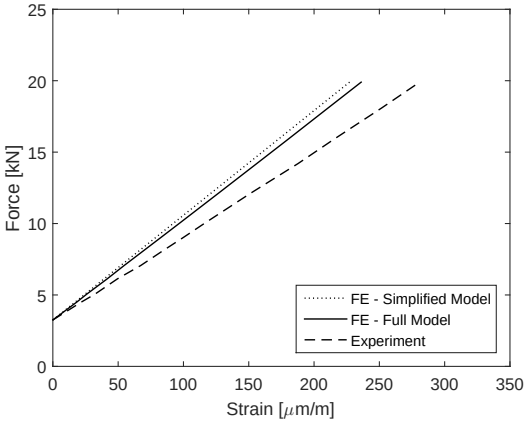


(b) Experiment 3

Figure A.7: Strain readings of S1 of the experiment, simplified finite element model and full finite element model

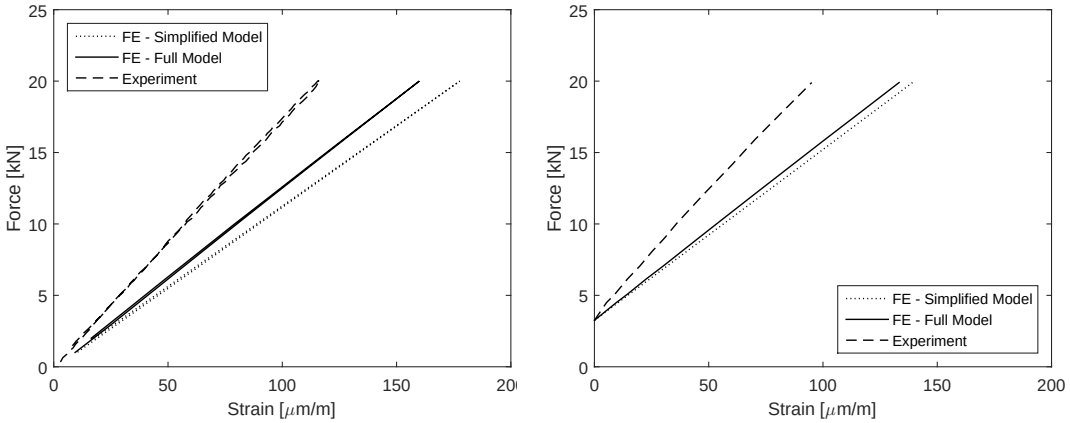


(a) Experiment 2



(b) Experiment 3

Figure A.8: Average strain readings of S2 and S4 of the experiment, simplified finite element model and full finite element model



(a) Experiment 2

(b) Experiment 3

Figure A.9: Average strain readings of S3 and S5 of the experiment, simplified finite element model and full finite element model